Channel Modeling for the Investigation of Human Absorption
in Realistic Indoor Environments

Kanaalmodellering voor het onderzoek van de menselijke absorptie
in realistische indooromgevingen

Aliou Bamba

UNIVERSITEIT
GENT

Université
de Lille
1 SCIENCES
ET TECHNOLOGIES

Universiteit Gent & Université de Lille 1

[1] Universiteit Gent

Faculteit Ingenieurswetenschappen en Architectuur

Vakgroep Informatietechnologie
Gaston Crommenlaan 8 bus 201, B-9050 Gent, België

Tel. : +32 9 331 49 00
Fax. : +32 9 331 48 99

[2] Université de Lille 1 - Sciences et Technologies

Institut d'Electronique, de Microélectronique et de Nanotechnologie

Télécommunication, Interférences et Compatibilité Electromagnétique
Bâtiment P3, USTL - TELICE, Cité Scientifique
F-59655, Villeneuve d'Ascq Cedex, France

Tel. : +33-(0)3 20 43 48 57

Acknowledgment

Every good thing has an end. Indeed, this doctorate program has been a pleasant en rewarding experience and has come to its end. Of course, I could not finalized this Ph.D without helps, supports and guidances from many people. I could also not start this Ph.D without many helps. Even though this book had been entirely dedicated to the acknowledgment, I would need additional pages to mention all the people who have helped me during my curriculum, since it has been a long route. Therefore, I hope that those persons not mentioned by name here will be less strict with my memory, and I apologize in advance.

I start this acknowledgment by giving thanks and praises to God, the One who provides my daily life breath and has permitted that I be here.

Then, I would like to thank my supervisors profs. Luc Martens, Wout Joseph, and Martine Liénard. Luc offered me the opportunity to perform this Ph.D in his laboratory. Besides, his helpful and constructive critics have always improved the quality of my researches. Thanks to Wout for his availability to always discuss with me at any time, for correcting my texts, for giving me confidence when I needed it, and for being my daily guide during this doctorate. I really enjoy and appreciate the collaboration with Wout. I will never forget his enthusiasm and joyful mood of every day, and this has helped me during some tough moments. Martine was my professor in antennas theory and wireless propagation during my master course in Lille. She has always been available for me, to answer my questions, and she has deepened my knowledge in this area. She also provided me valuable advices during this doctorate. I especially appreciate her friendly and enthusiastic mood, which make it very comfortable to work with her.

Many thanks to the members of my jury: profs. Patrick De Baets, Claude Oestges, Gert F. Pedersen, Davy Gaillot, Heidi Steendam, and Hendrik Rogier. Their comments, critics, and suggestions have helped me to improve the quality and the flow of the dissertation. I also thank prof. Jørgen B. Andersen with whom I have had fruitful discussions throughout this thesis.

A good working environment is a paramount condition to succeed a doctorate or any job. I have had the opportunity to work with people, who, somehow have contributed to that. Therefore, I seize this opportunity to thank all my (ex)colleagues at Wireless & Cable (WiCa): Adrian Juan, Amine Samoudi, Arno Thielens, Brecht Hanssens, Damiano Urbinello, David Plets, Divya Kurup, Emmeric Tanghe, Günter Vermeeren, Francis Goeminne, Frederic Heereman, Jens Trogh, Kris Vanhecke, Leen Verloock, Margot Deruyck, Marina Marinova, Matthias Van den Bossche, Michel M. Tamasala, Mostafa Pakparvar, Ning Liu, Quentin Braet, Reza Aminzadeh, Roel Mangelschots, Said Benaissa, Sam Aerts, Simon Dooms, Toon De Pessemier, and Xu Gong. Thanks Adrian for showing me Ghent by nights. Many thanks to Divya who helps me with tricks in my first days to settle down in Ghent. Thanks Emmeric for all the discussions we have had, for

for all your supports and advices, and I do appreciate your friendship. Thanks Cyriac for being with me as my roommate during the tough moments when we just arrived as students in Morocco, thanks for your nice meals (as I could not cook at that time), your unconditional helps, many thanks again. Samoudian, thank you for everything during our stay in Lille, I have enjoyed. Fabrice, thanks for the sleepless nights, I had great moments with you, and I believe that this helps me to vanish sometimes the pressure and stress. Merci Elodie d'avoir recousu mon pantalon de soutenance, merci pour tes gateaux noctures, et pour tant d'autres. Thanks André (Fofo) for being a good housemate in Mohammedia, and for visiting me many times in Ghent since you moved to Brussels recently, you are a good friend. As they say, friends are like stars; even though you don't see them, you know that they are present. One day, you see them and the friendship sparkles again. Inza, we have experienced so many things together since we were roommates at INPT, Rabat and it still goes on here. Thank you for these moments. Thank you also for visiting me often in Gent, and may God strengthen our brotherhood.

Many thanks to the family Broncquart (Angèle, Hugo, Romane) in Barlin, France, and the family Lham-moumi (Nora, Meriem, Halima, Abdallah & Khadidja) in Casablanca, Morocco. Thanks maman Khadidja for being a mother during my stay in Morocco and your kind hospitality, may God bless your family. I cannot forget to mention my tutors in Abidjan (Konan Aya Jeanne, Massita Koné & Mahamadou Koné), thanks for your hospitality during my high school years, and many others.

Infinite thanks to my bothers and sisters (Djoula, Largaton, and Djénéba, Karidja, Massandjé, Massiri, Salimata, Bintou) and my uncles (Issouf Konaté, and Aboulaye Bamba) and all my family. Thanks for your constant supports, sacrifices and blessings, I am here thanks to you. As said by the mandinka proverb, *a single finger can't pick up stones*. Put differently, *if a single finger picks up stones, there are certainly glue thereon*. If I am the single finger, you are the glue that has permitted me to pick up stones, if any.

Last but not least, my deepest gratitude to my parents: Fanta & Mamadou. Thanks for fashioning me to be who I am, the blessings, and everything. I owe you everything. There are no words strong enough to describe my gratitude and respect for you. I love you.

Aliou Bamba
Ghent, june 2015

Contents

i

List of Figures

List of Tables

List of Acronyms

0-9

3GPP 3rd Generation Partnership Project

A

AAU Aalborg University
ACS Absorption Cross Section
ADS Advanced Design System
APDP Averaged Power Delay Profile
AWGN Additive White Gaussian Noise

B

BMI Body Mass Index
BPSK Binary Phase Shift Keying
BSA Body Surface Area

C

COST Cooperation in Science and Technology (European)

D

dB   decibels

DECT   Digital Enhanced Cordless Telecommunications

DMC   Diffuse Multipath Components

DoA   Direction of Arrival

DoD   Direction of Departure

E

EIRP   Effective Isotropically Radiated Power

EKF   Extended Kalman Filter

EM   Electro-Magnetic

EMC   ElectroMagnetic Compatibility

EMF   ElectroMagnetic Field

EMW   ElectroMagnetic Wave

ESPRIT   Estimation of Signal Parameters via Rotational Invariance Technique

F

FCC   Federal Communications Commission

FDTD   Finite-Difference Time-domain

G

GBSCM   Geometry-Based Stochastic Channel Model

GO   Geometric Optics

GSM   Global System for Mobile communications

GTD   Geometrical Theory of Diffraction

I

ICNIRP   International Commission on Non-Ionizing Radiation Protection

ICT Information and Communication Technologies

IEEE Institute of Electrical and Electronics Engineers

L

LOS Line Of Sight

LTE Long Term Evolution

M

MDL Minimum Description Length

MIMO Multiple Input Multiple Output

MISO Multiple Input Single Output

MLE Maximum Likelihood Estimator

mmW millimeter Wave

MPC MultiPath Component

MUSIC MUltiple SIgnal Classifier

N

NLOS Non Line Of Sight

P

PDP Power Delay Profile

PEM Personal Exposure Meter

PN Pseudo Noise

PVC PolyVinyl Chloride

Q

QoS Quality of Service

QQ Quantile-Quantile

R

RC Reverberation Chamber

RF Radio Frequency

RT Ray Tracing

Rx receiving antenna

S

SAGE Space-Alternating Generalized Expectation-maximization algorithm

SAR Specific energy Absorption Rate

SEMCAD Simulation Platform for Electromagnetic Compatibility, Antenna Design

SM Stirred Mode

SNR Signal to Noise Ratio

T

TELICE TELécommunication, Interférences et Compatibilité Electromagnétique

TFSF Total Field Scattered Field

Tx transmitting antenna

U

ULA Uniform Linear Array

UMTS Universal Mobile Telecommunications System

UPML Uniaxial Perfectly Match Layer

US Uncorrelated Scatterer

UTD Uniform Theory of Diffraction

UWB Ultra WideBand

V

VH Visible Human

W

WiFi Wireless Fidelity
WINNER Wireless world INitiative NEw Radio
WLAN Wireless Local Area Network
WSS Wide Sense Stationary

X

XPR Cross Polar Ratio

Nederlandstalige samenvatting

Tegenwoordig worden mensen meer en meer geïnteresseerd in het gebruik van draadloze communicatiesystemen sinds de komst van internet. Het is duidelijk dat het gebruik van informatie- en communicatietechnologieën (ICT) een enorme impact heeft op verschillende aspecten in het leven van een mens, bijvoorbeeld op sociaal-, economisch-, en onderwijskundig vlak. Dit wordt weerspiegeld door de toenemende vraag naar draadloze communicatie apparaten, zoals mobiele toestellen, smartphones, laptops, notebooks, tablets, enzovoort. Bovendien worden er momenteel persoonlijke communicatiesystemen (PCS) ontwikkeld, en zijn deze voornamelijk bedoeld voor gebruikt in indooromgevingen. Mensen zijn geïnteresseerd in deze toepassingen, omdat ze het grootste deel van hun tijd binnen doorbrengen, bijvoorbeeld thuis, in klaslokalen, kantoren, winkels, enzovoort.

Enerzijds hebben onderzoekers de eigenschappen van het draadloze kanaal onderzocht om de capaciteit en prestaties van draadloze netwerken en apparaten te verbeteren. Anderzijds is het belangrijk om zo goed mogelijk de vermogensdichtheid te kennen die invalt op mensen, voor het berekenen van de absorptie van elektromagnetische velden (EMV) in een menselijk lichaam, en te bepalen of er hierdoor mogelijk schadelijke gezondheidseffecten ontstaan. Organisaties zoals de *International Commission on Non-Ionizing Radiation Protection (ICNIRP)* en de *Federal Communications Commission (FCC)* hebben basisrestricties gedefinieerd (gebaseerd op de huidige wetenschappelijke kennis) om de blootstelling van mensen aan elektromagnetische velden te beperken. De fundamentele beperkingen op dit vlak worden gedefinieerd in termen van specifieke energie tempo (SAR) in de radiofrequentie (RF) band. Dosimetrie studies richten zich voornamelijk op het beoordelen, karakteriseren en modelleren van de invallende elektromagnetische velden in een mens en de resulterende absorptie. Het is echter belangrijk om rekening te houden met de recente vooruitgang wat betreft de kennis van het draadloze kanaal bij de evaluatie van deze menselijke absorptie. Diffuus verstrooide velden kunnen echter zeer prominent aanwezig zijn in realistische indooromgevingen, waardoor dosimetrie onderzoek aandacht dient te besteden aan het effect van deze velden op de menselijke absorptie, en om dit eventueel in rekening te brengen. Dit doctoraat, getiteld *Kanaalmodellering voor het onderzoek van de menselijke absorptie in realistische indooromgevingen*, richt zich voornamelijk op dit doel.

Dit proefschrift is als volgt opgebouwd: Hoofdstuk 1 zal kort ingegaan op de modellering van draadloze kanalen in realistische omgevingen. We zien dat *kamer elektromagnetisme* een geschikt kanaalmodel is voor de menselijke absorptie te modelleren veroorzaakt door diffuse velden, omdat slechts enkele parameter (de *nagalmtijd*) voldoende is om deze diffuse verschijnselen te beschrijven in indooromgevingen.

Hoofdstuk 2 stelt een eenvoudig te implementeren methode voor om deze nagalmtijd in een reverberatiekamer (RK) te bepalen. RKs vormen een extreem referentiepunt voor elektromagnetische propagatie te

emuleren in realistische omgevingen waar het diffuse veld dominant is. De methodiek om deze nagalmtijd te bepalen wordt daarna vergeleken met deze van een hoog-resolutie-algoritme. Vervolgens introduceren we het begrip absorptie-doorsnede in diffuse velden. Een experimentele methode wordt ontwikkeld om de absorptie-doorsnede van een canoniek fantoom in diffuse gebieden te bepalen. Numerieke simulaties van dit fantoom worden uitgevoerd om de experimentele aanpak te valideren. Daarna passen we deze methodologie toe om de absorptie-doorsnede van een mens te bepalen in een RK, waarbij rekening wordt gehouden met verschillende lichaamshoudingen. De volgende hoofdstukken zullen een toepassing van dit hoofdstuk zijn, dit wil zeggen, we bepalen de waarden van de nagalmtijd en de blootstelling van een mens in realistische indooromgevingen.

In hoofdstuk 3 worden de eigenschappen van het kamer elektromagnetisme onderzocht in realistische indoor kantoren. We bepalen de waarden van de nagalmtijd in verschillende kantooromgevingen in Gent (België) en in Aalborg (Denemarken) met behulp van de virtuele Meerdere-Ingang Meerdere-Uitgang kanaalstimulator en een echte kanaalstimulator. Vervolgens laten deze nagalmtijd-waarden toe dat we direct de absorptie-doorsnede (van een mens) kunnen bepalen in diffuse velden in een realistisch kantoor.

In hoofdstuk 4 stellen we -voor het eerst- een experimentele methode voor om het hele-lichaam uitgemiddelde specifieke energie tempo (SAR_{hl}) te bepalen van een mens onder realistische omstandigheden in indooromgevingen, dit wil zeggen, in aanwezigheid van diffuse velden. Verschillende scenario's worden er onderzocht, en we tonen aan dat de diffuse velden in belangrijke mate bijdragen (in bepaalde omstandigheden) aan het totale vermogen aanwezig in deze indooromgevingen. We zien dat de bijdrage van diffuse velden in de absorptiesnelheid van mensen zeer prominent aanwezig kan zijn, en daardoor niet systematisch kan worden verwaarloosd.

In de voorgaande hoofdstukken hebben we de absorptie-doorsnede bepaald in diffuse velden, en werd er een experimentele benadering voorgesteld om het menselijke absorptie-tempo te bepalen. Echter, de experimentele methode kan enerzijds moeilijk en langdurig zijn, aangezien het vereist dat er metingen worden uitgevoerd met antennes, een netwerk analysator, kabels en andere apparatuur. Anderzijds kunnen simulaties van de diffuse velden met behulp van numerieke methoden duur zijn in termen van tijd en geheugen. Daarom zal er in hoofdstuk 5 een eenvoudige formule worden voorgesteld met weinig parameters (als alternatief voor numerieke en experimentele methoden) om de totale SAR_{hl} te bepalen van een mens onder realistische propagatie-omstandigheden, dit wil zeggen, in aanwezigheid van diffuse velden en een mogelijke *Line-Of-Sight (LOS)* component. De voorgestelde formule wordt gevalideerd via numerieke simulaties met vier 3-D heterogene menselijke modellen. De formule kan worden gebruikt om de absorptiesnelheid van een mens onder LOS en/of diffuse omstandigheden te bepalen. Bovendien kan deze formule worden gebruikt bij dosimetrie onderzoek om nauwkeurig en snel een beoordeling te maken van de absorptie van een mens onder realistische propagatie-omstandigheden in realistische indooromgevingen.

Hoofdstuk 6 stelt het kamer elektromagnetisme voor met behulp van een RC elektrisch circuit, zodat vermogensdichtheden in een indooromgeving kunnen worden bepaald via ontlading van de energie in dit circuit in een condensator. De theorie richt zich voornamelijk op *Ultra-Wideband* (UWB) systemen en *Wireless Local Area Networks* (WLAN). Er wordt aangetoond dat de absorptie als gevolg van diffuse velden groter is in WLANs dan in UWB systemen. Het circuit-model kan eenvoudig worden ingebed in circuit-simulatoren.

Tenslotte wordt al het uitgevoerde werk samengevat in hoofdstuk 7, en worden er mogelijkheden voorgesteld voor toekomstig uitbreidend onderzoek.

Résumé de la thèse

Plusieurs récherches ont étés dédiées a la détermination du débit absorption énergétique spéfique (whole-body averaged specific absorption rate, SAR_{wb}) en utilisant des modèles numériques de fantôme humains et la méthode de différence fini dans le domaine temporelle (finite-difference time-domain, FDTD). Cependant, toutes ces recherches et d'autres en cours ont seulement étudiées le SAR_{wb} pour des expositions à des ondes spéculaires ou discrètes. Habituellement, le SAR_{wb} est determiné en dosimétrie pour un fantome human exposé à une seule onde électromagnétique. Cependant, les recherches en propagation ont récemment mis en exergue l'existence de champs électromagnétique diffus (diffuse multipath components, DMC) dans les environments indoor (salles de classe, bureaux, magasins, chambres, etc.). Il est donc nécessaire de déterminer l'absorption électromagnétique des humains dûe a ces champs diffus afin de prévenir contre d'éventuels effets nuisibles causés par les radiations électromagnétiques. Cette problématique est complètement absente dans la littérature en dosimétrie.

Nous montrons après une revue des modèles de canaux sans fil que la théorie du *room electromagnetics* est un modèle de canal approprié pour étudier l'absorption humaine dûe aux ondes électromagnétique diffuses. Une méthode pour déterminer le temps de réverbération dans une chambre réverbérante est présentée et validée avec un algorithme à haute résolution. Ces chambres sont considérées comme un cas extrême où les champs électromagnétique diffus sont dominants par rapport aux champs discrets. Une chambre réverbérante est la référence idéale pour simuler un environnement intérieur ou le champ électromagnétique diffus est dominant. La section transversale d'absorption causée par les champs diffus ($\text{ACS}_{wb,dmc}$) est ensuite présentée. Une méthode expérimentale pour déterminer le $\text{ACS}_{wb,dmc}$ d'un fantôme est développée et validée par des simulations numériques via la méthode FDTD. Les propriétés du temps de réverbération ont étés étudiées dans plusieurs environnements, à Gand (Belgique) et à Aalborg (Danemark), en utilisant le sondeur de canal virtuel MIMO (Multiple-Input Multiple-Output) et le sondeur de canal réel. Les valeurs du temps de réverbération permettant ensuite la détermination l'$\text{ACS}_{wb,dmc}$. En outre, nous présentons pour la première fois une méthode expérimentale pour déterminer le débit d'absorption spécifique (SAR_{wb}) dans des conditions de propagation réalistes en environnements intérieurs. Plusieurs scénarii ont étés envisagés et il s'avère que la contribution des champs diffus dans le débit d'absorption spécifique total peut être importante et ne peut être systématiquement négligée ou ignorée en dosimétrie. Par ailleurs, une simple formule (comme alternative aux méthodes numériques et expérimentales) est proposée pour déterminer le SAR_{wb} des humains en présence de champs diffus. La formule est validée par des simulations numériques de fantômes humains hétérogènes et peut être utilisée en dosimétrie pour évaluer rapidement et avec précision le SAR_{wb} total des humains. Enfin, des futures possibilités de recherche concluent cette thèse.

English summary

People are more and more interested in the use of wireless communication systems since the advent of internet. Clearly, the use of Information and Communication Technologies (ICT) has a huge impact on several aspect of people's life, e.g., social, economy, education, etc. This is reflected by the increasing demand for wireless communication devices such as mobile devices, smart phones, laptops, notebooks, tablets, etc. Moreover, Personal Communication Services (PCS) are being developed and are mainly intended for and used in indoor environments. People are interested in these wireless applications because they spend most of their time in indoor environments, e.g., at home, in classrooms, in offices, in stores, etc.

On the one hand, researchers have investigated the properties of the wireless channel to enhance the capacity and performance of wireless networks and devices. On the other hand, knowing accurately the power densities incident on humans is important for calculating the absorption of the fields in human bodies in order to determine if there exist potential harmful health effects. Organizations such as the International Commission on Non-Ionizing Radiation Protection (ICNIRP) and the Federal Communications Commission (FCC) have defined basic restrictions (based on current scientific knowledge) to limit exposure of humans to ElectroMagnetic Fields (EMFs). The basic restrictions are defined in terms of Specific energy Absorption Rate (SAR) in the radio-frequency (RF) band. Dosimetry studies aim at assessing, characterizing, and modeling of the incident EMF and absorption in humans. However, it is important to account for the recent advances made in the understanding of the wireless channel when assessing the human absorption. The presence of diffuse scattered fields may be prominent in realistic indoor environments. Therefore, dosimetry research should pay attention to the effect of diffuse scattered fields on the human absorption and eventually take it into account. The present doctorate entitled *Channel modeling for the investigation of human absorption in realistic indoor environments* aims at this purpose.

This dissertation is organized as follows: Chapter 1 briefly reviews the modeling of wireless channels in realistic environments. We show that the *room electromagnetics* is a suitable channel model to address the human absorption due to diffuse fields, as only one parameter (*the reverberation time*) is sufficient to describe the diffuse phenomena in indoor environments where the diffuse fields are prominent.

Chapter 2 presents an easy-to-implement methodology to determine the reverberation time in a reverberation chamber (RC). RCs are extreme reference to emulate electromagnetic propagation in realistic environments where the diffuse field is dominant. The methodology is compared with a high-resolution algorithm. Then, we introduce the notion of absorption cross section in diffuse fields. An experimental method is developed to determine the absorption cross section of a canonical phantom in diffuse fields. Numerical simulations of the phantom is performed to validate the experimental approach. Afterward, we apply the

methodology to determine the absorption cross section of a human adopting several postures in the RC. The next chapters will be an application of this chapter, i.e., we determine the reverberation time values and the human's exposure in realistic indoor environments.

In Chapter 3, the properties of the room electromagnetics are investigated in realistic indoor offices. We determine the reverberation time values in several office environments in Ghent (Belgium), and in Aalborg (Denmark), using the virtual Multiple-Input Multiple-Ouput (MIMO) channel sounder and the real channel sounder. Next, the reverberation time values allows us the direct measurement of the absorption cross section (of humans) in diffuse fields in a realistic office.

In Chapter 4, we address - for the first time - an experimental method to determine the whole-body averaged specific absorption energy rate (SAR_{wb}) of humans under realistic conditions in indoor environments, i.e., presence of diffuse fields. Several scenarios have been considered and we show that the diffuse fields contribute significantly (under certain circumstances) to the total power involved in indoor environments. We show that the contribution of the diffuse fields in the absorption rate of humans may be prominent and cannot be systematically neglected.

In the previous chapters, we have evidenced the absorption cross section in diffuse fields and proposed an experimental approach to determine humans' absorption rate. However, the experimental method on one hand may be difficult and long as it requires measurements with antennas, network analyzer, cables, and other equipments. On the other hand, simulation of the diffuse fields in numerical tools would be expensive in terms of time and memory resources. Therefore, Chapter 5 proposes a simple formula with few parameters (as an alternative to numerical and experimental approaches) to determine the total SAR_{wb} of humans under realistic propagation scenarios, i.e., presence of diffuse fields and a possible Line-Of-Sight (LOS) component. The developed formula is validated via numerical simulations of four 3-D heterogeneous human models. The formula can be used to determine the absorption rate of humans under LOS and/or diffuse illumination. Furthermore, the formula can be used in dosimetry studies to assess accurately and rapidly the absorption rate of humans under realistic propagation conditions in realistic indoor environments.

Chapter 6 translates the room electromagnetics into an R-C electrical circuit so that it can determine the power densities in an indoor environment via the energy's discharge in a capacitance. The theory addresses the Ultra Wide Band (UWB) and Wireless Local Area Networks (WLAN) systems. We find that the absorption due to diffuse fields is larger in WLAN systems than in UWB systems. The circuit model can be embedded into circuit simulators.

Finally, Chapter 7 concludes this work and opportunities for future research are proposed.

<div style="text-align: right">

1

</div>

Introduction

1.1 Context and motivation

The telecommunication systems have nowadays become an important component in people's life. This is because the use of Information Communication Technologies (ICT) has a huge impact on several aspects of human activities, including the social, cultural, economical, and educational activities, etc. Therefore, the use of telecommunication systems has increased tremendously in recent years as illustrated in Fig. 1.1.
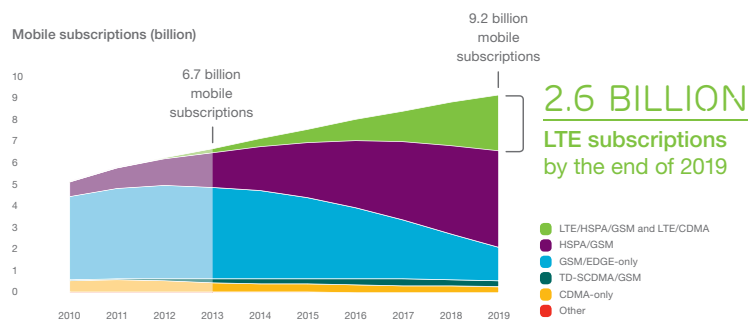
Figure 1.1: Subscribers evolution across networks

The wired access systems are the twisted-pair telephone networks and the hybrid-fiber coax TV networks. The wireless telecommunication systems include the Global System for Mobile communications (GSM), Universal Mobile Telecommunications System (UMTS), Long Term Evolution (LTE) known as the third generation partnership project (3GPP) family technology [1]. These technologies offer voice communica-

tions, data exchanges, multimedia services, mobile internet, etc.

Moreover, the advent of the wireless local area network (WLAN) systems increases the use of telecommunication devices and services in indoor environments such as the office rooms, classrooms, amphitheater, stores, residential environments, etc.

The massive success of the telecommunication systems stems for an important part from the satisfactory quality of service (QoS) experienced by the users. From a user's viewpoint, the QoS includes the coverage, the outage percentage or reliability, the data rate, etc. In order to meet the requirements of the expected QoS, researchers have to understand well the media through which the communication is established. Regarding the telecommunication systems, there are two types of media: the wired and wireless channel. In this thesis, we are only interested in the wireless channel. The understanding of the wireless channel is useful for the roll-out of new systems since this is exploited to predict the received signal and in turn the system capacity and coverage.

The wireless channel is very complex because the wireless signal encounters impairments that can distort and (seriously) attenuate it. In order to provide an accurate estimate of the received signal at a given location, it is important to consider propagation models that account as much as possible for all impairments undergone by the transmitted signal. In addition to the attenuation due to free-space propagation, the impairments are caused by reflections, diffractions or shadowing, scattering, absorption due to all objects along the propagation channel. In particular, the scattering process is very complex and gives rise to the diffuse multipath components (DMC) in indoor environments [2]. Recent studies in the propagation community have shown that wireless channels in indoor environments typically consist of a set of specular paths and diffuse multipath components [2, 3]. The DMC result from coherent and non-coherent reflections off scatterers present in indoor environments. The DMC represent the part of the channel which cannot be characterized with specular paths. In other words, the DMC are the remainder of the measured power delay profile (PDP) after removing the contribution of all specular paths. The existence and knowledge of the DMC has been used to improve significantly the radio channel models [4]. The characteristics of the DMC in an indoor environment were investigated in [3] for instance, where it has been shown that the contribution of the DMC to the total power may range from 10% up to 95%. Moreover, it has been shown that the diffuse fields contribute significantly to the channel capacity with contributions close to 100% in certain circumstances, showing that the diffuse fields can have a stronger influence on the channel capacity than the specular components. This is justified by the fact that the distributed scattered field has a wide angular spread at both the transmitter and receiver side [48]. Similarly, one may wonder whether the diffuse fields have an influence on the human's absorption due to electromagnetic radiation since the presence of the DMC has only recently been evidenced and the dosimetry community is usually not familiar with wireless channel propagation. Therefore, it is important to investigate how the absorption is influenced by the DMC. Moreover, reliable properties of diffuse fields have not yet been fully evidenced and have to be addressed as mentioned by [48].

The human absorption due to electromagnetic fields ought to account for the latest improvements and/or discovery made in the wireless channel modeling. Although the electromagnetic field (EMF) absorbed by humans in such circumstance is likely to be dependent of the DMC, its contribution to EMF's absorption is completely missing in the literature and must be carefully addressed. The contribution of the diffuse fields on human absorption is not yet investigated and should be addressed since the human exposure to electro-

magnetic fields has become of utmost importance for the international regulation authorities and/or local governments [5].

The topic of this dissertation deals with a new approach in determining the human exposure to electromagnetic fields in realistic indoor environments. This issue has been addressed by proposing a channel model that accounts for all interactions (specular reflections, diffuse scattering, etc.) occurring in indoor environments. The novelty of this dissertation resides in the fact that this is the first time that the diffuse scattered fields are accounted for in the human exposure to EMFs.

The objective of this dissertation is to investigate the effect of diffuse scattered fields on the human absorption and eventually take it into account.

1.2   Modeling of the wireless channels

The modeling of radio channels is mostly based on the implementation of the physical propagation phenomena. To this end, it is essential to identify and thoroughly understand underlying propagation mechanisms including the interaction with the physical objects present in the environment.

1.2.1   Physics of propagation

In wireless propagation, a transmitted signal is received by a receiver as a collection of plane waves or multipath components (MPCs). The MPCs stem from interactions of the transmitted signal with surrounding objects. These interactions occur because the wave impedance of the objects is different from the free-space impedance and therefore electromagnetic phenomena such as reflection, transmission (or absorption), diffraction, diffuse scattering, and/or any combination between them occur at each interaction [6–8]. An illustration of propagation mechanisms is shown in Fig. 1.2. After each interaction (denoted by *D, S, or R* in Fig. 1.2), the properties of the resulting wave (i.e., the magnitude, direction of propagation, phase, polarization) may change from the ones of the original impinging wave. This process goes on till the signal composed of multiple components produced by all reflections and scattering finally reaches the receiver. Therefore, one can easily understand that a multitude of MPCs will arise in realistic environments, particularly in indoor environments. This phenomena is called *multipath propagation* [6, 7]. *Reflection* occurs when an electromagnetic wave strikes upon a surface which dimensions are very large compared to the considered wavelength. Reflections generally occur from smooth surfaces such as flat walls, surface of the earth, facades of buildings, etc.

Diffraction occurs when the path - to reach a receiving point - of an incident electromagnetic wave is obstructed or shadowed by an impenetrable object. Based on the Huygen's principle [9, 10], secondary waves are formed in the shadowing region of the impeding object although there is no Line-Of-Sight (LOS) view between the transmitting and receiving points. Diffraction phenomena explain why radio-frequency (RF) signal can travel in urban or hilly environments without a LOS view.

Scattering occurs when the incident electromagnetic wave impinges on rough surfaces. Due to the surface's roughness and/or irregularities inside it, an electromagnetic wave incident on such surface results in several
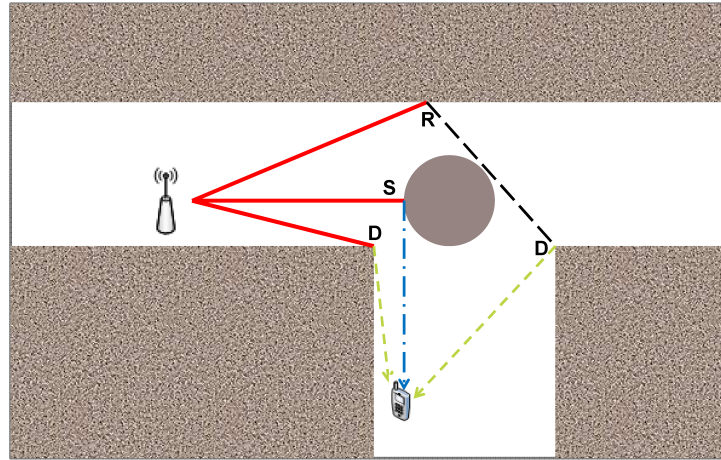
Figure 1.2: Illustration of the multipath propagation. Reflection (R, black line), Diffraction (D, green line), and Scattering (S, blue line)

reflected waves in many directions. The waves reflected in all directions - except the incident angle - are called the scattered waves. The roughness of a surface is determined by the Rayleigh criterion [11–13]. The scattering is the most difficult of the three propagation mechanisms because it involve the surface's details, all the directions, etc.

1.2.2 Physical channel models

Physical channel models aim at describing the wireless propagation in terms of parameters of the MPCs. Various parameters are associated with MPCs [8]:

– *time*: this parameter represents the variation of the channel over time. The variation of the channel is due to the motion of the transmitter/receiver and/or motion of the objects in the considered environment. The dynamic behavior of the wireless channel (in time) caused by the random motion of the transceiver and/or objects (or humans) is represented by the Doppler spectrum of the channel.

– *(time) delay*: due to the different MPCs arriving at the receiver side, each MPC arrives at the receiver with a different arrival delay, which in turn is proportional to the traveled path length.

– *direction of departure and arrival*: each MPC departs from the transmitter (Tx) with a direction referred to as direction of departure (DoD) and arrives at the receiver (Rx) with a direction referred to as direction of arrival (DoA). Each of these directions is specified by its elevation and azimuth angle in a spherical coordinates system. The DoD and DoA can be interpret as a directional distribution of the energy at the transmitter and receiver, respectively.

– *complex amplitude*: this expresses the magnitude and phase of the electric (or magnetic) field of the MPC at the position of the receiver. The phase is defined with respect to the field's phase at the

transmitting side. The squared magnitude of the complex amplitude is proportional to the power of the MPC.

Besides the parameters listed above, the orientation (or *polarization*) of the received electric (or magnetic) field is an important parameter of the MPC. The polarization properties of the MPC are managed by spitting the complex amplitude in three separate complex amplitudes, each corresponding to the orthogonal projection of the field on one of the three orthogonal directions in space.

Physical channel models are alluring as they provide physical insights (i.e., the MPCs and their characteristics) of the wireless propagation and are independent of the radiation patterns of the antennas at the transmit and receive side. Therefore, physical channel models are more suitable for the understanding and learning about the mechanisms of propagation. The physical models essentially characterize the double-directional impulse response of the channel and are mostly used for simulating system performance [8]. However, the main disadvantage of physical channel models is that they do not provide mathematical (analytical) solutions. We briefly review here some physical channel models.

Deterministic models

Deterministic channel models have been developed to determine numerically the received power at any location in an indoor environment so that all impairments encountered during the propagation of the transmitted wave are modeled in a deterministic way. These models are based on either the electromagnetic or ray approach. In the former solution, the Maxwell's equations (or other analytical formulations) are discretized and solved through numerical methods. However, this solution is time-consuming and the cost in terms of memory resources is extremely high since the entire environment has to be discretized in both space and time domains. Moreover, the cost increases as the dimensions of the environment and the frequency increase. In the latter solution (i.e., ray approach), the propagating field is computed as a set of direct and reflected wave(s) modeled with the Geometrical Optics (GO) theory. This approach is used in ray-tracing (RT) models [14–17]. The GO can be extended to treat diffraction by using e.g., the Geometrical Theory of Diffraction (GTD) or Uniform Theory of Diffraction (UTD). The contribution of an MPC (either a LOS, reflected, or diffracted signal) in an RT tool consists of the transmitted signal which is [8]:

– weighted by the radiation pattern of the Tx antenna,
– attenuated by the free-space loss, and possible additional losses due to the interactions with objects (i.e., walls, floor, ceiling, etc.),
– phase-shifted according to the relative path length of the LOS path with respect to the wavelength,
– weighted by the radiation pattern and the polarization mismatch at the receive terminal.

The RT models have been improved by accounting for the diffuse scattered fields [18–20]. Recently, the COST 2100 researchers have proposed a deterministic channel model for indoor environments [21]. The novelty of the COST 2100's model is that the diffuse scattering field is modeled and accounted for. This advanced RT model has been validated in [22, 23] where it turns out that including the diffuse fields in the classical RT tool enhances the estimation of the channel parameters such as the path loss, delay spread, etc. However, the accuracy of the advanced RT tool still resides in the accuracy of the input database which contains information such as the electromagnetic properties of the surfaces of the objects, the reflection and

scattering coefficients, the depolarization factor, etc. An exhaustive and complete input database requires excessive memory and computation time and is very difficult (if not impossible) to obtain. The RT models are also numerical based solutions and do not provide analytical means to analyze the behavior of the MPCs. Besides, these deterministic models are complex and are not primarily devoted to the propagation of diffuse scattered fields in indoor environments.

Empirical models

Empirical models are based on experiments and determine the parameters of MPCs through channel sounding in the considered environment. The channel sounding consists in exciting the wireless channel with a signal transmitted by a generator. The transmitted signal is further captured by a receiving antenna, and stored by an appropriate equipment such as a spectrum analyzer or a network analyzer. Measurement data obtained from the channel sounding require post-processing to retrieve the MPCs' parameters. The empirical models are useful for *a posteriori* simulation purposes. A non-exhaustive list of empirical models includes the (Extended) Saleh-Valenzuela model [24–26], the COST 259 directional channel model (DCM) [27, 28], and the COST 273 model [29].

Geometry-based channel models

Geometry-based models are stochastic models of the channel using a simplified ray-based approach. However, instead of modeling exactly the environment, the scatterers whose scattering properties are often modeled as complex Gaussian, are only specified by a spatial distribution. In a geometry-based stochastic channel model (GBSCM), a simplified description of the environment is created. This description might or might not try to look like the physical reality, but the positions of the possible scatterers are chosen according to a statistical distribution in both cases [21]. In the same way as for the ray-tracing models, GBSCMs include multi-antenna modeling and modeling of the temporal evolution of the channel. Movements of the Tx, Rx, and the scattering objects can also be described in a similar way as in the ray-tracing approach [21]. Examples of geometry-based stochastic channel models (GBSCM) are the one-ring model [8, 30, 31], and the double-ring model [8]. The most known GBSCMs are probably the Wireless world INitiative NEw Radio (WINNER) models [32], which have been widely used for evaluating the performance of MIMO transmission technologies in the next generation cellular systems such as the LTE [21].

1.2.3 Analytical channel models

While physical models aim at reconstructing the collection of MPCs (along with their parameters) present in the channel, analytical channel models do not describe the channel in terms of its propagation paths. Analytical models directly provide mathematical (or statistical) models for the complex channel transfer function between transmitting and receiving antennas [7, 8]. This channel transfer function is a function of one or more independent variables. Besides the mathematical expression of the channel transfer function, analytical channel models also allow the description of the spatial correlation properties of the MIMO channels' matrix. A major difference between analytical and physical channel models lies in the

fact that analytical models provide a mathematical framework but do not provide fully quantitative information. In particular, analytical model does not link the spatial correlation with geometrical or antenna parameters [8]. This means that analytical channel models include the antenna radiation pattern in their description, indicating that a change in antenna configuration requires that a different analytical model is used. Yet, analytical channel models are useful when analyzing mathematically the impact of correlations on any performance parameter. For instance, analytical channel models are used in space-time code design, forward error correction schemes, etc. Moreover, analytical models have been used to investigate the on-body propagation channels [33–36].

A non-exhaustive list of analytical channel models includes the Rayleigh fading channels, Ricean fading channels, dual-polarized channels, etc. The Rayleigh fading assumption is often used by MIMO system designers as it is the most realistic in environments rich of scatterers [8]. The Rayleigh channels correspond to modeling the narrowband transmission between a transmitting and receiving antenna as the sum of a large number of contributions with random and statistically independent phases, DoD, DoA [37]. In Wide Sense Stationary-Uncorrelated Scattering (WSS-US) Rayleigh fading channels, each individual channel is thus a zero-mean complex circularly symmetric Gaussian variable, or equivalently, a complex variable whose amplitude and phase respectively, are Rayleigh and uniformly distributed [8]. Wide sense stationary channels have the property that the channel correlation functions are invariant under a translation in time, i.e., the autocorrelation functions of a WSS channel depend only of $\Delta t = t_1 - t_2$ [37]. An uncorrelated scattering (US) channel is defined as a channel in which the contributions from elemental scatterers with different path delays are uncorrelated [37]. By analogy to WSS channels, the autocorrelation functions of US channels are invariant under a translation in the time-delay domain. This implies that the frequency correlation function of a US channel depends only on the frequency difference $\Delta f = f_1 - f_2$.

The Rayleigh channel models hold in mobile scenarios, as well as in deep-shadowed wireless links where the non-coherent contribution is prominent. However, there are scenarios where there may exist a strong coherent part, which does not experience any fading over time, i.e., a LOS component or one or several specular reflected components. This scenario leads to a Ricean distribution of the field amplitude. A thorough description of these models can be found in [8].

Analytical channel models are suitable to investigate the effect of the diffuse scattered fields on the human absorption as they provide a mathematical framework. We use in the following an analytical model that describes and models the diffuse scattered fields.

1.2.4 Dense/diffuse multipath components description and modeling

As previously mentioned, the impulse response of a wireless channel can be approximated by a superposition of discrete paths stemming from specular reflections. This approximation is widely used in urban and open environments. However, recent wireless channel investigations in indoor environments have evidenced that the superposition of discrete paths to model the channel do not characterize faithfully all the propagation mechanisms occurring in such environments. Such modeling neglects the contribution of the scattered and diffracted fields. The measured power delay profile (PDP) in an indoor environment and the reconstructed PDP from discrete paths is illustrated in Fig. 1.3.

7
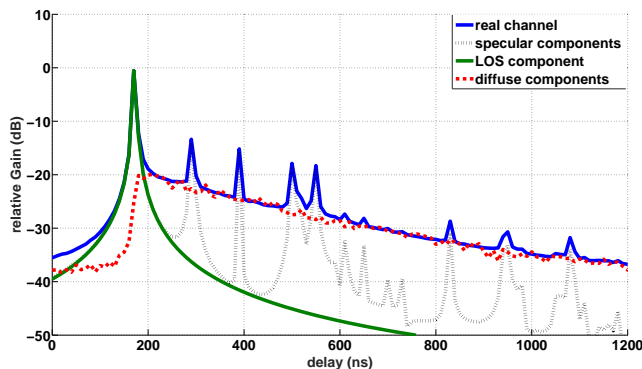
Figure 1.3: Example of a synthetic PDP (blue straight line), with the LOS component (green straight line), DMC (red dashed line), and the reconstructed PDP (black dotted line) from discrete or specular paths

The dense multipath components are considered as the remainder of the measured PDP after removing the contribution of all significant specular paths. Therefore, the dense multipath components are understood here as a set comprised of scattered and diffracted fields plus weak specular components that can not be estimated by the (high-resolution) estimation algorithms due to the limited bandwidth. Standard estimation algorithms such as the Estimation of Signal Parameters via Rotational Invariance Technique (ESPRIT), MUltiple SIgnal Classifier (MUSIC) [38], Space-Alternating Generalized Expectation-Maximization Algorithm [39] (SAGE), etc. can be used to estimate the characteristics of specular paths in a measured PDP if the number of paths is *a priori* known. The number of specular paths is determined with model order selection criteria such as the Minimum Description Length (MDL) [40–42]. These models fail in estimating the number of specular paths in measurement data if diffuse scattered fields are present [27]. This is because the data model used in model order selection criteria considers only specular paths plus AWGN whereas it has been shown that the DMC stem from a stochastic process and have to be taken into account in the data model [2].

Recent studies have shown that the wireless narrow band radio channel h can be considered as a superposition of deterministic specular components $s(\Theta_{sc})$ and stochastic dense multipath components $d(\Theta_{dmc})$, which include diffuse components [2, 43, 44] and noise. Here, Θ_{sc} and Θ_{dmc} are the set of parameters that fully describe the propagation mechanisms:

$$\mathbf{h} = \mathbf{s}(\Theta_{sc}) + \mathbf{d}(\Theta_{dmc}) + \mathbf{n} \tag{1.1}$$

where $\mathbf{h} \in \mathbb{C}^{M_f \times 1}$, $\mathbf{s}(\Theta_{sc}) \in \mathbb{C}^{M_f \times 1}$, $\mathbf{d}(\Theta_{dmc}) \in \mathbb{C}^{M_f \times 1}$, and $\mathbf{n} \in \mathbb{C}^{M_f \times 1}$ are the sampled version of an observation of the channel, the contribution of the specular paths, the contribution of the dense multipath components, and the additive measurement noise. M_f corresponds to the number of frequency points measured within the considered bandwidth. The contribution $\mathbf{s}(\Theta_{sc})$ is deterministic, whereas the contributions $\mathbf{d}(\Theta_{dmc})$ and $\mathbf{n}$ are both realizations of an independent and identically distributed (i.i.d) circular complex

normal distributed process expressed as follows: $\mathbf{d}(\Theta_{dmc}) \sim \mathcal{N}_c(0, \mathbf{R}(\Theta_{dmc}))$ and $\mathbf{n} \sim \mathcal{N}_c(0, \sigma_n^2 \mathbf{I})$, where σ_n^2, $\mathbf{I}$ are the noise variance, and the identity matrix of size $M_f \times M_f$, respectively. Here, $\mathcal{N}_c(\mathrm{m}, \mathbf{R})$ designates a complex circular symmetric Gaussian process with mean m and covariance matrix $\mathbf{R}$. Hence, the covariance matrix of the sampled channel can also be seen as corrupted colored noise and is solely dependent on the DMC and AWGN. Therefore, a channel observation is distributed according to

$$\mathbf{h} \sim \mathcal{N}_c(\mathbf{s}(\Theta_{sc}), \mathbf{R}(\Theta_{dmc}) + \sigma_n^2 \mathbf{I}) \in \mathbb{C}^{M_f \times 1} \tag{1.2}$$
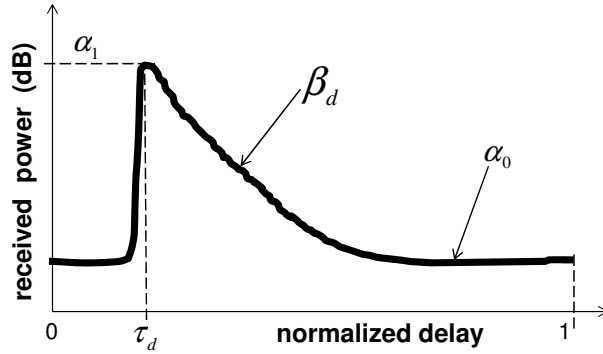
Figure 1.4: Diffuse multipath model in the delay domain

As illustrated in Fig. 1.4, the DMC power $\psi(\tau)$ as a function of time delay τ is described by an exponential decay:

$$\psi(\tau) = \alpha_1 e^{-\frac{(\tau - \tau_d)}{\tau_i}} + \alpha_0, \tag{1.3}$$

where α_0 is the noise floor in the measured PDP, τ_d is the arrival time of the first DMC, α_1 is the power of the DMC at $\tau = \tau_d$ (typically the highest value of the DMC in the PDP), and τ_i is the reverberation time of the room. α_1, τ_i, τ_d, and α_0 are the four parameters that fully describe the DMC and are gathered into the DMC parameter vector. This parametric description of the channel enables the use of maximum-likelihood high-resolution channel parameters estimation algorithms. A Maximum Likelihood Estimator (MLE) coined as RiMAX for the joint estimation of the parameters Θ_{sc} and Θ_{dmc} is proposed in [2, 43–45] where this topic is thoroughly addressed. The data model of the RiMAX estimation framework assumes that the DMC is Kronecker-separable in the spatial and frequency domains. Mathematically, the covariance matrix $R(\Theta_{dmc})$ has the following structure [2]:

$$R(\Theta_{dmc}) = I_{M_r} \otimes I_{M_t} \otimes R_f(\Theta_{dmc}) + \alpha_0 I_M \tag{1.4}$$

where I_k is the identity matrix of size k. M_t and M_r designate the number of transmit and receive antenna array ports respectively, and $M = M_t \times M_r \times M_f$. The frequency covariance matrix $R_f(\Theta_{dmc})$ is given by

$$R_f(\Theta_{dmc}) = toep(\kappa(\Theta_{dmc}), \kappa(\Theta_{dmc})^H), \tag{1.5}$$

9

where $\kappa(\Theta_{dmc}) \in \mathbb{C}^{M_f \times 1}$ is a sampled version of the power spectral density associated with (1.3), i.e., the Fourier transform of (1.3), and *toep*() is the Toeplitz-operator. The diffuse parameter Θ_{dmc} can be defined as $\Theta_{dmc} = [\tau_d\ \alpha_0\ \alpha_1\ \beta_d]$ where τ_d, α_0, α_1, β_d are the normalized base arrival delay of the diffuse components, the noise level, the power of the diffuse components at $\tau = \tau_d$, and the normalized coherence bandwidth of the diffuse components (proportional to τ_i). These parameters are illustrated in Fig. 1.4. If the parameters are time-variant, the extended Kalman Filter (EKF) is more suitable to track the time variations of the parameters [46, 47]. Although this analytical channel model describes and models the DMC, yet this approach is complicated and requires many parameters.

Finally, it should be noted that it is important to account for the diffuse contribution in the data model since recent studies have shown that the diffuse components may contribute significantly to the total power involved in realistic indoor environments [3, 4]. This has also been observed in [48] where it turned out that the contribution of the diffuse scattered fields in terms of received power varies between 10% and more than 95%, depending on the indoor scenario.

The next section proposes a hybrid channel model, i.e., analytical-empirical, so that the absorption due to the diffuse fields can be investigated in a simpler manner. The analytical-empirical modeling is a hybrid approach combining the advantages of both analytical and empirical models while avoiding many of their disadvantages. Moreover, this analytical-empirical modeling is a simple approach as it requires only one parameter describing the behavior of the diffuse scattered fields (see next Section).

1.3 Room electromagnetics

The *room electromagnetics* theory has first been developed in [49] in analogy with the well-known theory of room acoustics [50]. Here, we will briefly introduce some concepts of the room electromagnetics theory. Basically, the room electromagnetics describes the PDP in indoor environments as a superposition of two parts: a LOS component (if present) plus the rest, which is composed of the diffuse multipath components as shown in Fig. 1.5. This supposes that the (weak) specular contribution are neglected in the dense multipath components, hence yielding the diffuse multipath components. This assumption is supported by experimental observations where the contribution of the diffuse fields in the total power was prominent up to 90% or more [2–4, 48].

1.3.1 Theory and model

A very simple propagation model is obtained by considering an indoor environment as a lossy cavity where all the effective losses can be described with a single parameter. The theory of wide-band propagation in indoor environments is applied here, similar to studies in acoustics and reverberation chambers (RCs). The acoustics community has been applying the method [50] since the 1920's (known as Sabine's equation), but the fundamental difference to the electromagnetic case is the polarization [49].

The basic model is very simple and considers a first arriving LOS signal if present and next, multiple reflections, diffractions, and scatterings giving rise to a tail with an exponential decay in the received power as
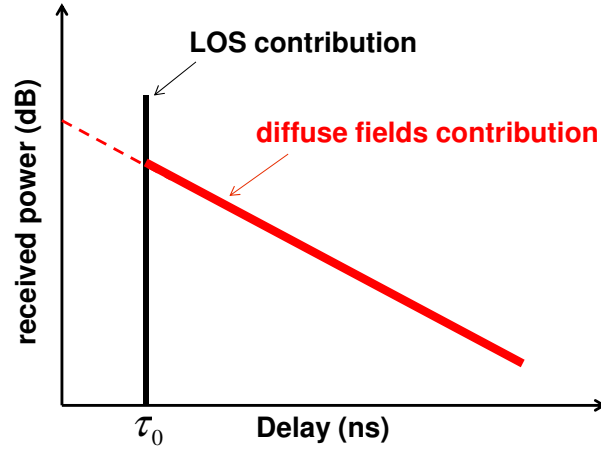
Figure 1.5: Power delay profile modeling in room electromagnetics theory.

a function of the arrival delay. The exponential decay of the received power in the delay domain in indoor environments has been experimentally observed in various works [2, 48, 49, 51]. The exponential decay has a time constant denoted as the *reverberation time*, similar to the acoustics case. It is important to mention that the uniform distribution of the electromagnetic energy in a room is the main assumption [50] for the validity of the expressions derived here.

Let's suppose a bundle of rays is selected within a small solid angle dΩ from all electromagnetic rays crossing an arbitrary point P as shown in Fig. 1.6.
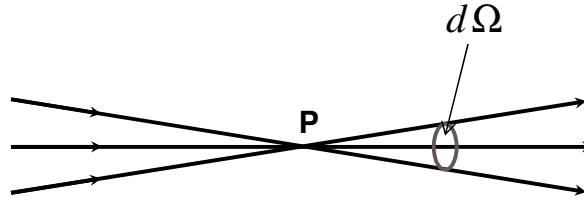
Figure 1.6: Bundle of nearly parallel rays

Since the ray tube is narrow, an intensity I(θ, φ)dΩ can be attributed to it with θ and φ describing its direction. The rays' intensity in the directions θ and φ is as follows:

$$dI(\theta,\varphi) = \frac{\left|E_\theta(\theta,\varphi)\right|^2 + \left|E_\varphi(\theta,\varphi)\right|^2}{2Z_0} \qquad (1.6)$$
$$= I(\theta,\varphi)d\Omega$$

where E is the peak electric-field strength value, and Z_0 is the free-space impedance. The corresponding

11

energy density is as follows:

$$
\begin{aligned}
dW(\theta, \varphi) \quad &= \frac{dI(\theta,\varphi)}{c_0} \\
&= \frac{I(\theta,\varphi)}{c_0} d\Omega
\end{aligned}
\tag{1.7}
$$

where $c_0 = 3 \times 10^8$ m/s is the velocity of light.

In total diffuse fields, the electromagnetic intensity is independent of the direction ($I(\theta, \varphi)=I$) due to the fields uniformity. The energy density in diffuse fields is found by integrating (1.7) over the whole sphere:

$$
W = 4\pi \frac{I}{c_0}
\tag{1.8}
$$

where W (watt.s/m^3), I (watt/m^2) are the energy density and the power density, respectively.

Assume now that the intensity in (1.6) is incident on a wall surface with area A. The total power absorbed by the wall is as follows:

$$
\begin{aligned}
P_{abs} \quad &= \eta A \int_{\varphi=0}^{2\pi} \int_{\theta=0}^{\pi/2} I(\theta, \varphi) \cos(\theta) \sin(\varphi) d\theta d\varphi \\
&= \eta A \pi I \\
&= \frac{c_0 \eta A}{4} W
\end{aligned}
\tag{1.9}
$$

where η is the average fraction of energy absorbed by the surfaces.

In (1.9), we use the relation between the power density and the energy density, i.e., (1.8).

If an input source power P(t) is transmitted in the room, and due to the law of energy conservation, the transmitted power is balanced by the increase in energy/second and the losses in the walls:

$$
P(t) = V \frac{dW}{dt} + \frac{c_0 \eta A}{4} W
\tag{1.10}
$$

The first and second term of the right side of (1.10) are the remaining power in the room and the power absorbed by walls, respectively. The general solution of (1.10) is a convolution integral:

$$
W_d(t) = \frac{1}{V} \int_0^\infty P(t - t') e^{-\frac{t'}{\tau}} dt'
\tag{1.11}
$$

where W_d(t) is the energy density in the room in Watt.s/m^3 and τ is the reverberation time of the room and defined in the next Section.

Electromagnetic reverberation time

If the source is turned off, i.e., P(t)=0 for t>0, (1.10) becomes an homogeneous equation with solution

$$
W(t) = W_0 e^{-\frac{t}{\tau}},
\tag{1.12}
$$

with

$$
\tau = \frac{4V}{c_0 \eta A}
\tag{1.13}
$$

where τ is the electromagnetic *reverberation time*, and depends solely on the room volume, absorption area, and absorption properties of the surfaces. It is identical to Sabine's equation in acoustics [50] except that the sound velocity is replaced by the light velocity.

From (1.12), the reverberation time is the damping factor of the diffuse fields. In other words, the reverberation time is the decay rate of the diffuse fields in the room. A large (resp. small) value of the reverberation time shows the slow (resp. fast) decay of the diffuse fields in the considered environment. If the energy density (or power) decay is translated in the decibels scale, the reverberation time is proportional to the slope (β_d) observed in the decay process shown in Figs. 1.4 and 1.5. The reverberation time is an important parameter in the modeling of the diffuse fields' power in indoor environments since it expresses its decay rate. In other words, the reverberation time indicates how fast the electromagnetic energy is absorbed by the materials and objects - humans included - in indoor environments.

Electromagnetic reverberation time in an occupied room

The reverberation time of (1.13) is determined for an empty room, in which only the flat surfaces (walls, ceiling, floor) are accounted for. We are interested in the expression of the reverberation time when one person is present in the room. If a person is present in the room, the total power absorbed is given by:

$$P_{abs}^{total} = P_{abs}^{walls} + P_{abs}^{human} \tag{1.14}$$

where P_{abs}^{walls} is the power absorbed by the surfaces (walls, ceiling, floor) and is defined in (1.9). P_{abs}^{human} is the power absorbed by a human present in the room and is defined as:

$$P_{abs}^{human} = \eta_h \int \int BSA(\theta, \varphi) I(\theta, \varphi) \cos(\theta) \sin(\varphi) d\theta d\varphi \tag{1.15}$$

where η_h and BSA are the fraction of energy absorbed by the human and its total Body Surface Area, respectively. Note that the integration is over half a sphere in the case of the walls, i.e., (1.9), while the whole sphere is considered here since we assume the human to be far from the walls. The term BSA(θ,φ) - the body surface area in a given direction - is difficult to obtain analytically. Therefore, assumptions are necessary to determine the power absorbed by a human, i.e., (1.15). Let us assume that the total body surface (accounting for all directions) of a human is comprised of its body surface from the front view plus its body surface from the back, which can be expressed as follows:

$$\begin{aligned} BSA \quad &= BSA_{front} + BSA_{back} \\ &= 2 \times BSA_{front} \end{aligned} \tag{1.16}$$

where it is assumed that BSA_{front} and BSA_{back} are equal. BSA_{front} is defined over half a sphere as for the case of the walls. We consider the human to be in a standing posture so that the BSA$_{front}$ can be approximated with a flat surface. The human model can be thought of as a rectangular cuboid as in [52].

If we now substitute (1.16) into (1.14), then the total power absorbed by the walls plus one human is:

$$
\begin{aligned}
P_{abs}^{total} \quad &= P_{abs}^{walls} + 2BSA_{front}\eta_h \int_{\varphi=0}^{2\pi} \int_{\theta=0}^{\pi/2} I(\theta, \varphi) \cos(\theta) \sin(\theta) d\theta d\varphi \\
&= \eta A \pi I + 2\eta_h \pi I BSA_{front} \\
&= (\eta A + \eta_h BSA)\pi I
\end{aligned}
\tag{1.17}
$$

Given the relation between the power and energy density in diffuse fields, i.e., (1.8), the power balance in the room becomes:

$$
P(t) = V\frac{dW}{dt} + \frac{c_0(\eta A + \eta_h BSA)}{4}W
\tag{1.18}
$$

Following the same procedure in Section 1.3.1, the reverberation time of the room with one person is expressed as:

$$
\tau = \frac{4V}{c_0(\eta A + \eta_h BSA)}
\tag{1.19}
$$

The reasoning can be extended to N persons in the room and the related reverberation time is given by

$$
\tau_N = \frac{4V}{c_0\left(\eta A + \eta_h \sum_{n=1}^{N} BSA(n)\right)}
\tag{1.20}
$$

where τ_N, N, and $BSA(n)$ are the reverberation time of the room occupied by N person(s), the total number of persons in the room and the body surface area of the nth person, respectively. We also assume here that the persons have the same absorption properties, which is characterized here by the average fraction of absorbed energy, i.e., η_h. The human absorption in diffuse fields is now included in the reverberation time via (1.20).

1.4 Human exposure to electromagnetic fields

1.4.1 Energy absorption and dosimetry

The coupling of RF energy into biological systems can be quantified by the induced electric and magnetic fields, power density, energy absorption, and the distribution and penetration into biological systems. The induced fields are the primary cause for biological effects of RF exposure, regardless of the mechanisms [53]. Restrictions on the effects of human exposure to EMF are based on established health effect such as temperature rise in tissues and are denoted as basic restrictions. Depending on the frequency, the physical quantities used to specify the basic restrictions on exposure to EMF are current density (or internal E-field), Specific energy Absorption Rate (SAR), and power density. Both the locally averaged SAR and the whole-body averaged SAR are considered by International Commission on Non-Ionizing Radiation Protection (ICNIRP) [5]. Protection against adverse health effects requires that the limitations on the basic restrictions are not exceeded. The basic restrictions metrics are frequency dependent and are defined as follows [5]. Between 1 Hz and 10 Hz, basic restrictions are provided in terms of internal fields to prevent effects on the

nervous system functions; between 100 Hz and 10 GHz, basic restrictions are defined in terms of whole-body averaged SAR to prevent whole-body heat stress and excessive localized tissue heating; and between 10 GHz and 300 GHz, basic restrictions are provided on the power density to prevent excessive heating in tissues or near the body surface. In any case, tissue heating is the accepted known effect of microwave radiation [53]. It is difficult to measure the temperature's rise in a human body. Furthermore, the use of temperature methods demands relatively high power to expose the tissue or human over a very short duration to avoid thermal diffusion errors [54]. Therefore, temperature methods are not applicable for low power transmitters. However, the initial temperature rise (when diffusion is not yet happening) due to RF energy in tissue is related to the SAR as follows [53–55]:

$$SAR = C\frac{\delta T}{\delta t} \tag{1.21}$$

where C is the specific heat of the tissue (J/(kg.K)), δT is the initial temperature rise (K) and δt (s) is the exposure duration. The incremental rise of the temperature in a tissue or a body can be determined if the related SAR is known [56–58].

The SAR is also defined [59] as the time derivative of the incremental energy δW (J) absorbed by (or dissipated in) an incremental mass δm (kg) contained in a volume element δV (m^3), of a given mass density ρ (kg/m^3):

$$SAR \quad = \frac{\delta}{\delta t}\left(\frac{\delta W}{\delta m}\right) \tag{1.22}$$

$$= \frac{\delta}{\delta t}\left(\frac{\delta W}{\rho\delta V}\right) \tag{1.23}$$

$$= \frac{\sigma E^2}{\rho} \tag{1.24}$$

$$= \frac{ACS\times I}{m} \tag{1.25}$$

where σ is the conductivity of tissue (S/m), and E is the rms value of the electric field (V/m). ACS and m designate the absorption cross section and the incident power density, respectively. The absorption cross section can be thought of as the body surface absorbing electromagnetic radiation and is detailed in the next chapter. Therefore, the SAR is expressed in W/kg. In other words, the SAR can be defined as the absorbed power per unit of mass.

It has been shown that a temperature increase of 1°C (which can cause health effects) corresponds to a whole-body averaged SAR of approximately 4 W/kg for about 30 minutes. With a safety factor of 10, a whole-body averaged SAR of 0.4 W/kg (averaged over any 6-minutes period) has been chosen as the restriction that provides adequate protection for occupational exposure. An additional safety factor of 5 is introduced for exposure of the general public, i.e., a whole-body averaged SAR limit of 0.08 W/kg [5]. Basic restrictions for the whole-body averaged SAR and localized SAR are provided to prevent whole-body heat stress and excessive localized tissue heating, respectively.

According to the ICNIRP [5], dosimetry is the measurement or determination by calculation of internal electric field strength or induced current density, and of SAR, or specific absorption rate distribution, in humans or animals exposed to electromagnetic fields. The SAR will depend on the characteristics of the exposed person (mass, morphology, absorption properties, etc.) and the exposure condition as well since

the absorbed power is proportional to the exposed surface area and the incident power (or energy) density. A phantom is often used for experimental dosimetry of a human body exposed to RF fields [59]. The availability of numerical voxel models is one of the recent advances made in the RF dosimetry.

1.5 Main research contributions and outline

Several works [58, 60–70] have investigated the whole-body averaged SAR (SAR$_{wb}$) using realistic numerical human models (or phantoms) and the finite-difference time-domain (FDTD) method [71]. However, all these studies and other current investigations of the SAR$_{wb}$ only address the exposure of human to specular or discrete plane wave(s). Usually, the SAR is investigated for a single or limited number of incident plane waves. Given the recent research of diffuse fields using channel measurement data in indoor environments (see Section 1.2.4), it is needed to investigate and determine the contribution of diffuse scattered fields to the SAR$_{wb}$ in such environments. This issue is completely missing in the literature of dosimetry.
To this end, the *room electromagnetics* theory has been used to investigate the human absorption in diffuse fields. This section lists the chapters of this dissertation. Each chapter led to a peer-reviewed publication in an international journal.

- Chapter 2 is focused on a particular case of environments, i.e., reverberation chamber (RC). Such chambers can be considered as an extreme case for which the diffuse scattered fields are dominant. The RC is an ideal reference for realistic indoor environments where the diffuse field is prominent. First, the chapter presents an easy-to-implement method to experimentally determine the reverberation time in such environments. Also, the difference between the absorption cross section in diffuse fields and the absorption cross section due to specular path(s) is explained. Second, a method to estimate the absorption cross section of various objects (or phantoms) in diffuse fields from reverberation time measurements is introduced. Further, numerical results in terms of diffuse absorption cross section validate the experimental methodology. The measurements in the RC highlight some properties of the diffuse fields that we use during the simulations. Finally, the method is applied to determine the absorption cross section in diffuse fields of a real human adopting different postures in the reverberation chamber. This second chapter is central, as all the remaining chapters derive from this chapter. **[AB4]**

- Chapter 3 continues the investigation of experimental setups capable of emulating the scattered fields but now moved away from the rather extreme metallic box used for the RC into the *real environment*. This chapter is an application of the Chapter 2. The reverberation time values of realistic indoor offices are characterized for several office environments in Ghent (Belgium) and in Aalborg (Denmark), using both a virtual Multiple-Input Multiple-Output (MIMO) channel sounder and a real MIMO channel sounder. From these numbers, the absorption cross sections of humans in realistic offices are determined. Experimental investigations show that the setup and the results are rather independent of the measurement system and antennas used. **[AB1]**

- Chapter 4 extends the results of chapter 3 to determine the whole-body averaged specific energy absorption rate of human beings. This chapter is the core of the dissertation in the sense that we develop an experimental setup to assess the human absorption rate in realistic complex indoor environments without huge computations. The method can be used if sufficient distance is encountered to have the

object or phantom in the far-field. The novel part is the inclusion of the diffuse scattered fields. We show that its contribution in the total whole-body SAR$_{wb}$ increases significantly with the distance between the transmitter and the phantom. We conclude that for large distances, diffuse fields should not be neglected when estimating the whole-body SAR$_{wb}$. The results of this chapter have been validated with FDTD simulations. **[AB2]**

– Chapter 5 introduces an expression (as an alternative to numerical and experimental approaches) to determine the full body SAR in typical environments for the typical frequencies used for mobile and wireless communications. We propose a simple expression to determine the SAR$_{wb}$ of humans solely based on their mass and the incident power densities. The developed formula is validated via numerical simulations of four 3D heterogeneous human models. The formula mainly avoids simulations of the absorption due to diffuse fields, as these are extremely expensive in terms of time and memory resources. The theoretical background is based on ellipsoid analysis and a limited number of simulations. This chapter makes the thesis very much applicable to practical scenarios. **[AB5]**

– Chapter 6 proposes a translation of the room electromagnetics theory into a circuit model. By applying (fast) circuit solvers, a complex electromagnetic problem can be calculated in this way. A new electrical circuit model to determine the exposure due to the diffuse fields is developed and can be used to determine human absorption in realistic indoor environments. Moreover, we show the difference between narrow-band and ultra-wide-band systems in terms of absorption due to diffuse fields. Such a simplified expression may be used by many not capable to or willing to get involved with the full wave simulations. **[AB3]**

– Finally, Chapter 7 summarizes this dissertation and addresses futures research.

1.6 Publications

1.6.1 Publications in International Journals (A1)

[AB1] **A. Bamba**, W. Joseph, J. B. Andersen, E. Tanghe, G. Vermeeren, D. Plets, J. Ø. Nielsen, and L. Martens, "Experimental Assessment of Specific Absorption Rate Using Room Electromagnetics" *IEEE Trans. Electromagn. Compat.*, vol. 54, no. 4, pages 747-757, 2012.

[AB2] **A. Bamba**, W. Joseph, G. Vermeeren, E. Tanghe, D. P. Gaillot, J. B. Andersen, J. Ø. Nielsen, M. Liénard, and L. Martens, "Validation of Experimental whole-body SAR Assessment Method in a Complex Environment" *Bioelectromagnetics*, vol. 34, no. 2, pages 122-132, 2013.

[AB3] **A. Bamba**, W. Joseph, E. Tanghe, G. Vermeeren, and L. Martens, "Circuit Model for Diffuse Multipath and Electromagnetic Absorption Prediction in Rooms" *IEEE Trans. Antennas Propag.*, vol. 61, no. 6, pages 3292-3301, 2013.

[AB4] **A. Bamba**, D. P. Gaillot, E. Tanghe, W. Joseph, M. Liénard, and L. Martens, "Assessing Human Whole-Body Specific Absorption Rate For diffuse Exposure From Reverberation Chamber Measurements" *IEEE Trans. Electromagn. Compat.*, accepted for publication, 2014.

[AB5] **A. Bamba**, W. Joseph, G. Vermeeren, A. Thielens, E. Tanghe, and L. Martens, "A Formula for human Average Whole-Body SAR Under Diffuse Fields Exposure in the GHz Region" *Phys. Med. Biol.*, vol. 59, pages 7435-7456, 2014.

[AB6] **A. Bamba**, M. T. Martinez-Ingles, D. P. Gaillot, E. Tanghe, B. Hanssens, J. M. Molina-Garcia-Pardo, M. Liénard, L. Martens, and W. Joseph, "Experimental Investigation of Electromagnetic Reverberation Characteristics as a function of UWB Frequencies" *IEEE Antennas Wireless Propag. Lett.*, vol. 14, pages 859-862, 2015.

1.6.2   Publications in International Conferences (P1)

[AB7] **A. Bamba**, W. Joseph, D. Plets, E. Tanghe, G. Vermeeren, L. Martens, J. B. Andersen, and J. Ø. Nielsen, "Assessment of Reverberation Time by Two Measurement Systems for Room Electromagnetics Analysis" in *IEEE International Symposium on Antennas and Propagation* (APS-URSI), Spokane, WA, US, 3-8 July 2011, pages 3113-3116, DOI:10.1109/APS.2011.5997191

[AB8] **A. Bamba**, J. B. Andersen, W. Joseph, D. Plets, E. Tanghe, G. Vermeeren, J. Ø. Nielsen and L. Martens, "Experimental Specific Energy Absorption Rate Assessment from Absorption Cross Section Measurement for Far-field Exposure at 2-3 GHz" in 33rd *Annual Meeting of the Bioelectromagnetics Society*, Halifax, Canada, 12-17 June 2011, http://hdl.handle.net/1854/LU-2039783

[AB9] **A. Bamba**, W. Joseph, G. Vermeeren, E. Tanghe, and L. Martens, "The DMC Contribution in the Human Absorption in an Indoor Environment" in *IEEE 6th European Conference on Antennas and Propagation* (EUCAP), *Proceedings*, Prague, Czech Republic, pages 460-462, 2012

[AB10] **A. Bamba**, E. Tanghe, W. Joseph, G. Vermeeren, D. Plets, and L. Martens, "Theory for Exposure Prediction in an Indoor Environment due to UWB Systems" in *IEEE Antennas and Propagation Society International Symposium* (APS-URSI), Chicago, IL, USA, 8-14 July 2012, pages 1-2, DOI: 10.1109/APS.2012.6348684

[AB11] **A. Bamba**, W. Joseph, G. Vermeeren, E. Tanghe, and L. Martens, "Validation of the Experimental whole-Body SAR Assessment Method in a Complex Indoor Environment" in 34th *Annual Meeting of the Bioelectromagnetics Society, Proceedings*, Brisbane, Australia, 17-22 June 2012, pages 320-322

[AB12] **A. Bamba**, W. Joseph, E. Tanghe, L. Martens, D. P. Gaillot, and M. Liénard, "Determination of the whole-body Absorption Cross Section of a Phantom using RiMAX" in *IEEE Antennas and Propagation Society International Symposium* (APS-URSI), Orlando, FL, USA, 7-13 July 2013, pages 716-717, DOI:10.1109/APS.2013.6711018

[AB13] F. Heereman, W. Joseph, E. Tanghe, D. Plets, **A. Bamba**, L. Verloock and L. Martens, "Performance loss due to multipath propagation for IEEE 802.11 systems" in 7th *European Conference on Antennas and Propagation* (EUCAP), Gothenburg, Sweden, 8-12 April 2013, pages 2610-2613

[AB14] B. Hanssens, M. Martnez-Ingls, **A. Bamba**, E. Tanghe, J. M. Molina-Garcia-Pardo, D. P. Gaillot, M. Liénard, C. Oestges, L. Martens, and W. Joseph, "Estimation of Room Electromagnetics Reverberation Time for Ultra-Wideband Indoor Channels" in 8th *European Conference on Anten-*

nas and Propagation (EUCAP), The Hague, The Netherlands, 6-11 April 2014, pages 527-528, http://hdl.handle.net/2078.1/143112

[AB15] **A. Bamba**, W. Joseph, G. Vermeeren, E. Tanghe, L. Martens, "Expression for Human Whole-Body Averaged SAR of Adults For Single Plane Wave Exposure" in 8th *European Conference on Antennas and Propagation* (EUCAP), The Hague, The Netherlands, 6-11 April 2014

[AB16] **A. Bamba**, M. T. Martinez-Ingles, D. P. Gaillot, E. Tanghe, B. Hanssens, J. M. Molina-Garcia-Pardo, M. Liénard, L. Martens, and W. Joseph, "Experimental Investigation of the Characteristics of the Electromagnetic Reverberation in the UWB Frequency Bands" in *IEEE Antennas and Propagation Society International Symposium* (APS-URSI), Memphis, TN, USA, 6-11 July 2014, pages 1181-1182, DOI:10.1109/APS.2014.6904917

References

[1] 3rd generation partnership project (3gpp).

[2] A. Richter. *"Estimation of Radio Channel Parameters: Models and Algorithms"*. PhD thesis, Faculty of electrical Engineering and Information Technology at the Technical University. Ilmenau, Germany., 2005.

[3] J. Poutanen, J. Salmi, K. Haneda, V. M. Kolmonen, and P. Vainikainen. "Angular and Shadowing Characteristics of Dense Multipath Components in Indoor Radio Channels". *IEEE Trans. Antennas Propag.*, 59: pages 245–253, 2011.

[4] N. Czink, A. Richter, E. Bonek, J. P. Nuutinen, J. Ylitalo. "Including Diffuse Multipath Parameters in MIMO Channel Models". In *IEEE 66th Vehicular Technology Conference (VTC)- Fall.*, 2007.

[5] ICNIRP. "Guidelines for limiting exposure to time-varying electric, magnetic, and electromagnetic fields (up to 300 GHz)". *Health Physics*, 74 (4): pages 494–522, 1998.

[6] J. B. Andersen, T. S. Rappaport, and S. Yoshida. "Propagation Measurements and Models for WiWireless Communications Channels". *IEEE Trans. Antennas Mag.*, pages pages 42–49, 1995.

[7] S. R. Saunders, and A. A. Zavala. *"Antennas and Propagation for Wireless Communication Systems"*. John Wiley & Sons Inc., New York, NY, 1999.

[8] Claude Oestges and Bruno Clerckx. *"MIMO Wireless Communication: From Real-World Propagation to Space-Time Code Design"*. Academic Press, first edition, 2007.

[9] C. Huygens. "Traité de la lumière (Leyden, 1690)". 1690. English translation by S. P. Thompson, Treatise on Light (MacMillan, London, 1912).

[10] D. A. B. Miller. "Huygens's wave propagation principle corrected". *Optics Letters*, 16 (18): pages 1370–1372, 1991.

[11] O. Landron, M. J. Feuerstein, and T. S. Rappaport. "In Situ Microwave Reflection Coefficient Measurements for Smooth and Rough Exterior Wall Surfaces". In *43rd IEEE Vehicular Technology Conference, Secaucus, NJ, USA*, 1993.

[12] F. Delfino, P. Girdinio, L. Minervini, M. Nervi. "Electromagnetic plane wave scattering from building surfaces". *COMPEL - The international journal for computation and mathematics in electrical and electronic engineering*, 25 (4): pages 1007–1018, 2006.

[13] R. Piesiewicz, C. Jansen, D. Mittleman, T. Kleine-Ostmann, M. Koch, and T. Kürner. "Scattering Analysis for the Modeling of THz Communication Systems". *IEEE Trans. Antennas Propag.*, 55 (11): pages 3002–3009, 2007.

[14] K. R. Shaubach, N. J. Davis, and T. S. Rappaport. "A ray tracing memethod for predicting path loss and delay spread in microcellular environments". In *42th Vehicular Technology Conf.*, pages pages 932–935, Denver, CO, May 1992.

[15] P. Daniele, V. Degli-Esposti, G. Falciasecca, and G. Riva. "Field prediction tools for wireless communications in outdoor and indoor environments". In *IEEE MTT-S Eur. Topical Congress, Turin, Italy, pages 129-134*, 1994.

[16] M. C. Lawton and J. P. McGeehan. "The application of a deterministic ray launching algorithm for the prediction of radio channel characteristics in small-cell environments". *IEEE Trans. Veh. Technol.*, 43: pages 955–969, 1994.

[17] G. Liang and H. L. Bertoni. "A new approach to 3D ray tracing for propagation in cities". *IEEE Trans. Antennas Propag.*, 46: pages 853–863, 1998.

[18] V. Degli-Esposti. "A Diffuse Scattering Model for Urban Propagation Prediction". *IEEE Trans. Antennas and Propag.*, 49 (7): pages 1111–1113, 2001.

[19] V. Degli-Esposti, F. Fuschini, E. M. Vitucci, and G. Falciasecca. "Measurement and Modeling of Scattering From Buildings". *IEEE Trans. Antennas Propag.*, 55 (1): pages 143–153, 2007.

[20] M. Kwakkernaat and M. Herben. "Modeling angular dispersion in ray-based propagation prediction models ". Technical report, Trondheim, Norway, 2008. Technical Report TD(08)519.

[21] R. Verdone and A. Zanella. *"Pervasive Mobile and Ambient Wireless Communications"*. Springer, 2012.

[22] F. Mani and C. Oestges. "Evaluation of diffuse scattering contribution for delay spread and cross polarization ratio prediction in an indoor scenarios". Technical report, Proc. 4th European Conference on antennas and Propagation (EuCAP), Barcelona, Spain, April 2010. Also available as TD(09)812.

[23] F. Mani, F. Quitin, and C. Oestges. "Evaluation of diffuse scattering contribution in office scenarios". Technical report, Athens, Greece, 2010. Technical Report TD(01)10001.

[24] A. A. M. Saleh and R. Valenzuela. "A Statistical Model for Indoor Multipath Propagation". *IEEE J. Select. Areas Commun. JSAC*, pages pages 128–137, 1987.

[25] Q. H. Spencer, B. D. Jeffs, M. A. Jensen, and A. L. Swindlehurst. "Modeling the statistical time and angle of arrival characteristics of an indoor multipath channel.". *IEEE J. Select. Areas Commun.*, 18(3): pages 347–360, March 2000.

[26] J. W. Wallace and M. A. Jensen. "Modeling the indoor MIMO wireless channel". *IEEE Trans. Antennas Propagat.*, 50(5): pages 591–599, May 2002.

[27] M. Steinbauer, A. F. Molisch, and E. Bonek. 'The double-directional radio channel". *IEEE Antennas Propagat. Mag.*, 43(4): pages 51–63, August 2001.

[28] L. M. Correia. *"COST 259-Wireless flexible personalized communications"*. Wiley, London, UK, 2001.

[29] L. M. Correia. *"COST 273-Towards mobile broadband multimedia networks"*. Elsevier, London, UK, 2006.

[30] D. S. Shiu, G. J. Foschini, M. J. Gans, and J. M. Kahn. "Fading correlation and its effect on the capacity of multielement antenna systems". *IEEE Trans. Commun.*, 48 (3): pages 502–513, March 2000.

[31] A. Abdi and M. Kaveh. "A space-time correlation model for multielement antenna systems in mobile fading channels". *IEEE J. Select. Areas Commun.*, 20 (4): pages 550–560, April 2002.

[32] P. Kyösti, J. Meinilä, L. Hentilä, X. Zhao, T. Jämsä, C. Schneider, M. Narandzić, M. Milojević, A. Hong, J. Ylitalo, V.-M. Holappa, M. Alatossava, R. Bultitude, Y. de Jong, and T. Rautiainen. "WINNER II Channel Models". Technical report, September 2007. IST-4-027756 WINNER II Deliverable 1.1.2. v.1.2, Technical Report, IST-WINNER II.

[33] G. Roqueta, A. Fort, C. Craeye, and C. Oestges. "Analytical propagation models for body area networks". *In IET Seminar on Antennas and Propagat. for Body-Centric Wireless Commun.*, 24: pages 90–96, April 2007.

[34] A. Fort, F. Keshmiri, G. R. Crusats, C. Craeye, and C. Oestges. "A body area propagation model derived from fundamental principles: Analytical analysis and comparison with measurements". *IEEE Trans. Antennas Propag.*, 58 (2): pages 503–513, February 2010.

[35] L. Liu, F. Keshmiri, C. Craeye, P. De Doncker, and C. Oestges. "An analytical modeling of polarized time-variant on-body propagation channels with dynamic body scattering". *"EURASIP J. Wireless Commun. Networking"*, 2011. Article ID 362521, 2011. doi:10.1155/2011/362521.

[36] D. Ma, and W. X. Zhang. "Analytic Propagation Model for Wireless Body-Area Networks". *IEEE Trans. Antennas Propag.*, 59 (12): pages 4749–4756, December 2011.

[37] J. D. Parsons. *"The Mobile Radio Propagation Channel"*. 2nd ed., Wiley,West Sussex, 2000.

[38] T. K. Moon and W. C. Stirling. *"Mathematical Methods and Algorithms for Signal Processing"*. Prentice Hall, Upper Saddle River, New Jersey 07458, 1999.

[39] Jeffrey A. Fessler, Alfred O. Hero. "Space-Alternating Generalized Expectation-Maximization Algorithm". *IEEE Trans. Sig. Process.*, 42: pages 2664–2677, 1994.

[40] J. Rissanen. "Modeling by shortest data description". *Automatica*, no. 14: pages 465–471, 1978.

[41] M. Wax and T. Kailath. "Detection of Signals by Information Theoretic Criteria". *IEEE Trans. Acoust., Speech, Signal Processing*, 33 (2): pages 387–392, 1985.

[42] M. H. Hansen, B. Yu. "Model Selection and the Principle of Minimum Description Length". *Journal of the American Statistical Association*, 96 (454): pages 746–774, 2001.

[43] A. Richter, M. Landmann, R.S. Thoma. "Parameter Estimation Results of Specular and Dense Multipath Components in Micro- and Macro-Cell Scenarios". In *International Symp. on Wireless Personal and Multimedia Communication (WPMC)*, Abano Terme, Italy, September 2004.

[44] A. Richter, and R. S. Thoma. "Joint Maximum Likelihood Estimation of Specular Paths and Distributed Diffuse Scattering". In *61st IEEE Vehicular Technology Conference (VTC) Spring*, pages pages 11–15 vol. 1., 2005.

[45] R. Thomä, M. Landmann, A. Richter. "RIMAX - a Maximum Likelihood Framework for Parameter Estimation in Multidimensional Channel Sounding". In *Int. Symp. on Antennas and Propagation*, Sendai, JP, August 17-21 2004.

[46] A. Richter, M. Enescu, and V. Koivunen. "State-space approach to propagation path parameter estimation and tracking". In *Proc. 6th IEEE Workshop on signal Processing Advances in Wireless Communications*, New York City, June 2005.

22

[47] J. Salmi, A. Richter, M. Enescu, P. Vainikainen, and V. Koivunen. "Propagation Parameter Tracking using Variable State Dimension Kalman Filter". In *Proc. IEEE VTC-2006 spring*, Melbourne, Australia, May 7-10 2006.

[48] A. Richter, J. Salmi, V. Koivunen. "Distributed scattering in radio channels and its contribution to mimo channel capacity". In *First European Conference in Antennas and Propagation (EuCAP 2006), Nice, France.*, 2006.

[49] J. B. Andersen, J. Ø. Nielsen, G. F. Pedersen, G. Bauch, and M. Herdin. "Room Electromagnetics". *IEEE Antennas Propagat. Mag.*, 49, (2): pages 27–33, 2007.

[50] H. Kuttruff. *"Room Acoustics"*. Spon Press, London, 2000.

[51] J. B. Andersen, K. L. Chee, M. Jacob, G. F. Pedersen, T. Kürner. "Reverberation and Absorption in an Aircraft Cabin with the Impact of Passengers". *IEEE Trans. Antennas and Propag.*, 60 (5): pages 2472–2480, 2012.

[52] A. Hirata, Y. Nagaya, F. Osamu, T. Nagaoka, S. Watanabe. "Correlation between Absorption Cross Section and Body Surface Area of Human for Far-Field Exposure at GHz Bands". *Electromagnetic Compatibility, 2007. EMC 2007. IEEE International Symposium on*, pages 1–4, July 2007.

[53] "Recommended Practice for the Measurement of Potentially Hazardous Electromagnetic Fields - RF and Microwave". Technical report, American National Standards Institute (ANSI), New York, NY 10017, 1992. ANSI/IEEE C95.3-1992. Copyright 1992, The Institute of Electrical and Electronics Engineers, Inc. (IEEE).

[54] D. L. Means and K. W. Chan. "Evaluating Compliance with FCC Guidelines for Human Exposure to Radiofrequency Electromagnetic Fields". Technical report, Federal Communications Commission Office of Engineering & Technology, 2001.

[55] Q. Balzano, O. Garay, and T. Manning. "Electromagnetic energy exposure of simulated users of portable cellular phones". *IEEE Trans. Veh. Technol.*, 44 (3): pages 390–403, 1995.

[56] P. Bernardi, M. Cavagnaro, R. Cicchetti, S. Pisa, E. Piuzzi, O. Testa. A UTD/FDTD investigation on procedures to assess compliance of cellular base-station antennas with human exposure limits in a realistic urban environment. *IEEE Trans. Micro. Theory Techn.*, 51: pages 2409–2417, 2003.

[57] A. Hirata, T. Asano, and O. Fujiwara. "FDTD analysis of human body-core temperature elevation due to RF far-field energy prescribed in the ICNIRP guidelines". *Phys. Med. Biol.*, 52: pages 5013–5023, 2007.

[58] J. F. Bakker, M. M. Paulides, A. Christ, N. Kuster, and G. C. van Rhoon. "Children and adults exposed to electromagnetic fields at the ICNIRP reference levels: theoretical assessment of the induced peak temperature increase". *Phys. Med. Biol.*, 56: pages 4967–4989, 2011.

[59] ICNIRP Standing Committee III, Task Group Physics, and Engineering. "Exposure to high frequency electromagnetic fields, biological effects and health consequences (100 kHz-300 GHz)". Technical report, International Commission on Non-Ionizing Radiation Protection (ICNIRP), 2009. Review of the scientific evidence on dosimetry, biological effects, epidemiological observations, and health consequences concerning exposure to high frequency electromagnetic fields (100 kHz to 300 GHz).

[60] P. J. Dimbylow. "Fine resolution calculations of SAR in the human body for frequencies up to 3 GHz". *Phys. Med. Biol.*, 47: pages 2835–2846, 2002.

[61] J. Wang, O. Fujiwara, S. Kodera and S. Watanabe. "FDTD calculation of whole-body average SAR in adult and child models for frequencies from 30 MHz to 3 GHz". *Phys. Med. Biol.*, 51: pages 4119–4127, 2006.

[62] P. Dimbylow, A. Hirata and T. Nagaoka. "Intercomparison of whole-body averaged SAR in European and Japanese voxel phantoms". *Phys. Med. Biol.*, 53: pages 5883–5897, 2008.

[63] G. Vermeeren, W. Joseph, C. Olivier, and L. Martens. "Statistical multipath exposure of a human in a realistic electromagnetic environment". *Health Physics*, 94, no. 4: pages 345–354, 2008.

[64] G. Vermeeren, W. Joseph and L. Martens. "Whole-body SAR in spheroidal adult and child phantoms in a realistic exposure environment". *IEE Electronics Letters (44)13:*, (44) 13: pages 790–791, 2008.

[65] E. Conil, A. Hadjem, F. Lacroux, M. F. Wong and J. Wiart. "Variability analysis of SAR from 20 MHz to 2.4 GHz for different adult and child models using finite-difference time-domain". *Phys. Med. Biol.*, 53: pages 1511–1525, 2008.

[66] S. Kühn, W. Jennings, A. Christ and N. Kuster. "Assessment of induced radio-frequency electromagnetic fields in various anatomical human body models". *Phys. Med. Biol.*, 54 (2009): pages 875–890, 2009.

[67] A. Hirata, N. Ito and O. Fujiwara. "Influence of electromagnetic polarization on the whole-body averaged SAR in children for plane-wave exposures". *Phys. Med. Biol.*, 54 (2009):N59–N65, 2009.

[68] A. El Habachi, E. Conil, A. Hadjem, E. Vazquez, M. F. Wong, A. Gati, G. Fleury and J. Wiart. "Statistical analysis of whole-body absorption depending on anatomical human characteristics at a frequency of 2.1 GHz". *Phys. Med. Biol.*, 55: pages 1875–1887, 2010.

[69] J. F. Bakker, M. M. Paulides, A. Christ, N. Kuster, and G. C. van Rhoon. "Assessment of induced SAR in children exposed to electromagnetic plane waves between 10 MHz and 5.6 GHz". *Phys. Med. Biol.*, 55: pages 3115–3130, 2010. Erratum in Phys. Med. Biol. 56(9) page 2883, 2011.

[70] T. Uusitupa, I. Laakso, S. Ilvonen and K. Nikoskinen. "SAR variation study from 300 to 5000 MHz for 15 voxels models including different postures". *Phys. Med. Biol.*, 55: pages 1157–1176, 2010.

[71] A. Taflove, S. Hagness. "Computational electrodynamics: The finite-difference time-domain method". *Artech. House, Norwood, MA, 3rd edition*, 2005.

2

Characterization of the absorption cross section due to diffuse fields from reverberation chamber measurements

2.1 Introduction

As introduced in Chapter 1, the room electromagnetics theory is applicable in environments where the diffuse fields are prominent. Under these circumstances, the reverberation time describes all the losses in indoor environments. An reverberation chamber (RC) emulates a rich isotropic multipath environment, which can be considered as an extreme reference for the realistic indoor environments where the scattered diffuse waves are prominent. Therefore, we investigate first the characteristics of the reverberation time in a RC. We showed in Section 1.3 of Chapter 1 that the reverberation time value is related to the surface area absorbing electromagnetic radiation in complete diffuse fields. Therefore, the reverberation time values are used to determine the absorption cross section of humans in diffuse fields via measurements in a RC. As an application, the methodology can be applied to determine the reverberation time and the absorption cross section of humans in realistic indoor offices in the next chapters. The knowledge of the absorption cross section is important toward the investigation of the human exposure to the electromagnetic fields.

Reverberation chambers [1–6] have been used for electromagnetic compatibility (EMC) measurements and for wireless channel characterization. A Stirred-Mode Reverberation Chamber (SM-RC) is a fully-closed metallic cavity which is oversized with respect to the investigated wavelength. It operates over a large frequency bandwidth (typically 1-18 GHz) depending upon its dimensions and volume. Due to the cavity effect, there exists a working volume sufficiently separated from the walls, wherein the electromagnetic fields are statistically uniform and isotropic for all measurement points, directions, and electromagnetic

emitting sources' positions. A rotation twisted metallic sheet inside the chamber provides the stirring of the electromagnetic waves' modes. This is known as the mechanical stirring. However, there exists other means of stirring the electromagnetic modes, e.g., the frequency stirring and reverberation chambers with vibrating walls. Fig. 2.1 shows an illustration of an RC. Further information and details about RCs can be found in [1, 2, 5, 7–10].
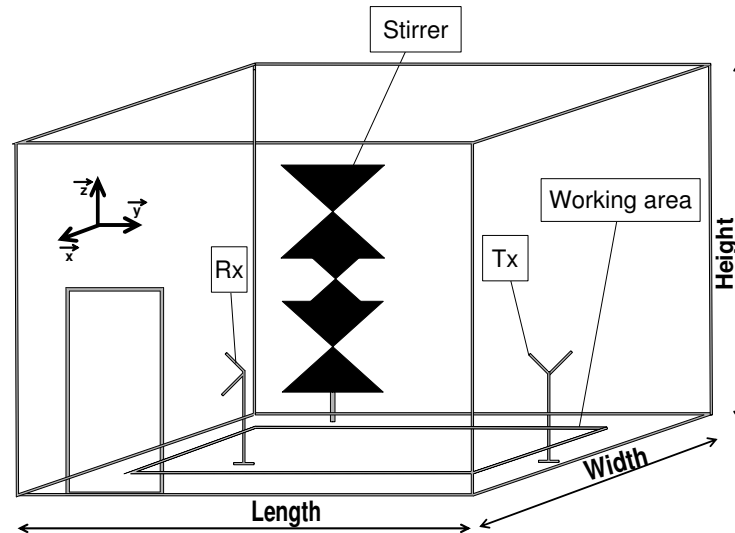
Figure 2.1: Illustration of a reverberation chamber

The different sources of losses inside an RC are well described in [2]. The plane-wave integral representation and properties in RCs are addressed in [3]. A statistical electromagnetic theory for the unstirred components of the electromagnetic fields (EMFs) in RCs is addressed in [4]. An RC can be used to emulate Rayleigh or Rician channels [5], along with the probability density function of the EMF. The multiple paths inside an RC are generated by multiple reflections of ElectroMagnetic Waves (EMWs) on the walls and on a mechanical paddle rotating in the chamber.

The characteristics of the multiple paths enhance the performance of the Multiple-Input Multiple-Output (MIMO) channels. Therefore, the RCs are more and more used for the characterization of MIMO channels [8, 11] and for the evaluation of the performance of wireless communication systems [9, 12]. In addition, RCs are also used to determine the mean absorption cross section (ACS_{mean}) of lossy objects. This information is critical when assessing an antenna's radiation efficiency when located close to lossy objects such as a head phantom [13]. The mean or average absorption cross section of a lossy object is also used to estimate the loading effects in terms of the average gain in radio frequency (RF) reverberating environments such as an aircraft passenger cabin [14]. The notion of the mean absorption cross section is clearly related to the performance of the reverberating environment in terms of averaged gain and *is different from the (whole-body) absorption cross section induced by diffuse fields* ($\text{ACS}_{wb,dmc}$). The ACS_{mean} is the averaged value of the ACS's values obtained for a single plane wave incident on a phantom or human with different direc-

tions and polarizations. Here, we introduce the ACS$_{mean}$ to show that it is different from the ACS$_{wb,dmc}$. The former has already been investigated [13–16] and is due to discrete electromagnetic ray(s) whereas the latter is due to diffuse (continuum) field and is missing in the literature. The knowledge of the whole-body absorption cross section induced by diffuse fields is critical with respect to the experimental investigation of human's specific absorption rate (SAR$_{wb}$) in realistic environments.

There is a lack of information in the literature regarding the human's ACS$_{wb,dmc}$. We determine first in this chapter the ACS$_{wb,dmc}$ of a canonical phantom - through measurements in an RC - from the reverberation time values obtained using *i)* a customized method denoted as the *slope* method, and *ii)* the maximum-likelihood high-resolution algorithm RiMAX. Secondly, the experimental ACS$_{wb,dmc}$ value of a the phantom is compared with the numerical result as a validation.

The use of a numerical algorithm such as RiMAX [17] is expected to provide additional robustness and possibilities since it removes the unstirred energy from the measurements and allows the determination of the ACS$_{wb}$ of a single person, allowing thereby the investigation of different postures of the human under test in the RC.

To my knowledge, this is the first time where the whole-body absorption cross section - induced by diffuse fields - is clearly defined and determined.

This chapter is organized as follows. The definition of the ACS$_{mean}$ and ACS$_{wb,dmc}$ in diffuse fields and the differences between these quantities are addressed in Section 2.2. The materials, the test environment and the methodology to determine both the reverberation time and the absorption cross section in diffuse fields are introduced in Section 2.3. The numerical settings of the simulation platform and the diffuse fields' properties in the simulation is also given. Section 2.4 presents the measured and simulated results. Realistic values of the ACS$_{wb,dmc}$ of a human in diffuse fields are determined from RC measurements are determined as well. Finally, conclusions are drawn in Section 2.5.

2.2 Difference between the ACS$_{mean}$ and ACS$_{wb,dmc}$

Basically, the ACS of a lossy object is defined as the ratio of the power absorbed by the object to the incident power density. However, it is important to distinguish the ACS in diffuse fields (ACS$_{wb,dmc}$) from the mean or average ACS (ACS$_{mean}$) from single plane-wave illumination. Let's define a plane wave p by its azimuth φ_p, elevation θ_p, and polarization ψ_p.

On one hand, the ACS$_{mean}$ is found by averaging the different values of the ACS obtained from a *single* incident plane wave [7, 13]. The different values of the ACS are obtained for different directions and polarizations of the plane wave p. The ACS$_{mean}$ can be formulated as follows:

$$ACS_{mean} = \frac{1}{P} \sum_{p=1}^{P} ACS_p(\varphi_p, \theta_p, \psi_p) \qquad (2.1)$$

where ACS_p is the absorption cross section for an incident plane wave p and P is the total number of plane waves. The direction and the polarization of the plane wave p are varied to obtain statistical relevant value accounting for all possible directions and polarization.

The experimental methodology consists in measuring the averaged power levels in steady state - through Hill's formula [2] - of the chamber when it is unloaded and loaded. The ACS_{mean} of a human (mass $\approx$ 75 kg and height $\approx$ 181 cm) determined in an RC from 1 to 18 GHz in a sitting posture is reported in [16].

On the other hand, the $ACS_{wb,dmc}$ is found by calculating the ACS for several plane waves *simultaneously* incident to the object under test. The $ACS_{wb,dmc}$ is obtained for the summed or integrated power. The $ACS_{wb,dmc}$ can be formulated as follows:

$$ACS_{wb,dmc} = \frac{1}{S} \sum_{s=1}^{S} ACS_s(\Phi_s, \Theta_s, \Psi_s), \tag{2.2}$$

with $\Phi_s=[\varphi_1^s, \ldots, \varphi_N^s]$, $\Theta_s=[\theta_1^s, \ldots, \theta_N^s]$, and $\Psi_s=[\psi_1^s, \ldots, \psi_N^s]$. The N plane waves are simultaneously incident and are spatially distributed to surround the object under test and S is the number of samples. The polarization and phase of the multiple incident plane waves are both assumed to be random and are defined in Section 2.3.4. To show a clear difference between the two quantities, we will consider a uniform sphere and determine its ACS_{mean} and $ACS_{wb,dmc}$ in Section 2.4.1 and Section 2.4.2, respectively. The modeling of the exposure for the determination of the ACS_{mean} and $ACS_{wb,dmc}$ is shown in Fig. 2.2.

(a)   (b)
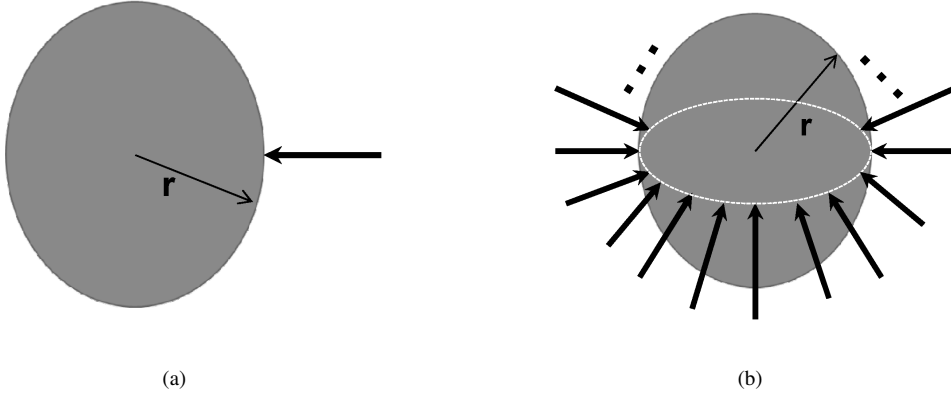
Figure 2.2: Configuration for calculating the ACS_p, i.e., 2.2(a) and the ACS_s, i.e., 2.2(b). The arrows represent the incident plane wave(s)

The radius of the sphere is set to 19.25 cm as in [16] for comparison purposes.

2.3 Materials and methodology

2.3.1 Reverberation chamber, materials and measurement setup

For our measurements, we use the RC of the TELICE group, University of Lille, France. The dimensions of this RC are 2.80 m $\times$ 5.70 m $\times$ 4.10 m (Height $\times$ Length $\times$ Width), resulting in a volume of 65 m^3. A metallic sheet is mounted onto a vertical pole going from the ceiling to the floor and consists of 4 vertical

elements [8].

This study has been carried out at 1800 MHz (telecommunication frequency and LTE frequency in Belgium, Italy, Germany, United Kingdom, etc.) within a bandwidth of 100 MHz divided into 101 frequency points. As transceivers, two double ridge guide horn antennas of type SAS-571 were placed and oriented suitably in the RC in order to achieve a Rayleigh channel [5]. This is achieved by orienting the transceivers toward walls, creating thereby a NLOS view. It is important for us to achieve a Rayleigh channel to minimize the influence of the direct path (unstirred energy) in the measured data.

Three orientations of the transceivers are considered. For the vertical orientation, the Tx and the Rx feeder are both oriented along the z-axis direction (referring to the coordinates system of Fig. 2.1); for the horizontal orientation, the Tx and the Rx feeder are both oriented along the y-axis direction; and finally for the cross orientation, the Tx feeder (resp. the Rx feeder) is oriented along the y-axis (resp. z-axis) direction. The stirrer rotates 180 times during one measurement with a step of $2°$. For each of its positions, the impulse transfer function of the propagation channel is measured; the PDP being calculated from it.

The experiments have been conducted with four identical polyvinyl chloride (PVC) cylindrical phantoms positioned arbitrarily in the working area of the RC and filled with liquid. The phantom has an inner radius of 119.50 mm, an outer radius of 124.50 mm (thickness = 5 mm) and a height of 1500 mm. A picture of the phantoms and the transceivers located in the RC is shown in Fig. 2.3.

Figure 2.3: Phantoms and transceivers in the reverberation chamber. The RC dimensions are 2.80 m $\times$ 5.70 m $\times$ 4.10 m (Height $\times$ Length $\times$ Width)

Dosimetric measurements are usually performed with liquids having dielectric properties similar to those of biological tissues. Hence, a tissue-simulating liquid that has similar dielectric properties as the body tis-

sue parameters specified in [18] is used. The liquid was composed of water, salt, and sugar. Different mixtures have been measured so that we obtained a liquid with the targeted dielectric properties. The final liquid had a relative complex permittivity ϵ_r = 57.74+13.55j, conductivity σ = 1.47 S/m, and a mass density ρ = 1000 kg/m^3. This liquid was used in the experiments and its properties were included into all the simulations as well. The dielectric properties of the liquid were measured using a Hewlett Packard HP85070A (Agilent) dielectric probe kit connected to a Hewlett Packard (Agilent) network analyzer [19]. All the measurements in the RC were conducted the same day in order to avoid excessive evaporation of the liquid. In addition, we ensured that the dielectric properties variations were within $\pm 5\%$, as recommended in [20].

2.3.2 Methodology for the reverberation time assessment

Power delay profile

The averaged PDP in the RC is obtained after taking the squared modulus of the inverse Fourier transformation of the transfer functions. The averaged PDP in decibels, labeled as APDP is thus given by:

$$APDP(t) = 10log10(\left|S_{21}^{avg}(t)\right|^2) \tag{2.3}$$

where S_{21}^{avg}(t) is the averaged scattering parameter.
An example of the APDP in the RC is shown in Fig. 2.4. We observe a quasi-perfect linear decay (in logarithm scale) of the relative power level as a function of the delay.
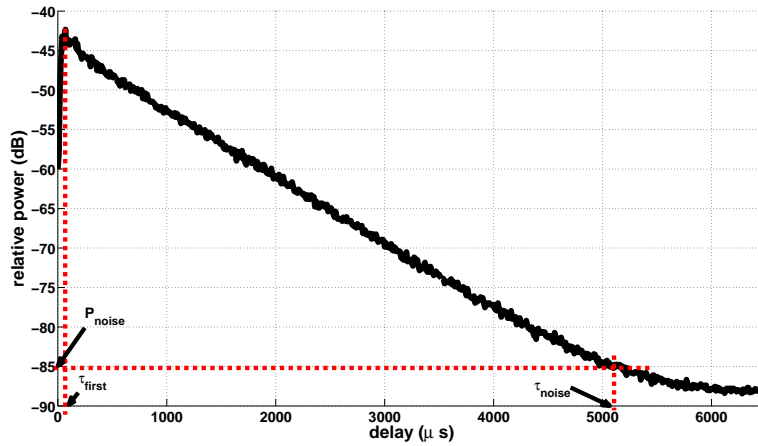
Figure 2.4: Power delay profile in the RC at 1.8 GHz. P$_{noise}$, τ_{first}, and τ_{noise} are the noise level, arrival delay of the first component, and arrival delay corresponding to the noise level, respectively

Extraction of the reverberation time

If the exponential decaying PDP is translated into the logarithmic scale, a linear tail with a negative slope is observed in the decay process as can be seen in Fig. 2.4. The reverberation time is related to the slope of

the decaying tail, and is expressed as follows:

$$\tau = -\frac{10log10(e)}{slope} \tag{2.4}$$

where τ is the reverberation time, $e \approx 2.718$ is *Euler*'s number and *slope* is the slope of the linear tail observed in the impulse response (in dB).

In practice, the experimental APDP (see Fig. 2.4) does not have a perfect linear tail because of the applied inverse Fourier transform, the noise level of the network analyzer, the measurement uncertainties, etc. Therefore, we need to derive the reverberation time over a certain delay range (or a certain range of power) in such a way that the APDP's tail could be approximated by a straight line. The choice of this delay range should be done automatically because manual detection would suffer from judgment subjectivity. Once the delay range is known, the slope of the linear tail is obtained by applying a linear regression fit. The general methodology is shown in the flow graph of Fig. 2.5.
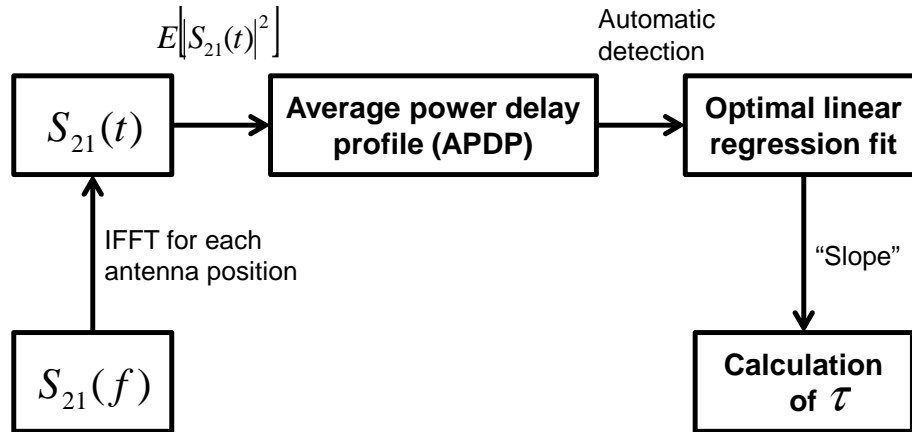
Figure 2.5: Flow chart of the methodology to determine the reverberation time from measurements

One may automatically determine the reverberation time by using a fixed delay range. Such approach would be good for a given room and propagation conditions. However, when changing the room (volume), the Tx-Rx separation, or when the propagation conditions change, the level of the received power will be different. As a consequence, the APDP's tail varies and neither the previous delay range, nor the power range will be valid anymore. Our objective here is to develop a site-independent procedure for the determination of the reverberation time. Therefore, we introduce a procedure to automatically determine the delay range where the APDP's tail can be approximated with a straight line. Let us consider the APDP of Fig. 2.4 and we define the following parameters.

- τ_{first} is the arrival delay of the first component.
- P_{min} is the lowest APDP value
- P_{noise} is the noise floor

31

– τ_{noise} is the delay corresponding to P_{noise}.

We arbitrarily define the noise floor as follows.

$$P_{noise} = P_{min} + 3 \; dB \tag{2.5}$$

where 3 dB is added to ensure that the estimated noise level will be above the actual noise level.

The slope of the APDP's tail is then determined by applying a linear regression fit between τ_{first} and τ_{noise}. Once the slope is obtained, one can easily determine the reverberation time be applying (2.4).

2.3.3 Procedure for the assessment the absorption cross section in diffuse fields

We define here the human's absorption cross section in diffuse fields and derive an experimental methodology for its assessment. When electromagnetic fields propagate in a room, rays impinge on the walls, objects present in the room, ceiling, floor, and present phantoms (or human beings). The dielectric properties of the free space is different from those of the materials in interaction with the waves. As a consequence, a fraction of the electromagnetic energy is absorbed by these materials. The absorbed power depends mainly on the considered frequency, the dielectric properties of the walls, and the surface area illuminated by the electromagnetic radiation. The surface illuminated by the radiation is denoted as the absorption area. If we consider that all objects in the chamber are fixed except the number of phantoms (or persons), the absorption area in diffuse fields varies as follows:

$$A_n = A_0 + \sum_{i=1}^{n} BSA(i) \tag{2.6}$$

where A_n, A_0, n, $BSA(i)$ are respectively the total surface area, total surface of the fixed structures (ceiling, walls, floor, furniture, etc.), number of persons, and the body surface area of the ith person. We assume that all the persons (or phantoms) present in the room have the same or similar body surface area.

The effective absorbing area (or absorption cross section) is the surface area times the average fraction of absorbed energy. Assuming that the phantoms have equal body surface area, the following expression of the total effective absorbing area is obtained:

$$A'_n = A'_0 + n \times ACS_{wb,dmc} \tag{2.7}$$
$$= \eta A_n$$

where $ACS_{wb,dmc}$ is the phantom's (or human's) absorption cross section in diffuse fields, i.e, the percentage of human body surface absorbing electromagnetic radiation in diffuse fields and η is the average fraction of absorbed energy (see Section 1.3.1). n is the number of phantom(s) and A'_n the total effective area defined in (2.8). The methodology to experimentally assess the $ACS_{wb,dmc}$ is based on the room electromagnetics theory, which states that all losses in a closed environment can be described with its reverberation time. It is possible to determine the effective absorption area of the chamber from its reverberation time [21].

$$A'_n = \frac{4V}{c_0 \tau_n} \tag{2.8}$$

where A'_n, V, c_0=3×10^8m/s, and τ_n are respectively the total effective absorbing area (m^2) of the room, the room volume (m^3), the light velocity in free space, and the reverberation time (s) when n phantom(s) are present in the room. The theoretical analysis of the reverberation time when the room is occupied with persons and its relation with the absorbing areas (i.e., fixed surfaces, humans' body surface area) are addressed in Section 1.3.1 of Chapter 1.

By varying the RC occupation successively with a different number of phantom (or people), the room effective absorbing area as a function of the number of people (n=0, 1, 2, 3, etc.) is obtained from the corresponding reverberation time values. Furthermore, the person's (or phantom) absorption cross section in diffuse fields is the slope (assuming they have the same ACS$_{wb,dmc}$) of the linear regression of the points related to the different absorbing areas for the different number of people.

2.3.4   Numerical simulation settings and diffuse fields' properties

The Finite-Difference Time-Domain (FDTD) solver SEMCAD-X is used to compute numerically the whole-body absorption cross section of the phantom in diffuse fields. SEMCAD-X is a 3D full-wave electromagnetic and thermal simulation platform [22]. The ACS$_{wb,dmc}$ is determined from the SAR$_{wb}$ value obtained when the phantom is illuminated simultaneously by several plane waves incident in all directions. The dielectric properties of the liquid described in Section 2.3.1 were used for the simulation settings.

Plane-wave sources based on the Total-Field Scattered-Field (TFSF) technique [23] are used to excite the cylindrical phantom. The plane waves superposition principle [3] is applied to simulate in SEMCAD-X the multiple paths encountered in RCs, similarly to [24, 25]. The multiple waves resulting from movement of the stirrer is called here a set of waves. S sets are used to excite the cylinder since the stirrer occupied several positions during the measurements. The S sets allow us the derivation of the statistical properties of the ACS$_{wb,dmc}$ since one ACS$_{wb,dmc}$ value is obtained per set.

Let us now define the properties of the plane waves within a set. A set is comprised of N plane waves, i.e., N_a plane waves in the azimuthal domain and N_e elevation angles are considered per azimuth (N=N_a×N_e). The plane waves are uniformly distributed in both azimuthal and elevation domain because we simulate diffuse fields. The total power density is divided by the number of plane waves in a set so that the plane waves have the same amplitude. The polarization of the diffuse fields in RCs can be obtained from the analysis of the polarization angle. The polarization angle can be obtained from the amplitude ratio between the co-polarized and cross-polarized received E-field and is expressed as follows:

$$\psi = \arctan\left(\frac{A_{pp}}{A_{qp}}\right) \tag{2.9}$$

where *p* and *q* can be either horizontal or vertical. A$_{pp}$ (resp. A$_{pq}$) is the magnitude of the E-field received by co-polarized (resp. cross-polarized) antennas. The result of the measurement of the polarization angle in the RC of Fig. 2.3 is shown in Fig. 2.6. Note that the radiation pattern of the horn antennas is included in the received powers.
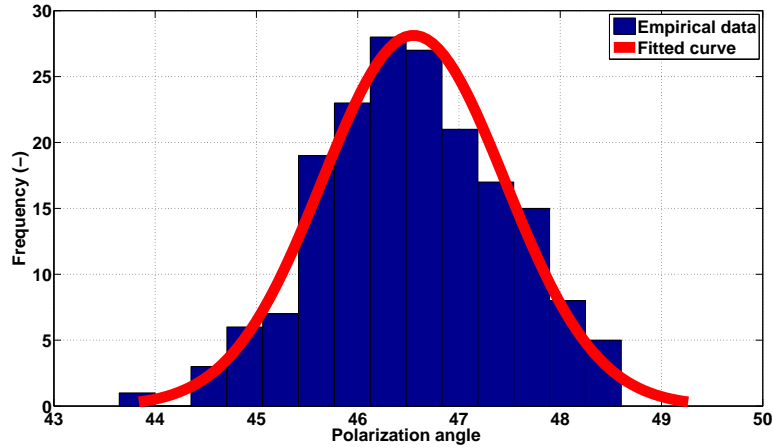
Figure 2.6: Distribution of the polarization angle in the reverberation chamber (mean value $\mu = 46°$ and standard deviation $\sigma = 0.90°$)
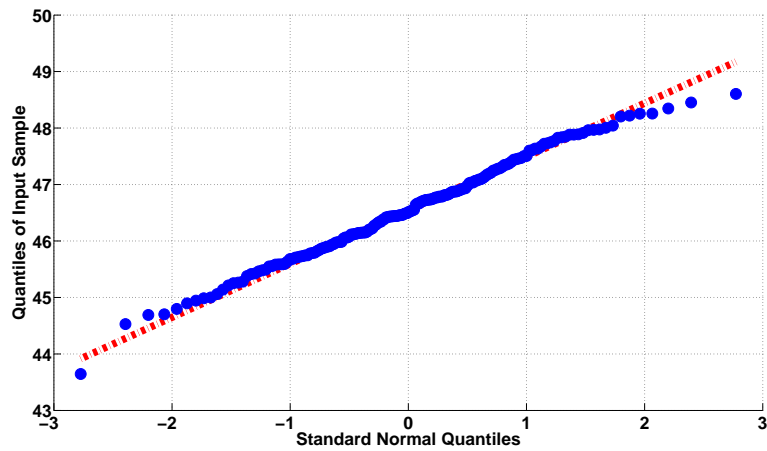
Figure 2.7: Q-Q plot of the samples versus standard normal

The mean value of the polarization angles in the RC is slightly larger than $45°$. This is in agreement with the analysis of the cross-polar ratio (XPR) in indoor environments [26, 27] where it is reported that the mean value of the XPRs is of the order of ≈ 0 dB. The mean value of the polarization angle of $\approx 45°$ shows that about half of the total received power is received by a vertically-polarized antenna while the other half is received by a horizontally-polarized antenna.

Moreover, the curve fitted to the frequency of the polarization angles (red curve in Fig. 2.6) and the quantile-

quantile plot of Fig. 2.7 clearly show that the polarization angle is normally distributed. The diffuse fields stem from multiple scatterings and diffractions that occur at the walls and other objects surrounding the receiver (or phantom). The polarization of an EMF is randomly shifted after each scattering, or diffraction. Therefore, the normal distribution of the polarization of the diffuse field is well justified by applying the central limit theorem as the total received signal in diffuse fields at a given point in the environment is the sum of a large number of scattered and diffracted waves from the walls and/or surrounding objects. It has been shown that the number of reflections or scattering components increases rapidly as a function of the number of walls and reflections order [28]. The normal distribution of the diffuse field is also in agreement with literature, e.g., [29, 30] where the authors investigated the polarization of multipath components in realistic indoor environments. Here, we obtain a standard deviation of less than $1°$. Therefore, we set the polarization angle of each plane wave in diffuse fields to $45°$. This modeling agrees well with the polarization factor of 0.5 chosen in the room electromagnetics theory [31]. Other approaches would also be possible, e.g., a uniform distribution of the polarization angle is used for the uplink bands, DECT, and WiFi bands [32], but we propose here the normal distribution with mean value of $45°$ for the reasons mentioned above.

Regarding the plane waves' phase, the notion of *starting point* is used [25]. The starting point is related to the phase as it defines the traveled path of the plane wave. Here, the starting point of each plane wave is randomly chosen with equal probability in the range $]0, \lambda/2]$, where λ is the wavelength at the considered frequency. This corresponds to the phase interval $]0, \pi]$. This is the correlation interval [33] ensuring that the E-field values of a plane wave traveling from the starting point to the simulation domain will not be uncorrelated. The choice of $]0, \pi]$ can be thought of as a mean of avoiding destructive interference of the waves in a set, which will not favor the establishment of diffuse fields. This is in agreement with [28] where it is stated that the interference can be neglected when dealing with the diffuse field's energy density at relatively high frequencies. Moreover, the uniformity of the diffuse field in space is a key condition for the existence of diffuse energy. A quantity to measure the field's uniformity is the correlation coefficient of the E-fields of the plane-waves [28], which is expressed as follows (assuming the same amplitude for each plane-wave):

$$\Psi(x) = \frac{\sin(kx)}{kx} \tag{2.10}$$

where $k = \frac{2\pi}{\lambda}$ and x is the path length difference between two plane-waves. There are perfect or complete diffuse fields (resp. no diffuse fields) if $\Psi = 1$ (resp. $\Psi = 0$) [28]. From (2.10) we see that $0 \leq \Psi(x) \leq 1$ for $0 \leq x \leq \frac{\lambda}{2}$, which corresponds to our choice of $]0, \pi]$ for the distribution of the phase in diffuse fields.

Simulation of the RC in SEMCAD-X would have required excessive memory resources and time because the FDTD method would have to discretize spatially the entire chamber. Therefore, the object under test is located inside a simulation domain which has comparable sizes with the object under test. To avoid the reflections of the waves impinging on the simulation domain boundaries, uniaxial perfectly match layer (UPML) is used as absorbing boundaries conditions in such as way that more than 95% of the incident wave power is absorbed by the boundary layers. The $ACS_{wb,dmc}$ of the object under test is derived from the

simulated SAR_{wb} as follows:

$$ACS_{wb} = \frac{SAR_{wb} \times m}{I}, \qquad (2.11)$$

where SAR_{wb}, m, and I are the whole-body specific absorption rate of the object under test (in diffuse fields), the object's mass, and the total power density, respectively. It is important to mention that the diffuse fields are simultaneously incident to the phantom from all directions.

Because of the randomness introduced by the phase and the polarization, the $ACS_{wb,dmc}$ is addressed with a stochastic approach. The statistical multipath tool [34] - which is based on FDTD simulations - is used to determine the numerical value of the $ACS_{wb,dmc}$. Regarding the numerical simulation of the cylinder in SEMCAD-X, we set the parameters N_a and N_e defined above as follows: N_a = 72 and N_e = 6. Each polarization angle in the tool is decomposed into two orthogonal polarizations, leading to a total SEMCAD-X simulations of 864 (72×6×2). An illustration of the cylinder in diffuse fields is shown in Fig. 2.8.
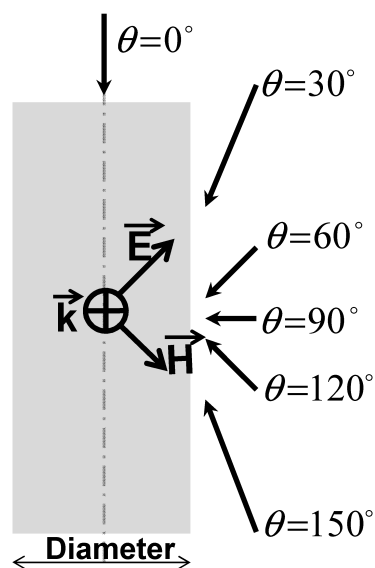
Figure 2.8: Cylinder and the diffuse fields illustration (for a given azimuth). 6 elevation angles are considered per azimuth and 72 azimuthal angle are considered. $\vec{\mathbf{E}}$, $\vec{\mathbf{H}}$, and $\vec{\mathbf{k}}$ are the electric field vector, magnetic field vector, and wave vector, respectively

For the exposure samples, 1000 sets of plane waves were used to obtain statistically relevant values. Each set contains 432 plane waves ($N_a \times N_e$). The statistical multipath tool [34] has the advantage to reduce considerably the simulations time and to facilitate the management of the simulation output. The outcome of the tool is the cumulative distribution function (cdf) of the SAR_{wb} from which the $ACS_{wb,dmc}$ is determined using (2.11).

2.4 Experimental and numerical results

2.4.1 ACS$_{mean}$ of a uniform sphere (single plane-wave illumination)

Fig. 2.2(a) shows the configuration of the sphere and an incident plane wave. The same dielectric properties as listed in Section 2.3.1 are used here since the same frequency of 1800 MHz is considered. The ACS$_{mean}$ of a sphere is the same as the ACS for any incoming single plane wave [13]. No averaging over the directions nor the polarizations is needed due to the symmetry of the sphere in all directions [7]. The ACS$_{mean}$ of a sphere is analytically determined from the coefficients of the Mie theory [35] and is given by [35, page 103].

$$ACS_{mean} = ACS_{ext} - ACS_{sca} \tag{2.12}$$

where ACS$_{ext}$ and ACS$_{sca}$ are the extinction and scattering ACS, respectively, and defined as follows [35]:

$$ACS_{ext} = \frac{2\pi}{k^2} \sum_{n=1}^{\infty} (2n+1)[Re(a_n + b_n)], \tag{2.13}$$

$$ACS_{sca} = \frac{2\pi}{k^2} \sum_{n=1}^{\infty} (2n+1)[|a_n|^2 + |b_n|^2], \tag{2.14}$$

where $k = \frac{2\pi}{\lambda}$ is the wavenumber, $Re(X)$ denotes the real part of the complex number X, and a_n and b_n represent the magnetic and electric multi poles of order n, respectively. Their expressions can be found in [35, page 100].
Applying (2.14), (2.13), and (2.12), an ACS$_{mean}$ of 0.0695 m^2 is obtained. A similar value of the ACS$_{mean}$ calculated with the equations of the Mie theory is obtained in [16]. We obtain from FDTD simulations that ACS$_{mean}$ (sphere illuminated with a single plane wave) is equal to 0.0684 m^2, resulting in a relative error of less than 2%. When determining the absorbed power in a given phantom under test in SEMCAD-X, the phantom is decretized and results in a multitude of voxels. The number of voxels depends on the phantom's dimensions and the considered grid size. Then, the FDTD method determines first the power in each voxel and eventually sum them to calculate the total power absorbed by the phantom. Therefore, the methodology to determine the absorbed power in a phantom is independent of its shape. This remark and the excellent agreement between the simulation and the analytical result show us that the simulation is a suitable alternative to determine accurately the ACS of objects with irregular shapes.

2.4.2 ACS$_{wb,dmc}$ of a uniform sphere (diffuse illumination)

The ACS$_{wb,dmc}$ - in diffuse fields - of the same sphere is now numerically determined. Fig. 2.2(b) shows the modeling of the diffuse fields in the simulation tool. Here, 200 sets are used for the simulation of the sphere and a set is comprised of 100 plane waves surrounding the sphere. Applying (2.11) to the 200 SAR$_{wb}$ values obtained from the simulation and considering the sphere's mass of about 30 kg, an averaged ACS$_{wb,dmc}$ of about 0.22 m^2 is obtained. The difference between the ACS$_{mean}$ and the averaged ACS$_{wb,dmc}$ is about 4.90 dB for the uniform sphere.

2.4.3 Experimental results of the cylinder's absorption cross section in diffuse fields from measurements in the RC

For the experiments, the RC was loaded with 0, 1, 2, 3, or 4 phantom(s) filled with the tissue equivalent liquid, and 180 channel transfer functions were measured for each scenario. The PDPs for the different load of the RC are shown in Fig. 2.9.
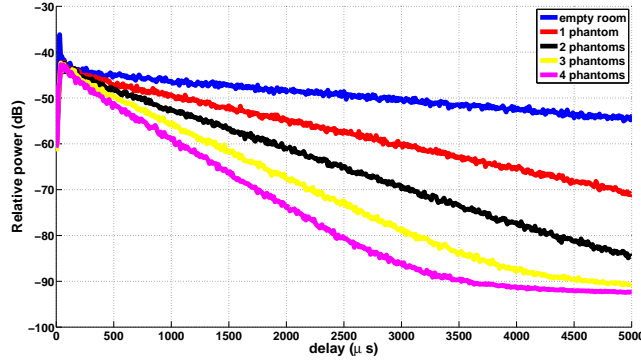
Figure 2.9: PDP in the reverberation chamber loaded with a different number of phantom(s) (Vertical-Vertical polarization)

The more phantoms in the RC (i.e., the more the RC is loaded), the steeper the PDP's slope is, indicating the faster decay of the diffuse field's energy. Physically, the EMF strength decays faster because the area absorbing the EM radiation increases due to the additional cylinder(s). For each PDP, the reverberation time is determined using the RiMAX estimator and the *slope* method described in Section 2.3.2. The RiMAX estimator is tuned to remove the strongest specular component from the measured PDP. The resulting reverberation time values are listed in Table 2.1, where τ_i designates the RC's reverberation time value when it is loaded with i phantom(s), $i \in 0, 1, ..., 4$. We observe that the reverberation time depends slightly on

Tx-Rx orientation	method	τ_0 (ns)	τ_1 (ns)	τ_2 (ns)	τ_3 (ns)	τ_4 (ns)	$ACS_{wb,dmc}$ (m²)	Δ ACS (%)
vertical (V-V)	RiMAX	2085	820	515	373	291	0.63	1.6
	Slope	1995	785	497	361	285	0.64	
cross (V-H)	RiMAX	2112	831	523	377	301	0.63	1.6
	Slope	2120	826	528	381	298	0.62	
horizontal (H-H)	RiMAX	2067	821	511	370	289	0.63	1.6
	Slope	1972	804	488	358	279	0.64	

Table 2.1: Benchmarking of the reverberation times, RiMAX vs Slope method

the transceiver's orientation, but these differences are insignificant and might be due to the measurement uncertainties. The reverberation time values for the cross polarization setup are the largest - regardless of

their determination procedure - demonstrating that the DMC is particularly strong for that configuration. In general, the *slope* method underestimates the reverberation time value in comparison with the RiMAX algorithm. This is explained by the possible presence of specular components not subtracted from the PDP when the *slope* method is used to determine the reverberation time.

From the reverberation time values, the experimental $ACS_{wb,dmc}$ of the cylinder is determined by linear regression method described in Section 2.3.3.

The experimental $ACS_{wb,dmc}$ values are listed in the last column of Table 2.1. The $ACS_{wb,dmc}$ values obtained for the different orientations of the transceiver and the different method are very similar. The maximum relative difference (Δ ACS) between the two methods (for all the transceiver's orientations) is about 1.6%. The results show that the $ACS_{wb,dmc}$ values are independent of the transceiver's orientation, indicating that the $ACS_{wb,dmc}$ is induced by stirred (or diffuse) fields. Moreover, the small relative deviation between the experimental $ACS_{wb,dmc}$ values also shows that the absorption cross section in diffuse fields is independent of the method used to determine the reverberation time values. Therefore, we will use the *slope* method to determine experimentally the $ACS_{wb,dmc}$ (unless otherwise stated) in the following as this method is simpler, faster, easy to implement, and requires less memory resources.

2.4.4 Numerical results of the cylinder's absorption cross section in diffuse fields from SEMCAD-X

The settings of the numerical simulation of the cylinder is described in Section 2.3.4. The outcome of the statistical multipath tool is the cumulative distribution function (cdf) of the $SAR_{wb,dmc}$ of the cylinder under diffuse exposure and is shown in Fig. 2.10. Given the cylinder's mass of about 65 kg and knowing the incident power density, we apply (2.11) to the $SAR_{wb,dmc}$ values of Fig. 2.10. As result, the cdf of the cylinder's $ACS_{wb,dmc}$ is obtained and is shown in Fig. 2.11.
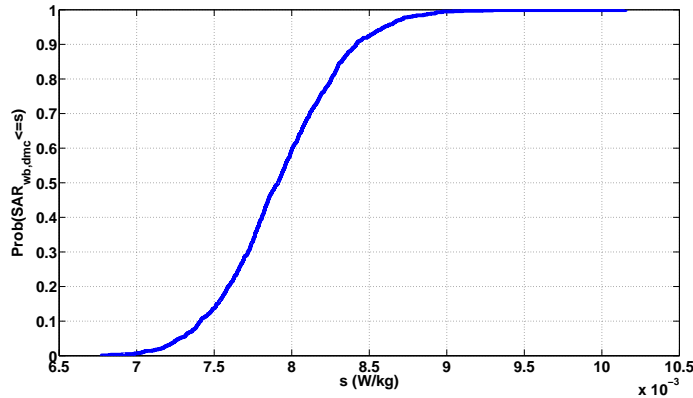
Figure 2.10: Cumulative distribution of the whole-body specific absorption rate of the cylinder in diffuse fields. $\ll$s$\gg$ designates the values of the $SAR_{wb,dmc}$ on the x-axis

From the cdf, an average value of the numerical $ACS_{wb,dmc}$ of about 0.52 m^2 is obtained.
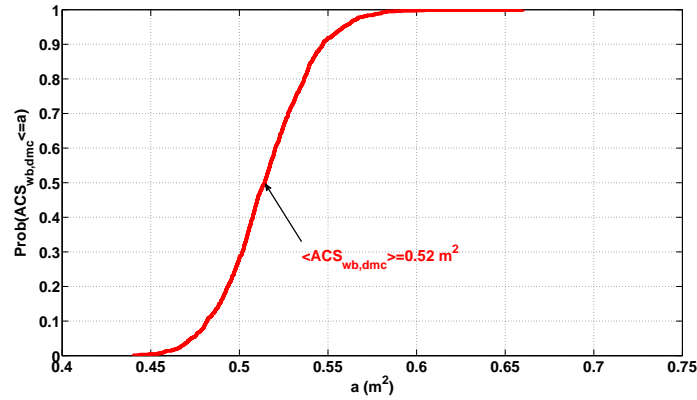
Figure 2.11: Cumulative distribution function of the whole-body absorption cross section of the cylinder in diffuse fields. ≪a≫ designates the values of the $ACS_{wb,dmc}$ on the x-axis.

We found a numerical (resp. experimental) value of the average whole-body absorption cross section in diffuse fields of about 0.52 m^2 (resp. 0.63 m^2), leading to a relative error of 17%. This indicates a good agreement between the experimental and numerical approaches. The difference between the two approaches is attributed to *i)* the modeling of the multiple incident fields since we consider only few incident angles, *ii)* the statistical properties of the plane waves during the simulations might be slightly different from what actually occurs in the RC and *iii)* other uncertainties during both measurements and simulations.

2.4.5   Application to a real human

In this section, the $ACS_{wb,dmc}$ in diffuse fields of a real human located in the RC is determined at 1800 MHz. The person (height = 1.73 m and mass = 63 kg) was located in the RC during the measurements. Three postures were considered: sitting, standing, and standing with stretched arms. The human under test in the standing with stretched arms' posture is shown in Fig. 2.12.
The $ACS_{wb,dmc}$ is determined for the cross orientation of the transceivers. Two measurements have been carried out: one PDP measured in the empty RC and a second one measured with the human adopting one of the mentioned postures. The reverberation time values are determined with the RiMAX algorithm and are used to assess the human's $ACS_{wb,dmc}$. As shown in Table 2.2, a human's $ACS_{wb,dmc}$ of about 0.95 m^2, 1.01 m^2, and 1.11 m^2 was obtained for the sitting, standing, and standing with stretched arms postures, respectively. The body surface area (BSA) of humans is only dependent of their height and mass [36–39]. However, the human's $ACS_{wb,dmc}$ for a given incident field depends not only of the BSA but also of the posture of the person. This is justified because the body surface (of humans) illuminated by the EMFs varies with the posture. The highest $ACS_{wb,dmc}$ occurs for the standing with stretched arms' posture whilst the lowest occurs for the sitting posture. The obtained values are logically proportional to the effective surface of the human under test in the three postures. The obtained $ACS_{wb,dmc}$ values change with frequency

Figure 2.12: Human under test in the RC adopting the standing with stretched arms' posture

Posture			
$\text{ACS}_{wb,dmc}$	0.95 m^2	1.01 m^2	1.11 m^2

Table 2.2: Human whole-body $\text{ACS}_{wb,dmc}$ for different postures

(Chapter 5).

The ACS is independent of the reverberating environment wherein it is determined [14]. Therefore, the values obtained from RC measurements can be used to determine the $\text{SAR}_{wb,dmc}$ due to diffuse fields in realistic reverberating environments.

2.5 Conclusions

The knowledge of the $\text{ACS}_{wb,dmc}$ is critical for the assessment of the $\text{SAR}_{wb,dmc}$ of humans in realistic environments where the diffuse field is dominant. Previous works in literature addressed the ACS due to single plane-wave exposure. Recent studies in the wireless propagation's community have evidenced the existence of diffuse fields in realistic indoor environments. However, the ACS values due to diffuse fields' exposure and related properties were missing in the literature. We show in this chapter the difference between the average or mean ACS_{wb} induced by deterministic plane wave(s) and the average $\text{ACS}_{wb,dmc}$ due to diffuse fields. An original experimental approach is developed to determine the $\text{ACS}_{wb,dmc}$ in diffuse fields with good accuracy from measured transfer functions in a stirred-mode reverberation chamber. To demon-

strate the effectiveness and robustness of the proposed method, the $\text{ACS}_{wb,dmc}$ of a cylindrical phantom was experimentally determined at 1.8 GHz in a reverberation chamber using the high-resolution parameter estimator RiMAX and an empirical method denoted as *slope* method. Both methods yield the same results in terms of $\text{ACS}_{wb,dmc}$. Furthermore, we developed a statistical approach to model the diffuse fields in the numerical simulation tool. The experimental $\text{ACS}_{wb,dmc}$ of a cylindrical phantom obtained in diffuse fields has been validated through numerical simulations. A good agreement is obtained between experimental and numerical approaches with a relative error of about 17%. Following the validation of the experimental procedure, the $\text{ACS}_{wb,dmc}$ of a human in diffuse fields was determined for three different postures in a RC. We clearly demonstrate the potential use of reverberation chambers to assess human's exposure in real environments. The next chapters will be an application of this chapter, i.e., we determine the reverberation time values and the human's exposure in realistic indoor environments.

References

[1] P. Corona, G. Latmiral, E. Paolini, and L. Piccioli. "Use of a Reverberating Enclosure for Measurements of Radiated Power in the Microwave Range". *IEEE Trans. Electromagn. Compat.*, 18 (2): pages 54–59, 1976.

[2] D. A. Hill, M. T. Ma, and A. R. Ondrejka. "Aperture Excitation of Electrically Large, Lossy Cavities". *IEEE Trans. on Electromagn. Compat.*, 36 (3): pages 169–178, 1994.

[3] D. A. Hill. "Plane Wave Integral Representation for Fields in Reverberation Chambers". *IEEE Trans. Electromagn. Compat.*, 40 (3): pages 209–217, 1998.

[4] P. Corona, G. Ferrara, and M. Migliaccio. "Reverberating Chamber Electromagnetic Field in Presence of an Unstirred Component". *IEEE Trans. Electromagn. Compat.*, 42 (2): pages 111–115, 2000.

[5] C. L. Holloway, D. A. Hill, J. M. Ladbury, P. F. Wilson, G. Koepke, and J. Coder. "On the Use of Reverberation Chambers to Simulate a Rician Radio Environment for the Testing of Wireless Devices". *IEEE Trans. Antennas Propag.*, 54 (11): pages 3167–3177, 2006.

[6] P. S. Kildal, C. Orlenius, and J. Carlsson. "OTA Testing in Multipath of Antennas and Wireless Devices With MIMO and OFDM". *Proceedings of the IEEE*, 100 (7): pages 2145–2157, 2012.

[7] C. L. Holloway, D. A. Hill, J. M. Ladbury and G.n Koepke. "Requirements for an Effective Reverberation Chamber: Unloaded or Load". *IEEE Trans. Electromagn. Compat.*, 48 (1): pages 187–194, 2006.

[8] O. Delangre. *"Caracterisation et Modelisation du Canal Radio en Chambre Reverberante"*. PhD thesis, Universite Libre de Bruxelles (Departement OPERA) & Universite Lille 1 (Laboratoire IEMN-TELICE), 2009.

[9] M. A. Garcia-Fernandez, J. D. Sanchez-Heredia, A. M. Martinez-Gonzalez, D. A. Sanchez-Hernandez, and J. F. Valenzuela-Valdes. "Advances in Mode-Stirred Reverberation Chambers for Wireless Communication Performance Evaluation". *IEEE Communications Magazine*, 49 (7): pages 140–147, 2011.

[10] P. Besnier and B. Demoulin. *"Electromagnetic Reverberation Chambers"*. ISTE Ltd and John Wiley & Sons, Inc., 2011.

[11] M. Liénard and P. Degauque. "Simulation of dual array multipath channels using mode-stirred reverberation chambers". *Electronics Letters*, 40(10): pages 578–580, 2004.

[12] Per-Simon Kildal. Correlation and Capacity of MIMO systems and Mutual Coupling, Radiation Efficiency, and Diversity Gain of Their Antennas: Simulations and Measurements in a Reverberation chamber. *IEEE Communications Magazine*, 42 (12): pages 104–112, 2004.

[13] U. Carlberg, P. S. Kildal, A. Wolfgang, O. Sotoudeh and C. Orlenius. "Calculated and Measured Absorption Cross Sections of Lossy Objects in Reverberation Chamber". *IEEE Trans. Electromagn. Compat.*, 46(2): pages 146–154, 2004.

[14] T. Nguyen. "RF Loading Effects of Aircraft Seats in an Electromagnetic Reverberating Environment". In *18th Digital Avionics Systems Conference, Procedings, vol. 2, pages 10.B.5-1 - 10.B.5-7*, 1999.

[15] E. Amador, M. I. Andries, C. Lemoine and P. Besnier. "Absorbing Material Characterization in a Reverberation Chamber". In *10th International Symposium on Electromagnetic Compatibility (EMC Europe), pages 177-122*, 2011.

[16] G. C. R Melia, I. D. Flintoft and M. P. Robinson. "Absorption Cross-Section of the Human Body in a Reverberant Environment". In *International Symposium on Electromagnetic Compatibility (EMC EUROPE)*, 2012.

[17] A. Richter. *"Estimation of Radio Channel Parameters: Models and Algorithms"*. PhD thesis, Faculty of electrical Engineering and Information Technology at the Technical University. Ilmenau, Germany., 2005.

[18] D. L. Means and K. W. Chan. "Evaluating Compliance with FCC Guidelines for Human Exposure to Radiofrequency Electromagnetic Fields". Technical report, Federal Communications Commission Office of Engineering & Technology, 2001.

[19] W. Joseph and L. Martens. Comparison of Safety Distances Based on the Electromagnetic Field and Based on the SAR for Occupational Exposure of a 900-MHz Base Station Antenna. *IEEE Transactions on Electromagnetic Compatibility*, 47 (4): pages 977–985, 2005.

[20] *IEEE Recommended Practice for Determining the Peak Spatial-Average Specific Absorption Rate (SAR) in the Human Head from Wireless Communications Devices: Measurement Techniques*, 2003.

[21] J. B. Andersen, K. L. Chee, M. Jacob, G. F. Pedersen, T. Kürner. "Reverberation and Absorption in an Aircraft Cabin with the Impact of Passengers". *IEEE Trans. Antennas and Propag.*, 60 (5): pages 2472–2480, 2012.

[22] *Schmid & Partner Engineering AG, SEMCAD-X.*, http://www.speag.com/, 2009. www.semcad.com.

[23] F. W. Smith D. E. Merewether, R. Fisher. "On Implementing a Numeric Huygen's Source Scheme in a Finite Difference Program to Illustrate Scattering Bodies". *IEEE Trans. Nucl. Sci.*, 27 (6): pages 1829–1833, 1980.

[24] F. Moglie, and A. P. Pastore. "FDTD Analysis of Plane Wave Superposition to Simulate Susceptibility Tests in Reverberation Chambers". *IEEE Transa. Electromagn. Compat.*, 48 (1): pages 195–202, 2006.

[25] V. M. Primiani and F. Moglie. "Numerical Simulation of Reverberation Chamber Parameters Affecting the Received Power Statistics". *IEEE Trans. Electromagn. Compat.*, 54 (3): pages 522–532, 2012.

[26] M. Landmann, K. Sivasondhivat, J. I. Takada, I. Ida, and R. Thomä. "Polarization Behavior of Discrete Multipath and Diffuse Scattering in Urban Environments at 4.5 GHz". *EURASIP Journal on Wireless Communications and Networking*, 2007.

[27] E. M. Vitucci, F. Mani, V. Degli-Esposti, and C. Oestges. "Dense Multipath Depolarization in Outdoor and Indoor Radio Transmissions ". In *31st URSI General Assembly and Scientific Symposium, Beijing, China*, 2014.

[28] H. Kuttruff. *"Room Acoustics"*. Spon Press, London, 2000.

[29] K. Kalliola, K. Sulonen, H. Laitinen, O. Kivekas, J. Krogerus, and P. Vainikainen. "Angular Power Distribution and Mean Effective Gain of Mobile Antenna in Different Propagation Environments". *IEEE Trans. Veh. Technol.*, 51 (5): pages 823–838, 2002.

[30] S. Iskra, R. McKenzie, and I. Cosic. "Monte Carlo simulations of the electric field close to the body in realistic environments for application in personal radiofrequency dosimetry". *Radiat. Prot. Dosim.*, 147 (4): pages 517–527, 2011.

[31] J. B. Andersen, J. Ø. Nielsen, G. F. Pedersen, G. Bauch, and M. Herdin. "Room Electromagnetics". *IEEE Antennas Propagat. Mag.*, 49, (2): pages 27–33, 2007.

[32] A. Thielens, S. Agneessens, L. Verloock, E. Tanghe, H. Rogier, L. Martens, and W. Joseph. "On-Body Calibration and Processing for a Combination of two Radio-Frequency Personal Exposimeters". *Radiat. Prot. Dosim.*, April 2014. doi:10.1093/rpd/ncu056.

[33] D. A. Hill. "Spatial Correlation Function for Field in a Reverberation Chamber". *IEEE Trans. Electromagn. Compat.*, 37: pages 138–145, 1995.

[34] G. Vermeeren, W. Joseph, C. Olivier, and L. Martens. "Statistical multipath exposure of a human in a realistic electromagnetic environment". *Health Physics*, 94, no. 4: pages 345–354, 2008.

[35] Craig F. Bohren, and Donald R. Huffman. *Absorption and Scattering of Light by Small Particles.* John Wiley & Sons, Inc., 1998.

[36] D. Du Bois and E. F. Du Bois. "A formula to estimate the approximate surface area if height and weight be known". *Arch Intern Medicine.*, 17: pages 863–871., 1916.

[37] S. Fujimoto, T. Watanabe, A. Sakamoto, K. Yukawa, K. Morimoto. "Studies on the physical surface area of Japanese. 18. Calculation formulae in three stages over all ages". *Nippon Eiseigaku Zasshi*, 5: pages 443–450., 1968.

[38] E. A. Gehan and S. L George. "Estimation of human body surface area from height and weight". *Cancer chemother Rep*, 54: pages 225–235, 1970.

[39] E. H. Livingston and S. Lee. "Body surface area prediction in normal-weight and obese patients". *American Journal of Physiology - Endocrinology and Metabolism*, 281: pages E586–E591, 2001.

3

Experimental assessment of the reverberation time in indoor environments using room electromagnetics

3.1 Introduction

Several works [1–6] have addressed the propagation of electromagnetic fields (EMF) in indoor environments. These works mainly focus on few specular electromagnetic paths, i.e., paths that stem from specular reflections (Section 1.2.1) or LOS. These works range from experimental investigations to numerical researches. Currently, propagation models such as the ones of [7–10] are complex and are not taking into account the diffuse field's propagation (Section 1.2.1). As shown previously, *room electromagnetics* theory has become an interesting solution to describe the propagation of the diffuse fields in indoor environments [11]. The room electromagnetics theory is an appealing approach compared to the existing methods such as the numerical or empirical approximations. This is because it does not require full knowledge of all the details of the propagation environment, which are extremely difficult - if not impossible - to obtain with accuracy.

The knowledge of the reverberation time is very interesting because it is a function of the area absorbing diffuse fields' energy (as we showed in Section 1.3.1 of Chapter 1), allowing to predict the power absorbed in the human body when present.

The reverberation time has also been investigated in indoor scenarios [11, 12]. In this chapter, the reverberation time is determined using two different measurement systems, namely the channel sounder and the virtual MIMO channel sounder in different realistic environments. The use of the virtual MIMO system has several benefits. It is much cheaper than the real channel sounder, and there is no coupling between the an-

tenna elements, etc. The drawback of using a virtual MIMO channel sounder is the increased measurement time, but the measurement of the reverberation time within the context of this work takes only few minutes. However, the use of the virtual channel sounder does not allow investigations of the channel in dynamic scenarios as the environment is assumed to be static. This chapter aims at characterizing the reverberation time in realistic indoor environments rather than in the ideal reverberation chamber. Further, the $\text{ACS}_{wb,dmc}$ of humans in these realistic offices are determined. The case of room-to-room electromagnetics is also addressed and validated with experiments.

The outline of this chapter is as follows: the two measurement systems, their configuration, and the investigated environments are described in Section 3.2. Section 3.3 addresses the benchmarking of the reverberation time. The diffuse absorption cross section of a person is determined in a realistic office in Section 3.4. Conclusions are drawn in Section 3.5.

3.2   Configuration and environment

3.2.1   Virtual Multiple-Input Multiple-Output channel sounder setup

The virtual channel sounder setup for the multiple-input single-output (MISO) measurements is shown in Fig. 3.1.
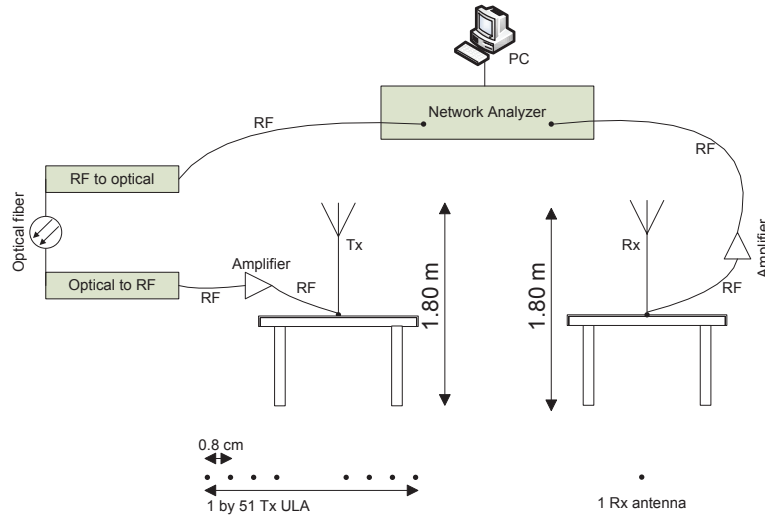
Figure 3.1: Virtual channel sounder setup

A network analyzer (Rohde&Schwarz ZVR) is used to measure the complex channel frequency response for a set of transmitting and receiving antenna positions. The channel is probed in a 500-MHz measurement bandwidth with a frequency step of 1.25 MHz (resulting in 401 frequency points) and a central frequency of 2.30 GHz. As transmitting (Tx) and receiving (Rx) antennas, broadband omnidirectional bi-conical antennas

of type Electro-Metrics EM-6116 are used. In order to perform measurements for large Tx-Rx separations, one port of the network analyzer is connected to the Tx through an Radio Frequency (RF)/optical fiber link with an optical fiber of length 500 m. A pulse signal (in the time domain) generated by the network analyzer is sent to the Tx via the optical fiber. The RF signal sent into the Tx and the RF signal coming from the Rx are both amplified using an amplifier of type Nextec-RF NB00453 with an average gain of 37 dB. The amplifiers assure that the signal-to-noise ratio (SNR) at the receiving port of the network analyzer is at least 20 dB for each measured location of the Tx and Rx. The calibration of the network analyzer is done at the connectors of the Tx and Rx antennas, and as such includes both the RF/optical link and the amplifiers.

The Rx is fixed and the Tx is positioned at 51 different locations forming a virtual uniform linear array (ULA). Both antennas are vertically polarized and positioned at a height of 1.80 m during the measurements. The separation between two adjacent positions in the array is 8 mm, which is larger than one half of the wavelength; this is to make sure that two adjacent positions will be spatially uncorrelated. One measurement (all 51 virtual antenna positions of the array) lasts about 5 minutes. At each Tx position in the array, the network analyzer measures the S_{21} scattering parameter ten times, i.e., 10 time observations are obtained.

3.2.2 Real channel sounder setup

The measurements were also carried out using a MIMO channel sounder. The system allows truly simultaneous measurements of all up to 8 Rx and 16 Tx branches. Details of the measurement system can be found in [13]. The main characteristics of the setup used in this set of measurements are as follows.

1. Measurements are triggered at 60 Hz. This ensures proper sampling of the channel, which is changing due to both movements of the Tx-Rx and other external changes.

2. Central frequency at 2.30 GHz and a bandwidth of 100 MHz. The bandwidth is limited by the chip rate of the pseudo-noise (PN) sequence used to transmit the signal at the Tx side. The PN sequence is transmitted using a binary phase shift keying (BPSK), which is robust but does not allow transmission at higher rate [13].

3. Measurement duration: 10 seconds (600 measurements)

4. Rx channels: four laptop arrays are measured simultaneously, each with four antennas (measured via switch). The laptop arrays have two top-mounted and two side-mounted dipole-like antennas.

5. Tx channels: four dual-band branches, four linear arrays with vertically polarized elements. Each of the four laptops is placed on a table in front of a person. During each measurement, the persons are moving the laptops randomly on the table with displacements of approximately $\pm$ 10 cm. The power delay profiles (PDPs) are further obtained by averaging over all the measurements made with the four antennas on the laptop.

3.2.3 Description of the environments

Environment in Aalborg, Denmark

The measurements were performed in a seminar room of Aalborg university (AAU). Only the right part of the room is used and is shown in Fig. 3.2.
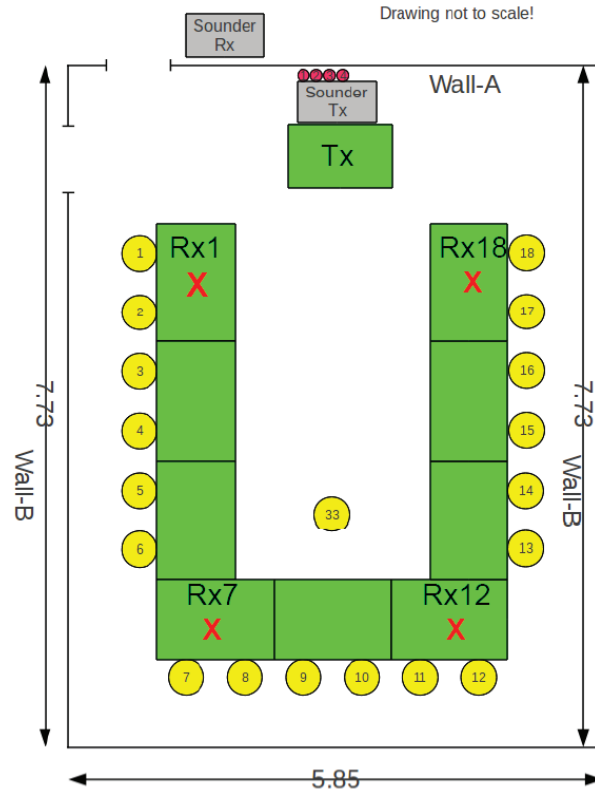
Figure 3.2: Seminar room in Aalborg: Tx and Rx measurement positions. The room dimensions are in meters

Position	Distance to Wall A (m)	Distance to Wall B (m)
Rx1	2.5	4.6
Rx7	6.4	4.4
Rx12	6.5	1.4
Rx18	2.5	1

Table 3.1: Locations for Rx in the seminar room in Aalborg

The room is equipped with tables, chairs, and ordinary meeting room facilities. The locations for Rx in this room are summarized in Table 3.1. The Tx antennas were at fixed positions whereas the Rx occupied positions Rx1, Rx7, Rx12, and Rx18 as shown in Fig. 3.2.

Environment in Ghent, Belgium

The measurements were performed with the virtual MIMO channel sounder in the room C3/3-3 and its adjacent room C3/3-4 at the third floor of an office building in Ghent, Belgium. The ground plan is shown in Fig. 3.3. This floor is comprised of different rooms indexed by C3/3-i, where i is the ith room. We are only interested in rooms C3/3-3 and C3/3-4 within the context of these measurements. A description of these rooms is as follows: both rooms contain desks (with chairs, computers, etc.), people, dressers, and other furniture such as books, cardboards, etc. We performed two kind of measurements: one is where the Tx and Rx are located in the same room (C3/3-3) and the other is performed using both rooms (Tx in adjacent room C3/3-4). For the same room measurements, both the Tx-Rx are located in room C3/3-3 (room-room, indexed further by RR). In the case of the adjacent room measurements, the Tx is located in the room C3/3-3 whereas the Rx is located in room C3/3-4 (adjacent rooms, indexed by AR).
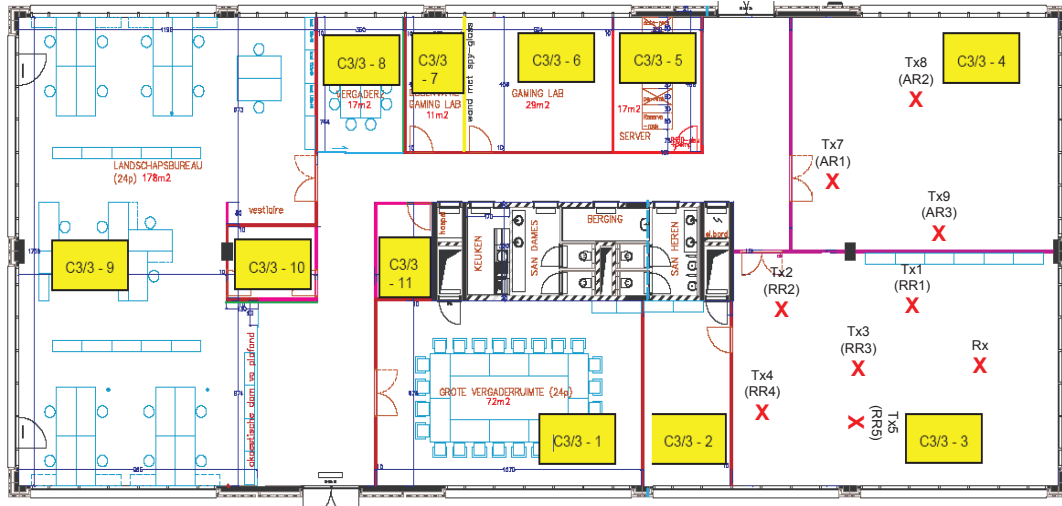
Figure 3.3: Third floor of office building in Ghent. The building dimensions are L×W×H=41.70 m×17 m×2.675 m. The measurements were performed in the rooms C3/3-3 (13.18 m×8.48 m×2.675 m) and C3/3-4 (10.78 m×8.48 m×2.675 m)

3.2.4 Theory of the reverberation time in adjacent rooms

Here, we investigate the reverberation time in adjacent rooms. We assume that the walls separating the rooms permit electromagnetic energy exchanges between the rooms. Let us consider the floor plan of Fig. 3.3. The Tx is located in room C3/3-4 (R_{Tx}) while the Rx is located in room C3/3-3 (R_{Rx}). The basic theory is the same as the case where the transceivers are located in the same room, except that there are energy exchanges between the two rooms [14]. Both rooms are separated by a wall with surface S. P(t) is the power transmitted in room R_{Tx} and α is the wall transmission factor.

In the following, we assume complete diffuse fields in both rooms. Therefore, the power density is direction independent as it is assumed in [11] as well. Once P(t) is launched in the room R_{Tx}, the room R_{Rx} will be

fed by two sources of power:

1. $\alpha^2 P(t)$, which is the transmitted LOS power scaled by the wall transmission coefficient.

2. P_{exch}, which is due to the diffuse energy exchanged from room R_{Tx} to room R_{rx} through the wall with surface S.

These received input powers in room R_{Rx} are further equal to the increase in energy per second inside the room plus the losses through the surfaces (walls, floor, ceiling, furniture, etc.) [11].

$$\alpha^2 P(t) + P_{exch} = V\frac{dW_{Rx}}{dt} + \frac{c_0 \eta A}{4}W_{Rx} \tag{3.1}$$

where V, A, W_{Rx} are the room volume, the total absorbing area, the energy density in the room R_{Rx}, respectively, and η is the average fraction of energy absorbed by the surfaces. Equation (3.1) is similar to the one obtained for the same room case [11].

Assume that the diffuse energy density W and the diffuse power density I in both rooms are related as follows: $W_{Rx}=\alpha^2 W_{Tx}$ and $I_{Rx}=\alpha^2 I_{Tx}$. As the diffuse intensity $I_{Tx}(\theta,\varphi)$ impinges uniformly on the wall S - with α being the transmission factor - then the transmitted power via the surface S to the room R_{Rx} is:

$$\begin{aligned} P_{exch} &= S\int_0^{2\pi}\int_0^{\frac{\pi}{2}} \alpha^2 I_{Tx}(\theta,\varphi)\sin(\theta)\cos(\theta)d\theta d\varphi \\ &= \pi\alpha^2 I_{Tx}S \\ &= \pi I_{Rx}S \end{aligned} \tag{3.2}$$

As we have seen in the first chapter, the energy density in diffuse fields and the power density are related as follows:

$$W = 4\pi\frac{I}{c_0} \tag{3.3}$$

Therefore, substituting (3.3) in (3.2), P_{exch} is expressed as a function of the diffuse energy density as follows:

$$P_{exch} = \frac{c_0 S}{4}W_{Rx}. \tag{3.4}$$

If the source is turned off, i.e., P(t)=0 for t> 0, and using (3.4), (3.1) turns to

$$V\frac{dW_{Rx}}{dt} + \frac{c_0}{4}(\eta A - S)W_{Rx} = 0, \tag{3.5}$$

which is a homogeneous differential equation and its solution is as:

$$W_{Rx} = W_0 e^{-\frac{t}{\tau}} \tag{3.6}$$

with

$$\tau = \frac{\tau_0}{1 - \frac{S}{\eta A}} \qquad \text{where } \tau_0 = \frac{4V}{c_0 \eta A}. \tag{3.7}$$

Here τ_0 is the reverberation time when both Tx and Rx are located in the same room R_{Rx}, i.e., room C3/3-3 in Fig. 3.3, and τ is the reverberation time when Tx and Rx are in adjacent rooms, i.e., Tx in room C3/3-4 and Rx in room C3/3-3 (see figure 3.3). Notice that we observe from the theory that $\tau \geq \tau_0$ for $S \leq \eta A$.

3.3 Benchmarking of the reverberation time and absorption cross section measurement

3.3.1 Channel sounder versus virtual channel sounder

In order to validate the measurements performed with the virtual channel sounder, we compare them with those obtained from the channel sounder. The measurements campaign has been carried out in the same room in Aalborg (see Fig. 3.2) with both measurement systems but at different dates. The room volume is about 118 m^3. The measurements have been done at different dates but the Tx and Rx locations were the same (as best as possible) for the two measurements campaign.

Tables 3.2 and 3.3 summarize the results for the reverberation time obtained for both measurement systems. D, n, τ, and A' represent the Tx-Rx separation, number of persons present in the room during the measurements, reverberation time, and the effective absorption area, respectively. As we are mainly interested

Position	D (m)	n	τ (ns)	A' (m^2)
Rx1	3.4	6	23.1	68
Rx7	4	6	22.7	69.3
Rx12	6.2	6	26.8	61.2
Rx12	6.2	9	25.5	61.7
Rx12	6.2	12	25.3	62.1
Rx12	6.2	15	26.1	60.3
Rx18	2.7	12	25.3	62.1

Table 3.2: Parameters from the real channel sounder measurement

Position	D (m)	n	τ (ns)	A' (m^2)
Rx1	3.6	0	24.5	64.2
Rx1	3.6	2	23.8	66.2
Rx7	7.2	2	25.2	62.5
Rx7	7.2	4	25.1	62.7
Rx7	7.2	18	22	71.5
Rx12	6	2	28.2	55.8
Rx18	3	2	26	60.6

Table 3.3: Parameters from the virtual channel sounder measurement

into the reverberation time τ, we focus the comparison on this parameter as illustrated in the diagram chart of Fig. 3.4. Although τ is theoretically dependent on the number of person n, i.e., (1.20), this is not clear in the measurements performed with two different systems. Therefore, we will compare the mean values obtained with the two measurement systems irrespective of the number of persons. For the channel sounder, we obtain a mean value of τ (τ_{mean}) equal to 25 ns with a standard deviation (σ_τ) of about 1.50 ns, which
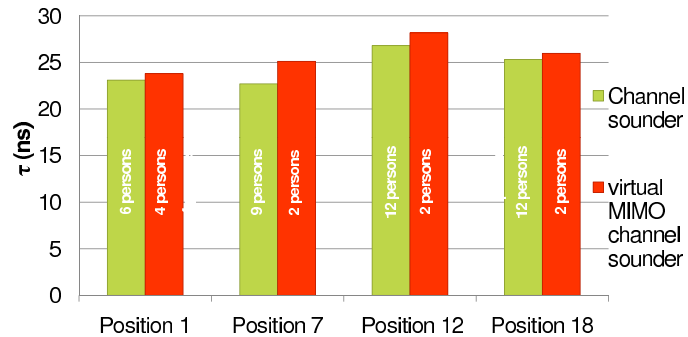
Figure 3.4: Differences in the reverberation time values for the channel sounder and the virtual channel sounder in 4 positions of Rx

is 6% of τ_{mean}. We obtain τ_{mean} of about 25 ns and σ_τ of about 1.90 ns (7.60% of τ_{mean}) for the virtual channel sounder. We obtain similar mean value of the reverberation time for the two measurement systems. The observed small discrepancies between the results of the two measurement systems at different positions may be due to the following reasons:

1. Differences between the measurement system setups.

2. Variations in the Tx-Rx separations: for a certain position of Tx and Rx, the Tx-Rx separation (see second column of Tables 3.2 and 3.3) may not be exactly the same for the two measurements campaign since they have been carried out at different dates. However, the room electromagnetics theory states that the reverberation time value should be independent of the Tx-Rx location if we assume that only complete diffuse scattered fields are present.

3. Furniture, people, and other objects in the room were probably not exactly at the same positions during both measurement campaigns.

4. Different number of people in the room as this is illustrated in the diagram chart of Fig. 3.4.

Given the small deviations between the reverberation time values obtained for each measurement system at the different locations, we can conclude that the reverberation time is independent of the transceiver location, as suggested by the room electromagnetics theory [11]. Moreover, our investigation also evidences that the reverberation time is independent of the measurement system.

3.3.2   Influence of different antennas

Using the virtual channel sounder setup, we investigate the reverberation time variation using different antennas. We first use a broadband omnidirectional biconical antenna of type Electro-Metrics EM-6116 denoted here as *iMinds* and then the laptop antennas mentioned in Section 3.2.2 and denoted as *aau*. Table 3.4 summarizes the results for the two antennas. For the omnidirectional biconical antenna, we obtain a mean value of τ of about 25.90 ns whereas we obtain τ_{mean} of about 24.10 ns for the laptop antenna, which results

Position	D_{iMinds} (m)	D_{aau} (m)	n_{iMinds}	n_{aau}	$\tau_{(iMinds)}$ (ns)	$\tau_{(aau)}$ (ns)
Rx1	3.6	3.6	1	1	24.1	24.9
Rx7	7.2	6.6	2	1	25.2	23.7
Rx12	6	6	2	1	28.2	25.8
Rx18	3	2.4	2	1	26	22

Table 3.4: Parameters for two antennas using the virtual channel sounder, iMinds = biconical antenna from Ghent university and aau = laptop antenna from Aalborg university

in a difference of 1.80 ns (only 7.20% of the mean value). Few variations between the results were observed, but this was due to the reasons mentioned in Section 3.3.1. Again, we find almost the same mean values of the reverberation time using one measurement system with different antennas, indicating that the reverberation time is independent of the antennas although it should be noted that the polarization might have a slight influence (Chapter 2).

3.3.3 Results of the adjacent room measurements

We now present the results of the reverberation time measurements in adjacent rooms, validating the theory developed in Section 3.2.4. Let us recall that Tx was located in room C3/3-4 and Rx in room C3/3-3 (Fig. 3.3) for the adjacent room scenario. The measurement results are shown in Fig. 3.5. The mean values of the reverberation time for the same room and adjacent rooms scenarios are $\tau_0 = 45.32$ ns and $\tau = 58.90$ ns, respectively. It is clear from Fig. 3.5 that the reverberation time values for the same room scenario are always lower than the ones obtained for the adjacent rooms scenario (i.e., $\tau_0 \leq \tau$) as theoretically expressed in (3.7). This is because the diffuse fields present in the same room scenario stem from scattering from the internal walls and other surfaces in the room whereas in the adjacent room scenario, the diffuse fields stem not only from internal walls and surfaces, but the room is also fed by fields from the adjacent room. Therefore, the diffuse fields in the adjacent rooms scenario will be more important than in the same room scenario, leading to a larger reverberation time. The variation of the reverberation time in both scenarios is mainly attributed to the change in the number of people in the room, given that this influences the total absorbing area and hence the reverberation time value.
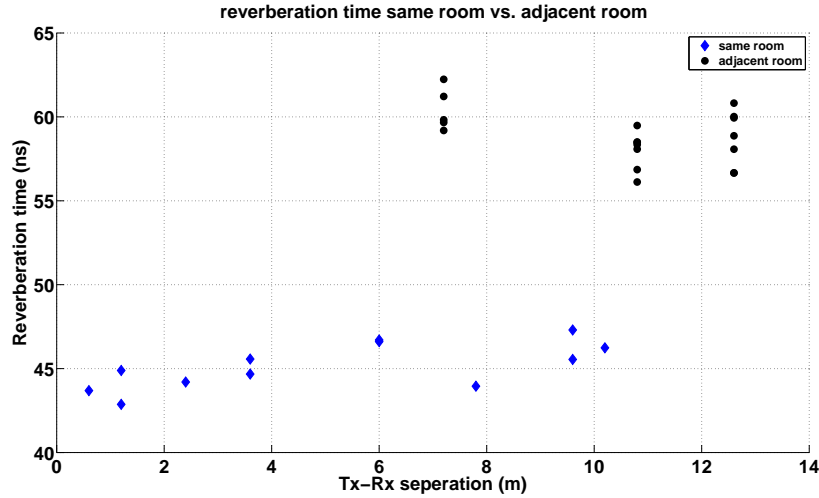
Figure 3.5: Reverberation time as a function of Tx-Rx separation for the same room and adjacent rooms scenarios

In order to validate (3.7), we determine the ratio $\frac{\tau_0}{\tau}$ from both the measurements and the theory, i.e., $\frac{\tau_0}{\tau}\big|_{meas}$ and $\frac{\tau_0}{\tau}\big|_{th}$, respectively. From (3.7), we can derive the expression of $\frac{\tau_0}{\tau}\big|_{th}$ as follows:

$$\frac{\tau_0}{\tau}\Big|_{th} = 1 - \frac{S}{A'} \qquad \text{with A' defined in (2.8)}$$

The wall surface S is about 28 m^2 and A' is determined from τ_0 and the room volume and is about 105 m^2. Therefore, we obtain $\frac{\tau_0}{\tau}\big|_{th}$ of about 0.735 whereas $\frac{\tau_0}{\tau}\big|_{meas}$ is obtained from the measured values of τ_0 and τ and is about 0.769, resulting in a relative deviation of only 4.40%. This small deviation between the theoretical and measured reverberation time values for adjacent rooms scenario shows that the measurement results are in good agreement with the calculation using the proposed theory.

3.4 Measurement of the absorption cross section in diffuse fields

The measurements were performed in the office room C3/3-3 (volume≈360 m^3) shown in Fig. 3.3. Three spatial locations for Tx and a fixed location for Rx are selected. Measurement data at frequencies 2.30 GHz and 3 GHz were used. The diffuse absorption cross section is determined from the absorbing areas as expressed in (2.7). We performed the measurements while varying successively the number of people in the room. As a result, different values of absorbing areas are obtained as a function of the room occupation with people. For a given occupation of the room, the effective absorbing area is obtained from the measured reverberation time value and the room volume, see (2.8). Since we have assumed that the people in the room have equal body surface, the diffuse absorption cross section of a person is determined as the slope of the regression line fitting the absorbing area as a function of number of people (see Section 2.3.3). An
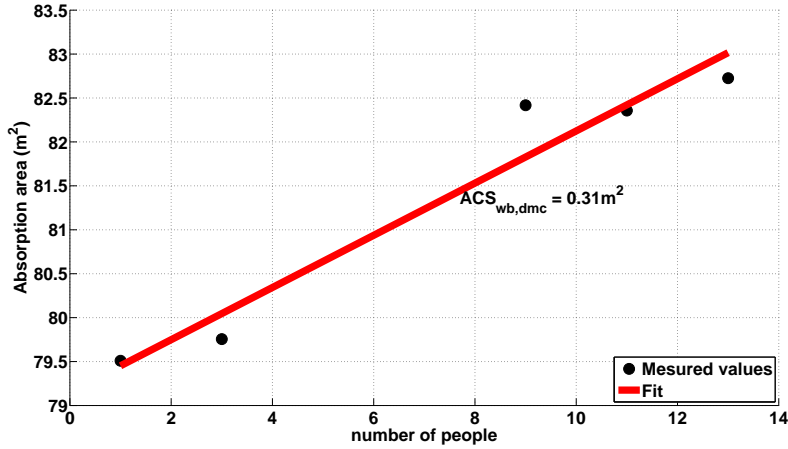
Figure 3.6: Absorption area as a function of the room occupation, along with the experimental absorption cross section in diffuse fields. R^2=0.95 is the goodness of fit

illustration of the absorbing area at 2.30 GHz as a function of the room occupation is shown in Fig. 3.6. The measurement results in terms of $ACS_{wb,dmc}$ for the different locations and two frequencies are summarized in Table 3.5. An average $ACS_{wb,dmc}$ of about 0.34 m^2 and 0.36 m^2 are obtained at the frequency of 2.30 GHz

Frequencies	Positions			$ACS_{wb,dmc}^{mean}$
	position 1	position 2	position 3	
2.3 GHz	0.42 m ^{2}	0.28 m ^{2}	0.31 m ^{2}	0.34 m ^{2}
3 GHz	0.24 m ^{2}	0.43 m ^{2}	0.42 m ^{2}	0.36 m ^{2}

Table 3.5: Diffuse absorption cross section ($ACS_{wb,dmc}$) from measurement data

and 3 GHz, respectively. We observe that the average $ACS_{wb,dmc}$ varies only slightly for the two frequencies. The frequency variation of the $ACS_{wb,dmc}$ will be addressed in Chapter 5.

However, this experiment shows how one can determine the ACS in diffuse fields from the reverberation time measurements in real indoor environments. The $ACS_{wb,dmc}$ will be used to determine the whole-body absorption rate in the next chapters.

3.5 Conclusions

A closed room environment is viewed as a lossy cavity characterized by possibly a LOS component and diffuse scattered fields from walls and internal objects in realistic indoor environments. A theory used in acoustics and reverberation chambers is applied in this chapter for the electromagnetic case. The capacity of a lossy cavity to store electromagnetic energy is expressed here in terms of the reverberation time, i.e.,

the decay rate of the diffuse fields. The goal of this chapter aimed toward validation of the assessment of the reverberation time in a real indoor environment using the virtual multiple-input multiple-output channel sounder. We showed that the reverberation time is independent of the measurement systems and the used antennas.

In addition, the reverberation time theory has for the first time been extended to the adjacent rooms case. The developed theory is in good agreement with measurement results performed in Ghent.

References

[1] R. Valenzuela. "A ray tracing apapproach to predicting indoor wireless transmission". In *IEEE Veh. Technol. Conf.*, volume 43, pages pages 214–218, 1993.

[2] A. F. Agelet, A. Formella, J. M. H. Rabanos, I. F. de Vicente, and P. F. Fontan. "Efficient ray-tracing acceleration techniques for radio prpropagation modeling". *IEEETrans. Veh. Technol.*, 49: pages 2089–2104, 2000.

[3] K. A. Remley, H. R. Anderson, and A. Weisshar. "Improving the accuracy of ray-tracing techniques for indoor propagation modeling". In *IEEE Veh. Technol. Conf.*, volume 49, pages pages 2350–2358, 2000.

[4] M. Iskander, Z. Yun, and Z. Zhang. "Outdoor/Indoor propagation modeling for wireless ccommunication systems". In *IEEE Antennas and Propagation Society International Symposium*, volume 2, pages pages 150–153, 2001.

[5] Jean-Marie Gorce, Katia Jaffrés-Runser and Guillaume De La Roche. Deterministic Approach for Fast Simulations of Indoor Radio Wave Propagation. *IEEE Transactions on Antennas and Propagation*, 55, No. 3: pages 938–948, 2007.

[6] Kathy Wei Hurst and Steven W. Ellington. "Path Loss From a Transmitter Inside an Aircraft Cabin to an Exterior Fuselage-Mounted Antenna". *IEEE Trans. Electromagn. Compat.*, 50, No. 3: pages 504–512, 2008.

[7] Claude Oestges and Bruno Clerckx. *"MIMO Wireless Communication: From Real-World Propagation to Space-Time Code Design"*. Academic Press, first edition, 2007.

[8] N. Czink. *The Random-Cluster Model - A Stochastic MIMO Channel Model for Broadband Wireless Communication Systems of the 3rd Generation and Beyond*. PhD thesis, Technische Universität Wien, Forschungszentrum Telekommunikation Wien, Wien, AT, 2007.

[9] 3rd Generation Partnership Project. Spatial Channel Model for MIMO Simulations . Technical report, 3GPP Technical Specification Group Radio Access Network., 2008. ref.: 3GPP TR 25.996 v8.0.0, online: www.3gpp.org.

[10] E.Tanghe, W. Joseph, M. Lienard, A. Nasr, P. Stefanut, L. Martens, and P. Degauque. "Statistical Analysis of Multipath Clustering in an Indoor Office Environment". *EURASIP Journal on Wireless Communications and Networking*, 2011:16 pages, 2011.

[11] J. B. Andersen, J. Ø. Nielsen, G. F. Pedersen, G. Bauch, and M. Herdin. "Room Electromagnetics". *IEEE Antennas Propagat. Mag.*, 49, (2): pages 27–33, 2007.

[12] J. B. Andersen, K. L. Chee, M. Jacob, G. F. Pedersen, T. Kürner. "Reverberation and Absorption in an Aircraft Cabin with the Impact of Passengers". *IEEE Trans. Antennas and Propag.*, 60 (5): pages 2472–2480, 2012.

[13] J. Ø. Nielsen , J. B. Andersen, P. C. F. Eggers, G. F. Pedersen, K. Olesen, H. Suda. "Measurements of indoor $16{\times}32$ wideband MIMO channels at 5.8 GHz". *IEEE Eighth International Symposium on Spread Spectrum Techniques and Applications*, pages 864–868, August 2004.

[14] H. Kuttruff. *"Room Acoustics"*. Spon Press, London, 2000.

[15] S. Fujimoto, T. Watanabe, A. Sakamoto, K. Yukawa, K. Morimoto. "Studies on the physical surface area of Japanese. 18. Calculation formulae in three stages over all ages". *Nippon Eiseigaku Zasshi*, 5: pages 443–450., 1968.

[16] A. Hirata, Y. Nagaya, F. Osamu, T. Nagaoka, S. Watanabe. "Correlation between Absorption Cross Section and Body Surface Area of Human for Far-Field Exposure at GHz Bands". *Electromagnetic Compatibility, 2007. EMC 2007. IEEE International Symposium on*, pages 1–4, July 2007.

[17] E. Conil, A. Hadjem, A. Gati, M. F. Wong and J. Wiart. "Influence of Plane-Wave Incidence Angle on Whole Body and Local Exposure at 2100 MHz". *IEEE Trans. Electromagn. Compat.*, 53, No. 1: pages 48–52, 2011.

4

Experimental whole-body specific absorption rate assessment

4.1 Introduction

The concern of human exposure to electromagnetic radiation has become important. For instance, IC-NIRP [1] defines guidelines to protect humans exposed to electromagnetic radiation. Limit values for the SAR have been defined as the basic restriction for human exposure in the RF band.

The SAR is a quantity difficult to measure in an actual human. Therefore, various works based on numerical computations using methods such as FDTD have assessed the SAR in human phantoms [2–5]. The complexity of the wave propagation and interaction with humans adds additional difficulties in the determination of the SAR in realistic environments, especially in indoor environments. In situ RF exposure of different RF sources is investigated in [6]; over 40 locations were investigated but only 2 are devoted to the indoor environments.

The whole-body averaged SAR (SAR_{wb}) has been determined in a human body model in a realistic electromagnetic environment in [7]. However, the results were obtained using a statistical incident field approach. The absorption of RF EMFs in the frequency range from 50 MHz to 2.50 GHz in an anatomically human body is investigated in [4] where the simulations have been conducted for few incident fields directions, while focusing more on the phantom anatomy. [6] calculates the SAR_{wb} from measurement data obtained with personal exposure meters (PEM) for different human spheroids and frequencies. The authors investigated the absorption for different scenarios, among which the indoor environments.

A geospatial model for RF-EMF prediction is introduced in [8]. The RF-EMF has been predicted for outdoor scenarios, but the indoor scenarios did not meet the same success because of considerable simplifications

made for the investigated indoor environment. This is because the indoor environments are actually very complex, comprised of different parts (the interior walls, the floor, the ceiling, the furniture, etc.) with different electromagnetic properties. Therefore, the propagation mechanisms in such environments must be well understood to faithfully assess the SAR$_{wb}$.

An interesting approach to assess the human absorption rate in a realistic urban environment can be found in [9]. This method simulates a room with thin plates of materials having different properties, while the transmitting antenna (Tx) was located outside the room. Because the propagation mechanism is so complex in indoor environments, a UTD technique is used to account for the fields generated from scatterings and diffractions. Notwithstanding the improvement thanks to the use of UTD, the scalability of combined FDTD/UTD is problematic since the room has to be discretized with the FDTD method.

The objective of this chapter is to propose an experimental methodology to determine the SAR$_{wb}$ by accounting for the absorption due to the diffuse fields. The proposed method is based on the room electromagnetics theory [10] (see Chapter 3), stating that the total power in an indoor environment is comprised of the first specular path, i.e., the LOS component if present, plus the diffuse fields. In this chapter, there will be no distinction between the dense multipath components and the diffuse fields. This approximation holds since one can consider that the power of the weak specular components are included in the power of the first specular component. In other words, all the specular components (weak or strong) are modeled with the LOS component in terms of power density. The novelty of the proposed method potentially lies in its ability to predict the SAR$_{wb}$ in an arbitrary complex indoor environment without huge computations. Most importantly, our simple method accounts for the absorption due to diffuse fields, which may be prominent in indoor environments.

This chapter is organized as follows: The experimental method to determine the SAR$_{wb}$ is presented in Section 4.2. The materials and methods for the validation process can be found in Section 4.3. In Section 4.4, the description of the validation process is given. The results of the validation are presented in Section 4.5 and discussion of the results is provided as well. Finally, conclusions are given in Section 4.6.

4.2 Methodology for the whole-body averaged specific absorption rate assessment

4.2.1 Formulation of the SAR$_{wb}$

As already stated in Chapter 1, the SAR$_{wb}$ is the physical quantity used for defining the basic restrictions for human exposure in the RF band [1]. Basically, the SAR$_{wb}$ is defined as the amount of absorbed power by an individual per mass unity.

Let us recall that the methodology here is based under the room electromagnetics theory (i.e., LOS plus diffuse). The SAR$_{wb}$ of a person can be expressed as follows:

$$SAR_{wb,total} = \frac{P_{abs,pers}}{m} \tag{4.1}$$

$$= \frac{P_{abs,pers,dmc} + P_{abs,pers,los}}{m} \tag{4.2}$$

where $P_{abs,pers}$, $P_{abs,pers,dmc}$, and $P_{abs,pers,los}$, are the total power, diffuse power, and the absorbed power due to the LOS signal, respectively, by a person in Watt and m is his/her mass in kg. Therefore, the SAR$_{wb}$ is expressed in W/kg.

The diffuse field is incident in all directions, such that the power absorbed in diffuse fields by a person is:

$$P_{abs,pers,dmc} = \int \int \eta(\theta,\varphi) I_{dmc}(\theta,\varphi) A(\theta,\varphi) \cos(\theta) \sin(\theta) d\theta d\varphi, \qquad (4.3)$$

where $I_{dmc}(\theta,\varphi)$ is the incoming power density in the azimuth-elevation direction (θ,φ) in (W/m^2). $A(\theta,\varphi)$ and $\eta(\theta,\varphi)$ are the body surface and the fraction of energy absorbed, respectively, by the person in the (θ,φ) direction. Because the power density $I_{dmc}(\theta,\varphi)$ is independent of the direction (θ,φ) in complete diffuse fields, (4.3) is now expressed as:

$$P_{abs,pers,dmc} = I_{dmc} \int \int \eta(\theta,\varphi) A(\theta,\varphi) \cos(\theta) \sin(\theta) d\theta d\varphi$$
$$= I_{dmc} \times ACS_{wb,dmc} \qquad (4.4)$$

where $ACS_{wb,dmc}$ is the whole-body absorption cross section in diffuse fields and characterized in Chapter 2. The expressions of both $\eta(\theta,\varphi)$ and $A(\theta,\varphi)$ are unknown but $ACS_{wb,dmc}$ and I_{dmc} can be determined via measurements.

Now, the absorbed power by a person due to LOS exposure in the (θ,φ)-direction can be defined as:

$$P_{abs,pers,los} = I_{los} \times \eta(\theta,\varphi) A(\theta,\varphi)$$
$$= I_{los} \times ACS(\theta,\varphi)$$
$$= I_{los} \times ACS_{los} \qquad (4.5)$$

where $ACS_{los}(\theta,\varphi)$ is the absorption cross section due to the LOS illumination in the (θ,φ) direction and I_{los} is the power density of the LOS signal, which is direction-independent because an antenna with isotropic radiation pattern (fields coming from all directions with the same magnitude) is assumed. The power density of the LOS signal is computed from the received LOS power and the receiving area of the Rx antenna (Section 4.5.2). ACS_{los} is unknown and cannot be determined through measurements. For its determination, let us assume the following: the incident LOS component only *sees* half of the body, and the front and back of the body are identical in terms of surface area. Thus, the absorption cross section due to the LOS illumination can be empirically approximated as half of the absorption cross section in diffuse fields, i.e.,

$$ACS_{los} = \frac{ACS_{wb,dmc}}{2} \qquad (4.6)$$

Using (4.1), (4.4), (4.5), and (4.6), the total SAR$_{wb}$ is expressed as:

$$SAR_{wb,total} = \frac{ACS_{wb,dmc}(I_{total} + I_{dmc})}{2m} \qquad (4.7)$$

where $I_{total}=I_{dmc}+I_{los}$ is the total incident power density. Other directions and polarization states of the LOS component are considered and investigated in Chapter 5.

We have seen in Chapter 2 that the assessment method of the $ACS_{wb,dmc}$ is based on the reverberation time values when the considered environment is unloaded and loaded. However, the reverberation time value is only valid if diffuse fields are produced that can be used to characterize the room's absorption properties in diffuse fields (i.e., reverberation time independent of the transceivers locations). The diffuse field is mainly attributed to the multiple waves scattered from rough surfaces, to the reflections inside materials caused by irregularities [11], and/or multiple waves diffracted on the edges. Hence, the diffusion phenomena are not favored in indoor environments comprised of only smooth surfaces, e.g., all glass. Therefore, the present experimental method is valid for rooms comprised of rough surfaces (paint walls, ceilings, floor with limestone, etc.) and/or random obstacles (tables, chairs, furniture, etc.). This means that our methodology to determine the SAR_{wb} is suitable for realistic indoor environments. It should also be noted that a surface roughness depends on the considered frequency and is defined by the Rayleigh criterion [12–14].

4.2.2 Experimental whole body SAR results (under LOS only)

In this section, the SAR_{wb} is calculated using (4.7). The result will be compared with values obtained from other methods such as [2, 7]. We use the experimental $ACS_{wb,dmc}$ value obtained in Section 3.4 of the Chapter 3. It has been assumed that all the subjects under test have the same morphology (height = 175 cm and mass = 70 kg) and we found an $ACS_{wb,dmc}$ of about 0.34 m^2 2.3 GHz (see Table 3.5 in Chapter 2). A total power density of 1 W/m^2 at the location of the human (or phantom) and a distance averaged diffuse power density of about 2.3 mW/m^2 taken from [15] were considered. Note that for this example, the diffuse field's power density represents less than 0.3% of the total power. We choose such a lower contribution of the diffuse fields for comparison purpose since this is not accounted for in the existing methods for calculating the SAR_{wb}. Once we know the person mass and the power densities, we now apply (4.7) and an experimental SAR_{wb} of about 2.43 mW/kg is obtained.

In [2], the whole-body averaged SAR calculation has been performed from 100 MHz to 3 GHz with the basic 2 mm resolution of the voxeled model NORMAN using the FDTD algorithm. A SAR_{wb} of about 3.77 mW/kg has been obtained at 3 GHz, resulting in a relative error of about 35%. It is noteworthy to mention that the NORMAN phantom characteristics used in [2] are different from the human morphology used here. A statistical approach is applied in [7] for the SAR_{wb} calculation in an indoor pico-cell environment at 2.45 GHz. The authors used a spheroid average man with similar characteristics (height and mass) as in our experiment and they obtained a mean SAR_{wb} of about 2.7 mW/kg, resulting in a relative error of about 10%. We obtain excellent agreement between this result and our experiment. The SAR_{wb} has been investigated for different phantoms from 20 MHz to 2.4 GHz in [16]. A SAR_{wb} of about 3.75 mW/kg is found for the Visible Human (VH), Zubal, and Korean model at 2.4 GHz. For the NORMAN model, a SAR_{wb} of about 6.25 mW/kg is found at 2.4 GHz whereas a value of 7 mW/kg is found for the female Japan model at the same frequency. [16] mainly shows that the value of the SAR_{wb} depends highly of the considered phantom. The deviation from our experimental SAR_{wb} and the results of [2, 7, 16] may be explained by the difference in the phantom shapes and postures. For instance, for the same body surface area of 1.78 m^2, the absorption cross section variation may reach 0.15 m^2 for two different phantom shapes and/or postures, resulting in a difference of 1.07 mW/kg in the calculated SAR_{wb} values [17]. Compared to the results obtained

in [2, 7, 16], our method leads to the lowest value in terms of absorption. This is mainly attributed to the fact that we have determined the human's ACS in an office room with working people, meaning that all the people were sitting during the measurements whereas the phantoms are standing in the other studies.

However, it is very important to remind that the previous references do not include the diffuse fields. Actually, the comparisons were for single plane wave incidence since the absorption to the diffuse fields has not yet been addressed in the literature. In the following section, the experimental methodology to determine the SAR$_{wb}$ will be validated through numerical simulations and the diffuse fields contribution will be accounted for.

4.3 Materials and methods for the validation of the experimental SAR$_{wb}$ assessment methodology accounting for DMC

In the following, we determine first via experiments the total SAR$_{wb}$ of a canonical phantom located in an office environment, where the diffuse scattered fields may be prominent. Next, numerical simulations of the same phantom validate the experimental procedure.

4.3.1 Presentation of the investigated environment and phantoms

Five identical cylindrical phantoms (Ph1, Ph2, ..., Ph5) in polyvinyl chloride (PVC) with an inner radius of 119.5 mm and an outer radius of 124.5 mm (thickness=5 mm) and a height of 1.5 m have been used and filled with water. Fig. 4.2 shows a figure of the phantom. The same phantoms have been used in the RC in Chapter 2. The phantoms are arbitrarily located in the room C3/3-2 and C3/3-3 shown in Fig. 3.3 and their positions can be seen in Fig. 4.1.
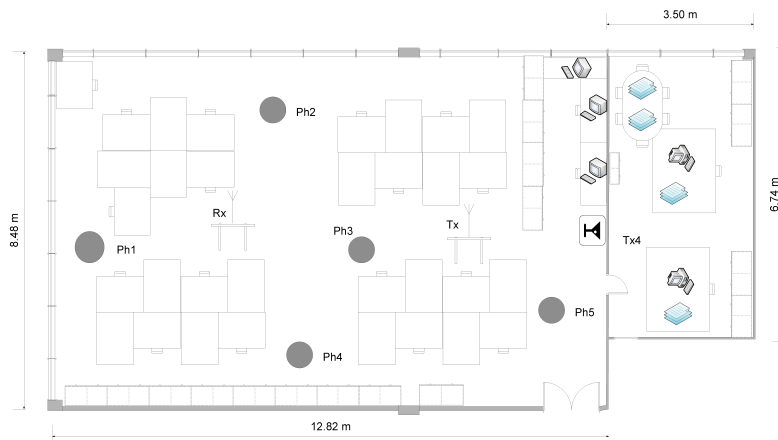
Figure 4.1: Schematic of the phantoms and the transceivers' locations in the investigated room

The PVC electrical properties at 2.8 GHz are as follows: conductivity = 0.003 Ω^{-1}/m and relative permittivity = 2.58. Dosimetric measurements should be performed in phantoms containing liquid that has

dielectric properties similar to those of biological tissues. Given that the purpose of our experiment focuses on the validation of a method rather than simulating actual SAR_{wb} in a human, the cylinders can be filled with any liquid having dielectric properties that allow absorption. For the present work, water has been used to fill the phantoms because it is cheap, available, and easy to manipulate. We have measured the dielectric properties of the water using the open-ended coaxial-line probe (HP85070A dielectric probe kit) with a HP8753D network analyzer [18] and the following values have been obtained at 2.8 GHz: σ=1.58 Ω^{-1}/m (conductivity), ϵ_r=77.32 (permittivity). The water has a mass density of ρ=1000kg/m^3.
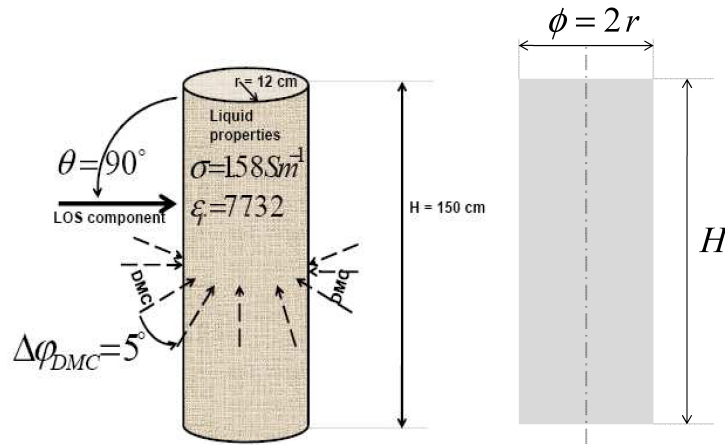
Figure 4.2: A phantom plus the involved power components and the front view

4.3.2 Measurement equipment

A virtual MIMO channel sounder is used to probe the channel. This is justified because we have validated the measurements performed with the virtual channel with those performed with the real channel sounder (see Section 3.3.1 in Chapter 3). The channel sounder is equipped with a single physical antenna at each side, namely Tx and Rx, as shown in Fig. 4.3. A network analyser (Rohde & Schwarz ZVR) is used to measure the complex channel frequency response for a set of transmitting and receiving antenna positions. Broadband omnidirectional biconical antennas of type Electro-Metrics EM-6116 are used for both Tx and Rx. To be able to perform measurements for large Tx-Rx separations, one port of the network analyser is connected to the Tx through an RF/optical link with an optical fiber of length 500 m. We connected the optical fiber to the Tx side because the Tx carriage moves sometimes and the Rx is kept fixed (the Rx and the network analyser are on the same carriage). The signal generated by the network analyser is sent into the Tx via the optical fiber. The RF signal sent into the Tx and the RF signal coming from the Rx are both amplified using an amplifier of type Nextec-RF NB00453 with an average gain of 37 dB.
The amplifiers assure that the signal-to-noise ratio (SNR) at the receiving port of the network analyser is at
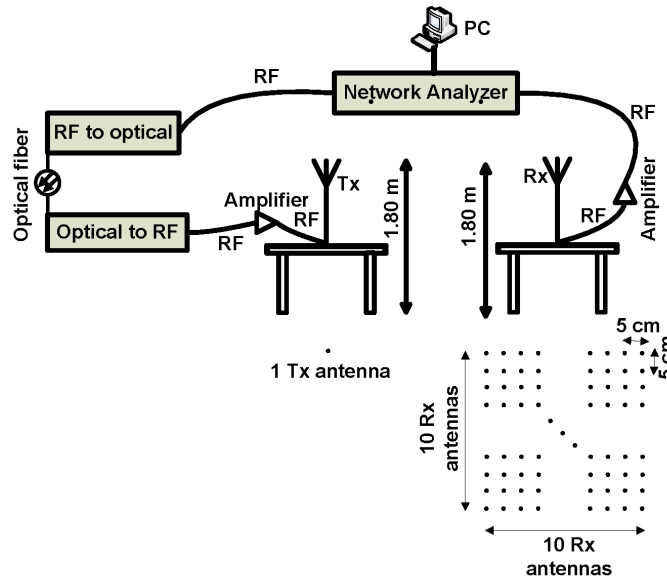
Figure 4.3: Virtual MIMO system illustration

least 20 dB. The calibration of the network analyser is done at the connectors of the Tx and Rx antenna, and include both the RF/optical link and the amplifiers. By means of stepper motors, the antennas are moved from one position to another. Performing measurements with several positions of the Tx and Rx antenna emulate thus a MIMO system (Fig. 4.3). A picture of the virtual MIMO system with the different equipment is shown in Fig. 4.4. The measurements were performed at the frequency of 2.8 GHz within a bandwidth of 200 MHz, with a frequency resolution of 500 kHz (401 frequency points). This band has been chosen because it is representative for the Wireless Local Area Network (WLAN) exposure at 2.4 GHz (2.8 GHz band is chosen instead of 2.4 GHz to avoid interferences with radiation from the wireless devices installed in the building).

For the present measurements, the Tx is fixed and the Rx is positioned at 100 (10×10) different positions forming a virtual uniform rectangular array as shown in Fig. 4.3. Performing measurements with several positions of the antenna in the virtual array and averaging them removes the small-scale fading effects and ensures the PDP to be smooth enough. Both antennas are vertically polarized and positioned at a height of about 1.80 m above the ground.

4.3.3 Numerical settings

For the FDTD simulation, a harmonic excitation was selected. A rectangular plane wave source (the duration of the plane wave is set to 25 periods at 2.8 GHz) is chosen and the Total-Field Scattered-Field (TFSF) technique [19] is used. The maximum grid step in the cylindrical phantom equals 0.077 λ_{ph}, where λ_{ph} is the wavelength in the phantom. This is equivalent to more than 12 cells per wavelength whereas
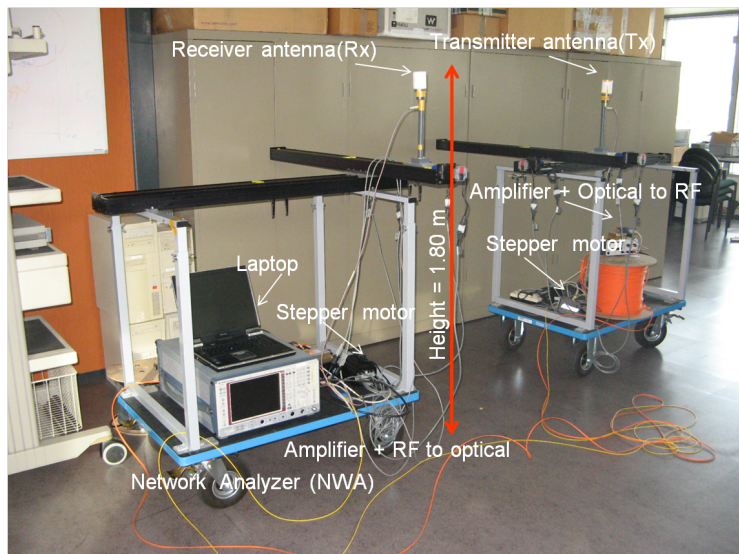
Figure 4.4: A picture of the MIMO measurement system with the different equipment

SEMCAD-X, the used FDTD tool, requires a minimum of 10 cells per wavelength. To avoid reflections of the waves impinging on the boundaries of the simulation domain, uniaxial perfectly match layer (UPML) is used as absorbing boundary conditions. The UPML has been set so that more than 95% of the power of incident waves will be absorbed by the bounday layers. Given the dimensions of the cylinder, we obtain a volume of about 0.068 m^3, leading to a mass of about 68 kg.

The diffuse power density is experimentally determined (Section 4.5.2) and is modeled with plane waves. In the angular domain, the diffuse fields are assumed to have a white azimuthal spectrum [23, 24]. This means that the plane waves used to model the diffuse fields are uniformly distributed over [0-2π[in the azimuthal domain. The elevation of the plane waves is assumed to be in the horizontal plane (θ=90°). We do not know a priori the number of plane waves that would be sufficient to model the diffuse fields. Therefore, the diffuse field is modeled with several sets of plane waves to observe the trend of the results as the number of plane waves in a set is increased. The diffuse field's amplitude is constant in the azimuthal domain, so the amplitude of a plane wave equals the total power density divided by the number of plane waves in the modeling. The phase and polarization of the diffuse fields is similar to the modeling used in Chapter 2. It is important to mention that no matter the number of plane waves used to model the diffuse fields in a given scenario, the total incident power density is constant.

4.4 Description of the validation procedure

The flow chart of the validation methodology is depicted in Fig. 4.5 and the different steps are explained. For the following validation, all incident plane waves are assumed to be in the horizontal plane, i.e., normal

incidence to the phantoms. The diffuse fields's properties have been determined in Section 2.3.4 of Chapter 2 and the LOS component is vertically polarized. We assume a transmitted power of 1 W.
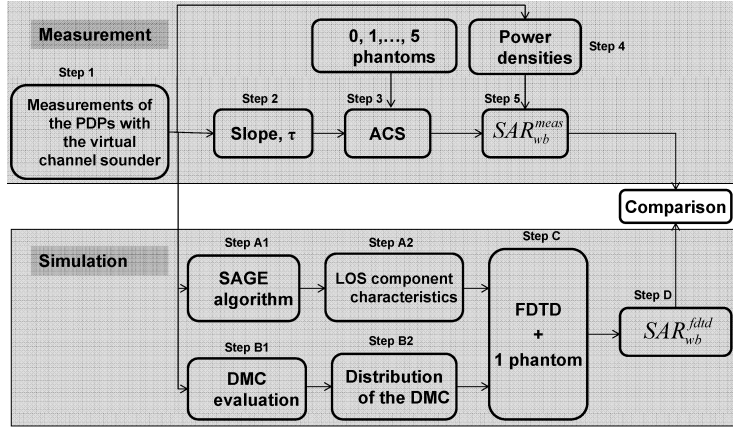
Figure 4.5: Flow chart of the validation of the experimental assessment of the SAR_{wb}

We use five phantoms to assess the $ACS_{wb,dmc}$ of one phantom, i.e., the total surface of the phantom illuminated in completely diffuse fields. The $ACS_{wb,dmc}$ could be derived from measurements performed with only one phantom. However, because of the measurement uncertainties, the results are more accurate if an averaging of the $ACS_{wb,dmc}$ is done over a large number of phantoms (five in our case). We choose to determine the SAR_{wb} in a homogeneous phantom instead of humans because we want to focus more on the validation process rather than checking the compliance with the basic restrictions or reference levels issued by the ICNIRP or other regulatory organisms. Furthermore, it is practically difficult if not impossible to have humans with the same body surface (for an accurate assessment of the $ACS_{wb,dmc}$ by only a few measurements as we have seen in Chapter 3). Another benefit of the use of the phantom is that this one can be simulated in FDTD software.

4.4.1   Experimental procedure

Basically, the experimental assessment of the SAR_{wb} is comprised of two parts as we have seen in Section 4.2: the determination of the diffuse absorption cross section of the phantom and the determination of the incident power densities.

In a first step (Step 1 in Fig. 4.5), the measurements of the PDP are performed using the virtual channel sounder. Then, the reverberation time is determined from the PDP in the Step 2 of Fig. 4.5. Since the reverberation time is now known, the related absorbing area for a given number of the phantom in the room is easily computed with (2.8). The average $ACS_{wb,dmc}$ of the cylinder is further determined from those values (Step 3). In the Step 4, the experimental LOS component power density is investigated based on the Friis equation [20] and the diffuse power density as well (see Section 4.5.2). In step 5 of Fig. 4.5, the

$ACS_{wb,dmc}$ of the phantom in diffuse fields, i.e., $ACS_{wb,dmc}^{ph}$ (the subscript *ph* stands for *phantom*) and the one obtained from the LOS component illumination, i.e., ACS_{los}^{ph} are combined with the power densities to calculate the total SAR_{wb}. For the calculation of the ACS due to the LOS component, the absorption cross section due to diffuse fields cannot be used since the LOS plane wave does not *see* the whole phantom, but it rather *sees* the front view of the cylinder. Let us now determine the ACS of the cylindrical phantom for an incident plane wave. The whole-body absorption cross section in diffuse fields of the cylinder ($ACS_{wb,dmc}^{ph}$) is determined from the measurements. From (2.8), it can be easily shown that $ACS_{wb,dmc}^{ph}=\eta_{ph}A_{ph}$, where η_{ph} and A_{ph} are the average fraction of energy absorbed by the phantom, and the total surface area of the phantom, respectively. Since the incident LOS plane wave *sees* only the front of the cylinder, the associated absorption cross section can be expressed as $ACS_{los}^{ph}=\eta_{ph}A_{ph}^{frontview}$. Therefore, the ACS for diffuse and LOS cases are related as follows:

$$\frac{ACS_{wb,dmc}^{ph}}{ACS_{los}^{ph}} = \frac{\eta_{ph}2\pi rh}{\eta_{ph}2rh} = \pi, \tag{4.8}$$

where r and h are the radius and the height of the cylindrical phantom, respectively (see Fig. 4.2). Obviously, this ratio will depend on the shape of the considered phantom, but it is easy to determine for other geometrical shapes. For instance, we assumed roughly a ratio of 2 for humans in (4.6). However, further simulations are needed to determine accurately the relation between a human's ACS illuminated in diffuse fields and the one resulting in a LOS component illumination for different azimuthal angles. Once this ratio is known, the methodology can be applied for humans since the absorption cross section (in diffuse fields) and the assessment methods for the power densities are independent of the phantom, or human. The method has been applied to the humans in Section 4.2.1 by assuming a ratio of 2 (instead of π for a cylindrical phantom) and a LOS illumination from the back or the front was considered.

Once these absorption cross section values (due to LOS and DMC) are determined, the experimental SAR_{wb} is finally derived as follows:

$$\begin{aligned}
SAR_{wb}^{exp} &= SAR_{wb,spec}^{exp} + SAR_{wb,dmc}^{exp} \\
&= \frac{ACS_{los}^{ph}I_{spec}^{total}}{m} + \frac{ACS_{wb,dmc}^{ph}I_{dmc}}{m} \\
&= \frac{ACS_{wb,dmc}^{ph}I_{spec}^{total}}{\pi m} + \frac{ACS_{wb,dmc}^{ph}I_{dmc}}{m} \\
&= \frac{ACS_{wb,dmc}^{ph}}{m}\left(I_{dmc} + \frac{1}{\pi}\sum_{k=1}^{N_{spec}} I_{spec}^{k}\right)
\end{aligned} \tag{4.9}$$

where $SAR_{wb,spec}^{exp}$, $SAR_{wb,dmc}^{exp}$, m, I_{dmc}, I_{spec}^{k}, and N_{spec} represent the experimental absorption rate due to the specular components, the experimental absorption rate due to diffuse fields, the mass of the phantom, the power density of the diffuse fields, the power density of the kth specular path, and the total number of specular paths, respectively. We introduce here N_{spec} to show that the method can be extended to several specular paths. However, $N_{spec}=1$ for the present experiment as we assume that the LOS is the sole specular component.

70

4.4.2   Numerical procedure

The aim of the numerical simulations is to provide reference SAR_{wb} values so that the experimental SAR_{wb} values could be validated. Again, the SEMCAD-X simulation platform is used for the simulations. The FDTD solver [21] is used to compute numerically the whole-body averaged SAR_{wb} of the cylindrical phantom shown in Fig. 4.2. The dielectric properties of the liquid (water) described in Section 4.3.1 are used in the simulations.

The simulation method is shown in the lower part of the flow chart of Fig. 4.5 and is described as follows. In steps A1-A2, the incident LOS plane wave properties are determined from the measurement data by means of the Space-Alternating Generalized Expectation-Maximization Algorithm (SAGE) [22]. SAGE is an expectation-maximization based estimation algorithm used to determine the characteristics (received power, direction of arrival (DoA), direction of departure (DoD), arrival delay, etc.) of the specular paths contained in measurement data. In our case, we are only interested in the AoA of the LOS signal since the received LOS power will be determined in the experimental procedure (Section 4.5.2). However, the azimuth of the LOS signal will not alter the SAR_{wb} of the phantom due to its symmetry in the azimuthal directions. The azimuth will be important for non-symmetric shapes such as for a real human. Since the vertical polarization was used in the experimental procedure, the same polarization of the incident LOS plane wave is used in the simulation.

In step B1 (Fig. 4.5), the diffuse power density is experimentally determined (Section 4.5.2) and is modeled with plane waves in step B2 (see Section 4.3.3). In step C (Fig. 4.5), the FDTD simulation of the cylinder illuminated by both the LOS signal and the diffuse fields is performed. Finally, the SAR_{wb} values are retrieved in Step D.

4.5   Results and validation

4.5.1   Experimental absorption cross section in diffuse fields

A APDP, the slope value, and the corresponding reverberation time in the investigated room (volume$\approx$360 m^3) without phantoms are shown in Fig. 4.6. We then vary the room occupation to obtain different absorbing area values as a function of the number of phantoms. Hence the absorption cross section is obtained by the determination of the slope of the linear regression of the absorbing areas' values for the different number of phantoms. Fig. 4.7 shows the determination of the $ACS_{wb,dmc}$ (for one time observation) in the considered case by using 0, 1, ..., 5 phantoms. For each set of the phantoms in the room, measurements are performed twice at each location to ensure repeatability. Also 10 sweeps (time observations) have been taken for each measurement. Therefore, 20 values of the absorption cross section of the phantom for the whole measurement campaign are obtained (Step 3 in Fig. 4.5). The average $ACS_{wb,dmc}$ is further determined from those values. We obtained an average absorption cross section value of the phantom in diffuse fields of about 0.39 m^2.

In the next section, the power density of the LOS component and DMC are investigated for the transceivers

71
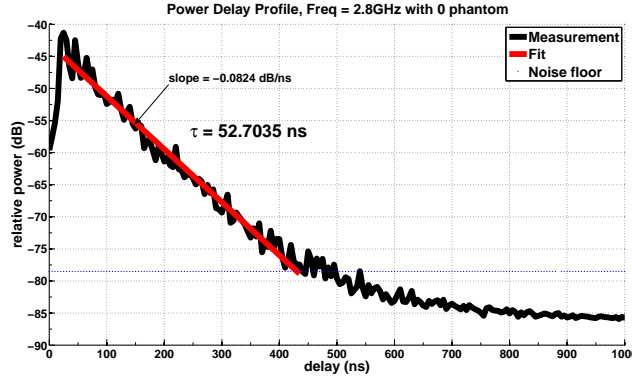
Figure 4.6: A power delay profile with the corresponding tail's slope and the reverberation time

located in the same room. We assume that the antennas have an isotropic radiation pattern. Moreover, we assume the existence of complete diffuse fields, i.e., fields incident in all directions, as in reverberation chambers.

4.5.2 Power density of the LOS component and DMC

The power density of the LOS component is calculated from the experimental received power at a certain position and the Rx effective area. The LOS component power density is [20]

$$I_{los} = \frac{P_r}{A_{eff}}, \tag{4.10}$$

where I_{los}, P_r, and A_{eff} are the power density of the LOS component, the received power, and the effective area of the receiving antenna, respectively. The use of the hypothetical isotropic antenna allows us to write that $A_{eff} = \frac{\lambda^2}{4\pi}$ [20], where λ is the wavelength at the considered frequency. Since we measured the received power and the wavelength is known, it is easy to derive experimentally the power density from (4.10).

$$I_{los}^{exp} = 4\pi \frac{P_r}{\lambda^2} \tag{4.11}$$

Theoretically, the LOS power density from Friis' equation at a distance d_0 from Tx is expressed as:

$$I_{los}^{the} = \frac{P_t}{4\pi d_0^2} \tag{4.12}$$

where P_t is the radiated power by the Tx.

The total power density in diffuse fields has been determined in [25]. Its final expression is repeated here:

$$I_{dmc} = \frac{P_t c_0 \tau}{4\pi V} e^{-\frac{d_0}{c_0 \tau}} \eta_{pol} \tag{4.13}$$

where P_t, c_0, τ, V, d_0, and η_{pol} are the radiated power by the Tx, light velocity in free space, room reverberation time, room volume, shortest distance between the Tx and Rx, and the polarization factor in diffuse
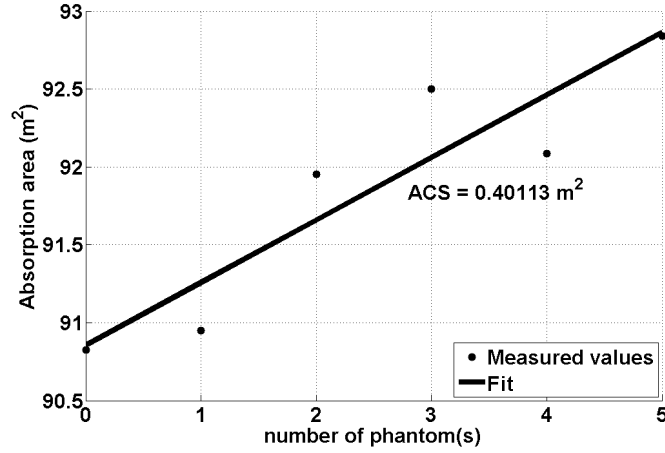
Figure 4.7: Experimental absorption cross section in diffuse fields (ACS$_{wb}$) of the phantom at 2.8 GHz (one time observation). R^2=0.85 is the goodness of fit

fields, respectively. Assuming complete diffuse fields, a polarization factor of 0.5 is considered. This is in agreement with [10, 26] and the measurements performed in RC in Chapter 2.

The measurements have been carried out in the room C3/3-3 of the floor plan shown in Fig. 3.3 of Chapter 3. Fig. 4.8 shows the power densities for the LOS and diffuse field for a transmitted power of 1 W. It can be observed that the experimental LOS power density agrees well with the theoretical LOS power density. The LOS power density is important in the vicinity of the Tx. As the Tx is moved away from the Rx (or vice versa), the LOS power density decreases dramatically, making the power absorption less significant at larger distances. The same trend has been confirmed in [27]. Experimental and theoretical results for the diffuse fields agree very well as well, although it should be noted that the theoretical result is obtained from the experimental reverberation time, see (4.13). The experimental power density in diffuse fields is determined from the experimental diffuse power and the effective area of the Rx (similar to (4.11)). The experimental diffuse power is obtained by subtracting the LOS power to the total received power. The power density of the diffuse fields also decreases with increasing Tx-Rx separation. However, it can be observed from Fig. 4.8 that the LOS field dominates the diffuse fields in the vicinity of the Tx, whereas the diffuse fields dominate for larger Tx-Rx separations. This means that both power densities are equal at a certain distance. This particular distance is the so-called *reverberation distance*. At the reverberation distance location, the LOS field and the diffuse fields have the same intensity. Its theoretical expression has been investigated in [10], and is defined as:

$$R_d = \frac{1}{2}\sqrt{D_t D_r A'}, \tag{4.14}$$

where R_d, D_t, D_r, and A' are the reverberation distance, the Tx directivity, the Rx directivity, and the effective absorbing area, respectively.

In diffuse fields, the power density is direction-independent, and the directivity of both antennas are equal
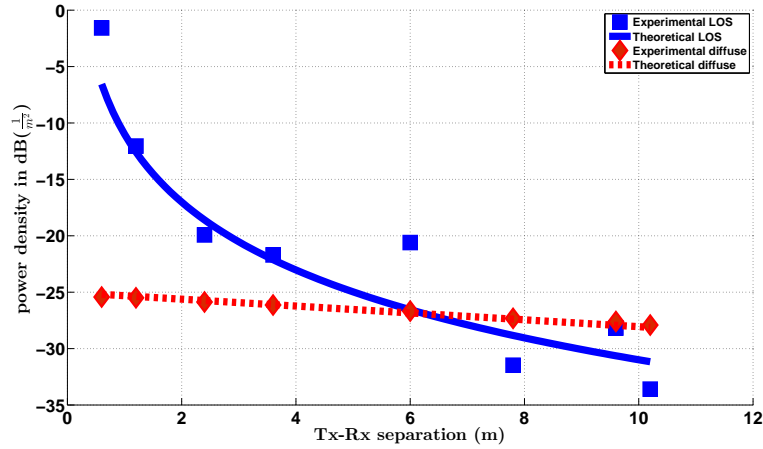
Figure 4.8: Power density for 1 W input as a function of separation between Tx and Rx

to unity (i.e., D_t=D_r=1). The results of the reverberation distance according the Tx-Rx positions are shown in Table 4.1. A mean reverberation distance of about 5.2 m is obtained with a standard deviation of only

Tx-Rx separation (m)	0.6	1.2	2.4	3.6	6	7.8	9.6	10.2
R_d (m)	5.2	5.3	5.2	5.2	5.1	5.2	5.0	5.1

Table 4.1: Reverberation distance values

0.009 m ($\leq$0.2% of the mean value). Therefore, the theoretical reverberation distance is unique for the room and agrees well with the 6 m distance obtained as the intersection of the LOS and diffuse power density curves in Fig. 4.8.

4.5.3 Considered scenarios for the determination of the SAR$_{wb}$

As it can be observed in Fig. 4.8, the contribution of the DMC into the total power increases as the Tx-Rx separation increases. Therefore, the experimental methodology to determine the SAR$_{wb}$ is validated for three scenarios; each scenario corresponds to a certain contribution of the diffuse fields into the total power. Fig. 4.9 shows the relation between the LOS and the diffuse fields power densities in the investigated environment, and is obtained from Fig. 4.8.
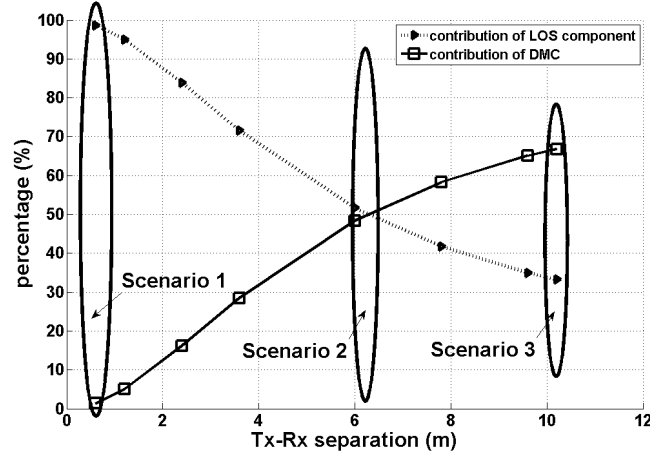
Figure 4.9: Contribution of the diffuse fields and the LOS component in the total power density (under room electromagnetics assumption)

This figure shows that the contribution of the diffuse fields increases with increasing separation between Tx and Rx. This has been also confirmed in measurements in indoor environments [28], where the authors show that the contribution of the dense multipath power density in the total power may vary drastically. The SAR_{wb} of a phantom is then calculated for the three following scenarios (indicated by ellipses in Fig. 4.9).

1. the phantom is in the vicinity of the Tx where the power density of the LOS component is dominant (scenario 1),

2. the phantom is located at the reverberation distance where the LOS component and the diffuse fields have the same contribution in the total power density (scenario 2),

3. the phantom is located far away from the Tx so that the diffuse fields' power density is dominating over the LOS power density (scenario 3).

The LOS component and the diffuse field's power density values for the three scenarios are listed in Table 4.2. The diffuse field power contribution is about 1%, 49%, and 80% for the scenarios 1, 2, and 3, respectively. This agrees with the results in literature [24, 28] wherein the diffuse fields contribution to the total power may reach values up to 95%.

	distance phantom-Tx (m)	LOS power density (mW/m^2)	DMC power density (mW/m^2)	total power density (mW/m^2)
Scenario 1	0.60	694.40 (99%)	2.90 (1%)	697.30
Scenario 2	6.00	2.20 (51%)	2.10 (49%)	4.30
Scenario 3	10.20	0.40 (20%)	1.60 (80%)	2.00

Table 4.2: Power densities for the investigated scenarios

75

4.5.4 Result of the SAR$_{wb}$ from experimental measurements

The total experimental SAR$_{wb}$ values are computed by using (4.9), and the results are listed in Table 4.3. In addition, the diffuse fields' contribution in the total absorption rate is shown for the different scenarios. The diffuse fields' contribution is the ratio between the $SAR_{wb,dmc}^{exp}$ induced only by diffuse fields and the total SAR_{wb}^{exp} induced by the total power density, respectively. In the vicinity of the transmitter (scenario 1) the highest power density (697.3 mW/m^2 in Table 4.2) leads to the highest absorption rate (1.284 mW/kg in Table 4.3). As the phantom is moved away from the transmitter, the total SAR_{wb}^{exp} decreases drastically. It can be clearly seen that the influence of the diffuse fields cannot be neglected in the total absorption rate. Its contribution becomes more and more important for larger separations from the Tx even though the total absorption rate decreases. For instance, the diffuse fields contribution to the total absorption rate in about 1.3 %, 75%, and 93% for the scenario 1, scenario 2, and scenario 3, respectively.

	scenario 1	scenario 2	scenario 3
$SAR_{wb}^{exp}(\mu$W/kg)	1284.30	16.10	9.90
$SAR_{wb,dmc}^{exp}(\mu$W/kg)	16.60	12.00	9.20
Part of DMC in the SAR_{wb}^{exp}	1.3%	75.00%	92.70%

Table 4.3: Experimental SAR_{wb} values for the different scenarios

4.5.5 Results from FDTD simulations

In this section, SAR_{wb}^{fdtd} stands for the whole-body specific absorption rate obtained from the FDTD simulation. ΔSAR is the relative error (in %) between the experimental SAR_{wb} determined in Section 4.5.4 and the simulated SAR_{wb} obtained from the FDTD simulation, and is expressed as follows:

$$\Delta SAR = 100 \times \frac{\left| SAR_{wb}^{exp} - SAR_{wb}^{fdtd} \right|}{SAR_{wb}^{fdtd}} \tag{4.15}$$

As explained before, the diffuse fields are modeled with different numbers of plane waves (0, 8, 16, 32, 64 up to 81) to investigate the convergence and the accuracy of the modeling. We consider a maximum of 81 plane waves because of hardware/software constraints. Table 4.4 shows that the results do not vary much from 75 plane waves. Moreover, modeling the diffuse fields with 81 plane waves gives satisfactory results as it can be observed in Table 4.4. The absorption rate induced by *only* the diffuse fields is also determined from numerical simulations (SAR$_{wb}^{fdtd,dmc}$ in Table 4.4, i.e., second row of each scenario).

The first scenario corresponds to a separation of 0.60 meter between the Tx and the phantom. The incident LOS power density is about 99% of the total power, the remainder is attributed to the diffuse fields power. The experimental absorption rate in this scenario 1 is about 1284.3 μW/kg, while the simulated one is 723.5 μW/kg (81 plane waves, last column in Table 4.4), resulting in a relative error of 77.5%. The relatively large error in the first scenario is certainly due to the influence of the LOS signal (explanation

	no. of pl. waves in the modeling	0	8	16	32	64	75	78	80	81
Scenario 1	$SAR_{wb}^{fdtd}(\mu$W/kg)	668	717	705.3	707.4	717.8	721.5	722.5	723.2	723.5
	$SAR_{wb,dmc}^{fdtd}(\mu$W/kg)	0	3.6	3.3	6.3	12.5	14.7	15.3	15.6	15.8
	% of the DMC in the SAR_{wb}^{fdtd}	0	0.5	0.5	0.9	1.7	2.0	2.1	2.2	2.2
	percentage error (ΔSAR) in %	92.3	79.1	82.0	81.5	78.9	78.0	77.7	77.6	77.5
Scenario 2	$SAR_{wb}^{fdtd}(\mu$W/kg)	2.1	6.9	6.1	8.3	13.0	14.6	15.0	15.3	15.5
	$SAR_{wb,dmc}^{fdtd}(\mu$W/kg)	0	2.6	2.4	4.6	9.1	10.6	11.0	11.3	11.5
	% of the DMC in the SAR_{wb}^{fdtd}	0	37.7	39.0	55.1	69.8	72.7	73.4	73.9	74.1
	percentage error (ΔSAR) in %	659	133.3	162.0	94.0	23.8	10.3	7.0	4.9	4.0
Scenario 3	$SAR_{wb}^{fdtd}(\mu$W/kg)	0.4	3.2	2.8	4.5	8.0	9.2	9.5	9.7	9.8
	$SAR_{wb,dmc}^{fdtd}(\mu$W/kg)	0	2.0	1.8	3.5	6.9	8.1	8.4	8.6	8.7
	% of the DMC in the SAR$_{wb}^{fdtd}$	0	62.3	64.9	78.0	86.8	88.2	88.5	88.8	88.9
	percentage error (ΔSAR) in %	2505	211	251	121	24.4	8.0	4.2	1.8	0.7

Table 4.4: Simulated SAR_{wb} values for the different scenarios. The last row of each scenario represents the relative error between the experimental and numerical results

in Section 4.5.6). The second scenario corresponds to a separation of 6 meters between the Tx and the phantom, and the total power density is about 4.30 mW/m^2. The incident LOS power density is about 51% of the total power density while the diffuse fields represent the rest, i.e., 49% of the total power density. The experimental and simulated absorption rate values are 16.10 μW/kg and 15.50 μW/kg, respectively, leading to a relative error of about 4%. The third scenario corresponds to a separation of 10.20 meters of the phantom from the Tx, and the total incident power density is about 2 mW/m^2. The LOS power density represents 20% of the total power density whereas the diffuse fields represent 80%. Only a relative error of about 0.7% is obtained between the experimental absorption rate (9.90 μW/kg) and the simulated absorption rate (9.80 μW/kg).

It is important to mention that Tables 4.3 and 4.4 return a maximum relative error of about 5.1%, 5.0%, and 5.0%, respectively, for the three scenarios between the experimental and the simulated SAR$_{wb}$ induced by *only* the diffuse fields ($SAR_{wb}^{exp,dmc}$ in Table 4.3 and $SAR_{wb}^{fdtd,dmc}$ in Table 4.4).

4.5.6 Discussions

We presented an entirely new method for the experimental assessment of the SAR$_{wb}$ in a real indoor environment and validated it through numerical simulations. Excellent agreement is obtained for the far field conditions (scenario 2 and 3). In contrary to the scenario 2 and 3, no satisfactory agreement is obtained for the scenario 1. When assessing the SAR$_{wb}$ induced only by the diffuse fields (comparing both the experimental and numerical approach), it turns out that the presented method gives excellent agreement since a relative error of about 5 % is obtained regardless of the scenario. This indicates that the large error in scenario 1 is due to the LOS component. The reason could be the fact that the absorption cross section assessment due to a LOS component illumination is based on the plane-wave assumption. The plane-wave assumption is not ensured in the near field of the transmitter (scenario 1), especially when the receiver is not

an antenna, but a phantom with large dimensions. This may explain the difference between the experimental and the simulated results for the first scenario since the LOS component is dominant in that configuration. Here, the general method is presented for canonical models for validation purposes but it can be applied to any phantom. The method is applied to actual humans in Section 4.2.2. For the sake of averaging and simplification, we assumed in the methodology that the humans under test have a similar absorption cross section. When considering humans with different absorption cross section - which is more likely to occur in reality - the method can be applied in this way: *i)* perform the measurements for only one unknown subject in the room, or if there are other persons in the room their absorption cross section in diffuse fields should be known and *ii)* in addition, several measurement observations for each person have to be done - for averaging purposes - to accurately assess the absorption cross section.

A person's absorption cross section is proportional to its body surface, and hence, to its morphology. The body mass index (BMI) is a main characteristic of human's morphology. The human's morphology variability is addressed in [16], where the authors have shown that the BMI variability for six adult models (Visible Human, Norman, Korean, Zubal, Japan Male, and Japan Female) leads to a standard deviation of only 18%. Therefore, even though the morphology variability affects the whole-body SAR, our simple method will provide a reasonable value for the whole-body SAR_{wb} (not localized SAR) given the low variability caused by the human's morphology.

4.6   Conclusions

An experimental method to assess the whole-body specific absorption rate in indoor environments is proposed and validated through numerical simulations. The method is applicable for any phantom or human. Different scenarios have been investigated to ensure the validity of the method at different locations within the investigated room. Experimental and numerical results agree very well as long as the plane wave assumption is sufficiently met (not in the vicinity of the transmitter). The relative error between experimental and numerical results are 77.5%, 4.0%, and 0.70%, for the scenario 1, scenario 2, and scenario 3, which correspond respectively to a distance of 0.60 m, 6.0 m, and 10.20 m from the Tx.

The diffuse fields' contribution in the total whole-body specific absorption rate has been addressed as well. The SAR_{wb} decreases with increasing separation from the Tx. The larger the separation is, the larger the contribution of the diffuse fields in the induced SAR_{wb} will be, which may reach 90%.

The absorption cross section in diffuse fields was independent of the polarization since this latter is assumed to be random in a complete diffuse fields. However, the absorption cross section due to LOS exposure will be polarization dependent and this issue has not been addressed in this chapter.

When the method is applied to humans, it is assumed that they have identical absorption cross sections. This assumption might not be applicable in certain circumstances, for instance when children and adults are both in the room during the measurements. In Chapter 5, we will address the human's absorption cross section as a function of its characteristics, i.e., its height and mass.

References

[1] ICNIRP. "Guidelines for limiting exposure to time-varying electric, magnetic, and electromagnetic fields (up to 300 GHz)". *Health Physics*, 74 (4): pages 494–522, 1998.

[2] P. J. Dimbylow. "Fine resolution calculations of SAR in the human body for frequencies up to 3 GHz". *Phys. Med. Biol.*, 47: pages 2835–2846, 2002.

[3] J. Wang, O. Fujiwara, S. Kodera and S. Watanabe. "FDTD calculation of whole-body average SAR in adult and child models for frequencies from 30 MHz to 3 GHz". *Phys. Med. Biol.*, 51: pages 4119–4127, 2006.

[4] S. Kühn, W. Jennings, A. Christ and N. Kuster. "Assessment of induced radio-frequency electromagnetic fields in various anatomical human body models". *Phys. Med. Biol.*, 54 (2009): pages 875–890, 2009.

[5] J. F. Bakker, M. M. Paulides, A. Christ, N. Kuster, and G. C. van Rhoon. "Children and adults exposed to electromagnetic fields at the ICNIRP reference levels: theoretical assessment of the induced peak temperature increase". *Phys. Med. Biol.*, 56: pages 4967–4989, 2011.

[6] W. Joseph, L. Verloock, F. Goeminne, G. Vermeeren and L. Martens. In situ LTE Exposure of the General Public: Characterization and Extrapolation. *Bioelectromagnetics*, 33 (6): pages 466–475, 2012.

[7] G. Vermeeren, W. Joseph, C. Olivier, and L. Martens. "Statistical multipath exposure of a human in a realistic electromagnetic environment". *Health Physics*, 94, no. 4: pages 345–354, 2008.

[8] A. Bürgi, P. Frei, G. Theis, E. Mohler, C. Braun-Fahrlnder, J. Frhlich, G. Neubauer, M. Egger, M. Röösli. A model for radiofrequency electromagnetic field predictions at outdoor and indoor locations in the context of epidemiological research. *Bioelectromagnetics*, 33: pages 226–236, 2010.

[9] P. Bernardi, M. Cavagnaro, R. Cicchetti, S. Pisa, E. Piuzzi, O. Testa. A UTD/FDTD investigation on procedures to assess compliance of cellular base-station antennas with human exposure limits in a realistic urban environment. *IEEE Trans. Micro. Theory Techn.*, 51: pages 2409–2417, 2003.

[10] J. B. Andersen, J. Ø. Nielsen, G. F. Pedersen, G. Bauch, and M. Herdin. "Room Electromagnetics". *IEEE Antennas Propagat. Mag.*, 49, (2): pages 27–33, 2007.

[11] Bruce Hapke. "Theory of Reflectance and Emittance Spectroscopy". *Cambridge University Press*, 1993.

[12] O. Landron, M. J. Feuerstein, and T. S. Rappaport. "In Situ Microwave Reflection Coefficient Measurements for Smooth and Rough Exterior Wall Surfaces". In *43rd IEEE Vehicular Technology Conference, Secaucus, NJ, USA*, 1993.

[13] F. Delfino, P. Girdinio, L. Minervini, M. Nervi. "Electromagnetic plane wave scattering from building surfaces". *COMPEL - The international journal for computation and mathematics in electrical and electronic engineering*, 25 (4): pages 1007–1018, 2006.

[14] R. Piesiewicz, C. Jansen, D. Mittleman, T. Kleine-Ostmann, M. Koch, and T. Kürner. "Scattering Analysis for the Modeling of THz Communication Systems". *IEEE Trans. Antennas Propag.*, 55 (11): pages 3002–3009, 2007.

[15] A. Bamba, W. Joseph, J. B. Andersen, E. Tanghe, G. Vermeeren, D. Plets, J. O. Nielsen, and L. Martens. "Experimental Assessment of Specific Absorption Rate Using Room Electromagnetics". *IEEE Trans. Electromagn. Compat.*, 54 (4): pages 747–757, 2012.

[16] E. Conil, A. Hadjem, F. Lacroux, M. F. Wong and J. Wiart. "Variability analysis of SAR from 20 MHz to 2.4 GHz for different adult and child models using finite-difference time-domain". *Phys. Med. Biol.*, 53: pages 1511–1525, 2008.

[17] A. Hirata, Y. Nagaya, F. Osamu, T. Nagaoka, S. Watanabe. "Correlation between Absorption Cross Section and Body Surface Area of Human for Far-Field Exposure at GHz Bands". *Electromagnetic Compatibility, 2007. EMC 2007. IEEE International Symposium on*, pages 1–4, July 2007.

[18] W. Joseph and L. Martens. Comparison of Safety Distances Based on the Electromagnetic Field and Based on the SAR for Occupational Exposure of a 900-MHz Base Station Antenna. *IEEE Transactions on Electromagnetic Compatibility*, 47 (4): pages 977–985, 2005.

[19] F. W. Smith D. E. Merewether, R. Fisher. "On Implementing a Numeric Huygen's Source Scheme in a Finite Difference Program to Illustrate Scattering Bodies". *IEEE Trans. Nucl. Sci.*, 27 (6): pages 1829–1833, 1980.

[20] Harald T. Friis. A note on a Simple Transmission Formula. *Procedings of the I.R.E and Waves and Electrons*, pages pages 254–256, May, 1946.

[21] A. Taflove, S. Hagness. "Computational electrodynamics: The finite-difference time-domain method". *Artech. House, Norwood, MA, 3rd edition*, 2005.

[22] P. J. Chung, and J. F. Böhme. "DOA estimation using fast EM and SAGE algorithms". *Signals Processing*, 82: pages 1753–1762, 2002.

[23] A. Richter. *"Estimation of Radio Channel Parameters: Models and Algorithms"*. PhD thesis, Faculty of electrical Engineering and Information Technology at the Technical University. Ilmenau, Germany., 2005.

[24] N. Czink, A. Richter, E. Bonek, J. P. Nuutinen, J. Ylitalo. "Including Diffuse Multipath Parameters in MIMO Channel Models". In *IEEE 66th Vehicular Technology Conference (VTC)- Fall.*, 2007.

[25] J. B. Andersen, K. L. Chee, M. Jacob, G. F. Pedersen, T. Kürner. "Reverberation and Absorption in an Aircraft Cabin with the Impact of Passengers". *IEEE Trans. Antennas and Propag.*, 60 (5): pages 2472–2480, 2012.

[26] E. M. Vitucci, F. Mani, V. Degli-Esposti, and C. Oestges. "Dense Multipath Depolarization in Outdoor and Indoor Radio Transmissions ". In *31st URSI General Assembly and Scientific Symposium, Beijing, China*, 2014.

[27] Gerhard Steinbock, Troels Pedersen, Bernard Henri Fleury, Wei Wang, and Ronald Raulefs. Distance Dependent Model for the Delay Power Spectrum of In-room Channels. *IEEE Transactions on Antennas and Propagation*, 61 (8): pages 4327–4340, 2013.

[28] J. Poutanen, J. Salmi, K. Haneda, V. M. Kolmonen, and P. Vainikainen. "Angular and Shadowing Characteristics of Dense Multipath Components in Indoor Radio Channels". *IEEE Trans. Antennas Propag.*, 59: pages 245–253, 2011.

5

A Formula for human Average Whole-Body SAR Under Diffuse Fields Exposure in the GHz Region

5.1 Introduction

We have developed in the previous chapters a new measurement-based method to experimentally determine the SAR_{wb} of humans in realistic environments. Although the experimental method considers the contribution of both the DMC and LOS component, only particular directions and polarizations of the LOS component have been considered. The diffuse field is the part of the propagation data that can not be characterized with discrete planes waves [1–3]. The diffuse field is characterized by a continuous power density as function of azimuthal angle, time-delay, etc [2]. Therefore, the diffuse fields can not be recorded separately from field measurements. We have shown in Chapter 4 that the contribution of the diffuse fields to the total SAR_{wb} in realistic indoor environments may increase up to 90%, depending on the person's location in an indoor environment.

In Chapter 2, it is shown that the diffuse field has a stochastic nature (e.g., polarization and phase). Because of this stochastic nature, the numerical investigation of the SAR_{wb} due to diffuse fields would require excessive time and memory resources.

The SAR_{wb} depends on many parameters (posture, polarization of the incident plane wave, direction of the plane wave, human morphology, etc.) [4]. A variability study of the SAR_{wb} for different morphological phantoms can be found in [5]. [6] investigated the SAR_{wb} in child phantoms in a realistic environment in the MHz range. The authors showed that the worst-case incident plane-wave polarization depends on the ratio of the phantom size and the considered wavelength. This observation is confirmed in [7, 8], wherein it is stated that the polarization of the incident electric field may have an effect of several dB on the estimated SAR_{wb}.

The SAR_{wb} due to a vertically polarized plane-wave is higher than the one due to a horizontally polarized plane-wave up to the resonant frequency (order of 60-120 MHz), whereas the SAR_{wb} due to a horizontally polarized plane-wave becomes higher in the GHz region [8]. Moreover, the SAR_{wb} due to a single plane wave illumination depends on its direction of arrival. This is confirmed in [9] where it was shown that the SAR_{wb} varies periodically with the azimuth angle for the visible human (VH). This periodic behavior will occur for any other human phantom at the GHz frequencies since the physically illuminated body surface varies with the incident plane wave's azimuth.

Despite a large number of parameters involved in the SAR_{wb} and their complexities, [10] proposed a formula on the basis of the analogy of the human body and a half dipole antenna to determine the SAR_{wb} for plane wave exposure at the resonance frequency. The authors highlighted the impact of the tissues inhomogeneity on the estimated SAR_{wb} at the resonance frequency. The derived formula accounts for the proportion of fat in the human model as well. All those previous works investigated the human SAR_{wb} due to deterministic plane-wave illumination.

The human's absorption in the GHz region is mainly influenced by the body surface area (BSA). This is due to the absorption occurring at the body surface rather than inside the body volume because of the relative small penetration depth in the GHz region [3, 11]. Based on these observations, a BSA based formula to determine the SAR_{wb} caused by diffuse fields in the GHz region is addressed in this chapter. The objective of this chapter is to propose a simple formula (as an alternative to numerical and experimental approaches) with only the human mass and the incident power density as inputs to determine rapidly the average SAR_{wb} under realistic propagation conditions, i.e., **presence of diffuse fields**, and possibly a LOS component. The novelty of this work is that *i)* it proposes a formula whose parameters are independent of the human morphology to determine the SAR_{wb}, and *ii)* the formula includes the diffuse fields contribution to the human SAR_{wb} assessment up to 5-6 GHz. The theoretical background is based on an ellipsoid analysis, which is used to investigate the parameters involved in the proposed formula. For the LOS exposure, both vertical and horizontal polarization are investigated, and all azimuthal angles as well. Some parameters in the formula are frequency dependent and are characterized at GHz frequencies. Moreover, the proposed formula is validated using numerical simulations with several realistic 3D heterogeneous phantoms at 3 GHz.

The remainder of this chapter is organized as follows: In Section 5.2, the ellipsoidal and the anatomical phantoms are described. The simulation settings and the methodology are presented in Section 5.3. The formula to determine the total SAR_{wb} and the parameters involved are derived in Section 5.4. The formula is validated at 3 GHz in Section 5.5. Further discussions and analysis of these results can be found in Section 5.5. Finally, conclusions are drawn in Section 5.6.

5.2 Models

5.2.1 Ellipsoids

The complexity of the human morphology makes a geometrical investigation very difficult for the SAR_{wb} determination. Prolate spheroids models are often used as approximation of the human body [6]. The authors in that paper investigated the SAR_{wb} in the MHz region, where the dielectric properties influence more

the SAR$_{wb}$ than the BSA does. However, an ellipsoid model describes more accurately the human body characteristics in terms of the BSA [9] . Therefore, ellipsoids are more suitable as non-realistic phantoms for the determination of the SAR$_{wb}$, particularly in the GHz region. Four homogeneous ellipsoidal models of human bodies are used here to determine the main parameters in the SAR$_{wb}$ prediction equation, i.e., the average man, the average woman, the 10-year-old child, and the 5-year-old child. The mass (resp. height) of each ellipsoid coincides with the mass (resp. height) of the corresponding human. A picture of the tri-axial ellipsoid model is shown in Fig. 5.1. The three axes are denoted as a, b, and c with $a \geq b \geq c$.
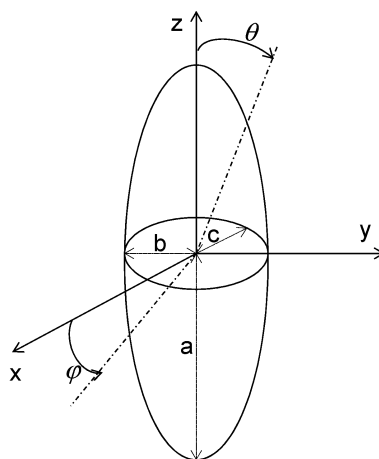
Figure 5.1: An ellipsoid model for human body approximation. a, b and c are the ellipsoids axes. φ and θ represent the azimuth and the elevation, respectively

The parameters of the ellipsoids, i.e., the height, long axis, and small axis are summarized in Table 5.1 and are retrieved from [12]. The dielectric properties (conductivity σ and relative permittivity ϵ_r) of equiv-

Phantoms	Average mass (kg)	Height, $2a$ (m)	Long axis, $2b$ (m)	Small axis, $2c$ (m)
Average man	70.00	2×0.875	2×0.195	2×0.098
Average woman	61.14	2×0.805	2×0.200	2×0.091
10-year-old child	32.20	2×0.69	2×0.143	2×0.078
5-year-old child	19.50	2×0.56	2×0.120	2×0.069

Table 5.1: Characteristics of the ellipsoids used as human phantoms

alent head tissue recommended by the IEEE SCC-34/SC-2 [13] are used to simulate the human tissues properties in the homogeneous phantoms. Their values for different frequencies in the GHz region are listed in Table 5.2.

85

Frequency (MHz)	Head tissue properties	
	ϵ_r	σ (S/m)
1450	40.50	1.20
1610	40.30	1.29
1800 - 2000	40.00	1.40
2450	39.20	1.80
3000	38.50	2.40
5800	35.30	5.27

Table 5.2: Head tissue dielectric parameters used for the analysis [13]

5.2.2 Anatomical phantoms

Four 3D heterogeneous human models are used to validate the theory developed with the ellipsoids analysis. The four anatomical phantoms are the virtual family models comprised of a 34-year-old male, 26-year-old female, 11-year-old girl, and 6-year-old boy, denoted respectively as Duke, Ella, Billie, and Thelonious. Each model contains more than 75 different types of tissues and organs [14].

(a) Duke (34-year-old male) (b) Ella (26-year-old female) (c) Billie (11-year-old girl) (d) Thelonious (6-year-old boy)
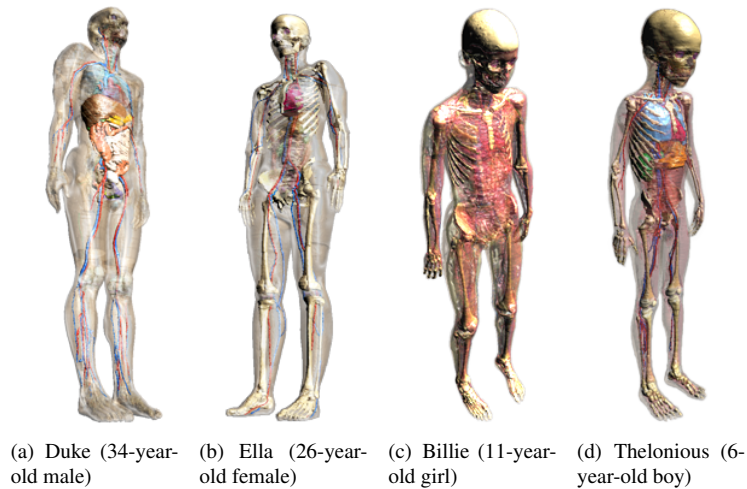
Figure 5.2: Various considered 3D heterogeneous human models

A picture of the virtual family is shown in Fig. 5.2, and only represent the upright posture. Hence, only this position is investigated in this study.

5.3   Settings and methodology

5.3.1   Simulation settings

The FDTD method [15] is used to numerically compute the SAR_{wb} in the homogeneous ellipsoids and in the heterogeneous human models. As previously, a harmonic excitation and a rectangular plane-wave source based on the TFSF technique are used in the simulations [16]. The maximum grid step in the phantoms is set to $0.07\lambda_{ph}$, where λ_{ph} is the wavelength inside a tissue. An UPML is used as boundary condition to avoid the reflections of the waves impinging on the boundaries of the simulation domain. The UPML was set so that more than 95% of the incident plane-wave power is absorbed by the boundary layers.

5.3.2   Methodology

When assessing experimentally the SAR_{wb} in Chapter 3, one of the challenging issues was the determination of the ACS under a LOS illumination (ACS_{los}). We assumed in Chapter 3 a frontal illumination ($\varphi=0$) or a back illumination ($\varphi=\pm\pi$) of humans to approximate the ACS_{los} as half of the ACS obtained in diffuse fields ($ACS_{wb,dmc}$). In general, and for a given azimuth, the ACS for a LOS illumination can be expressed as:

$$ACS_{los}(\varphi) = k(\varphi) \times ACS_{wb,dmc} \qquad \text{with } 0 < k < 1, \tag{5.1}$$

where $ACS_{wb,dmc}$ is the whole-body ACS in diffuse fields, i.e., accounting for all the azimuthal, therefore independent of the azimuth. In (5.1), we assume the LOS illumination is in the horizontal plane so that the ACS_{los} depends only on the azimuthal angle. The ACS_{los} can be determined for a given incident angle via numerical simulations. However, the $ACS_{wb,dmc}$ - determined from diffuse exposure - can *not* be determined exactly via numerical simulations because *i)* it is stochastic by nature and *ii)* the modeling and properties of the DMC in the simulation software will be an approximation of what actually occurs in real environments. Therefore, the ACS in diffuse fields is investigated from the ellipsoid analysis, and then related to the ACS_{los} via the parameter k.

The SAR is the absorbed power by a human per unit of mass (W/kg). Therefore, the SAR_{wb} can be expressed as:

$$SAR_{wb} = \frac{P_{abs}}{m} \tag{5.2a}$$

$$= \frac{I \times ACS}{m} \tag{5.2b}$$

where P_{abs}, m, I, and ACS are the absorbed power by the human (W), the person's mass (kg), the incident power density (W/m^2), and the person's absorption cross section (m^2), respectively.

The ACS stems from the interaction between a surface area and an incident plane wave. Therefore, the ACS can be defined as the projected surface *on a plane* perpendicular to the direction of the incident plane wave and then scaled by an efficiency factor. The efficiency factor can be thought of as the percentage of the power absorbed by the surface [17], or as an absorption probability [18]. All the wave's interactions with surfaces are included in the efficiency factor. The human $ACS_{wb,dmc}$ can be defined as the sum of

the different projected human body surfaces from all azimuthal angles, and then be scaled with the average fraction of the power absorbed by the human:

$$ACS_{wb,dmc} = \eta \times \int_0^{2\pi} BSA_{pr}(\varphi)d\varphi$$
$$= \eta \times BSA_{pr}^T \tag{5.3}$$

where η, $BSA_{pr}(\varphi)$, and BSA_{pr}^T are the average fraction of the incident power being absorbed, the projected surface of the human body in the φ-direction, and the total projected body surface area of the human, which accounts for all the azimuthal angles. Since η is an average value, it is independent of the incoming wave's direction of incidence.

Now, we determine the surface of the ellipsoid of Fig. 5.1. Its projection on a plane perpendicular to the frontal direction (x-axis, i.e., $\varphi = 0$ and $z = 0$) is an ellipse whose long and small axis are $2a$ and $2b$, respectively. The surface area of that ellipse is $S_F = \pi \times a \times b$. Similarly, the area of the projected ellipsoid on a plane from a side view (y-axis, i.e., $\varphi = \pm\pi/2$ and $z = 0$) is $S_S = \pi \times a \times c$. If the projection of the ellipsoid is done on any plane between the front and a side view ($0 < |\varphi| < \pi/2$ and $z = 0$), the resulting surface is an ellipse whose long and small axis are $2a$ and h, respectively. h is the hypotenuse of the triangle whose perpendicular sides are $2bcos(\varphi)$ and $2csin(\varphi)$. The area of that surface is denoted as S_φ, and is given as follows:

$$S_\varphi = \pi a \frac{h}{2}$$
$$= \pi \frac{a}{2}\sqrt{(2b\cos(\varphi))^2 + (2c\sin(\varphi))^2}$$
$$= \sqrt{S_F^2 \cos^2(\varphi) + S_S^2 \sin^2(\varphi)} \tag{5.4}$$

Equation (5.4) shows that the surface of the projected ellipsoid from any azimuth can be described with the frontal and side projected surfaces, i.e., S_F and S_S, respectively. Analogously with (5.4), the ACS at any azimuth, i.e., ACS(φ), can be expressed as a function of the frontal and side absorption cross section, denoted as ACS$_F$ and ACS$_S$, respectively.

$$ACS(\varphi) = \sqrt{ACS_F^2 \cos^2(\varphi) + ACS_S^2 \sin^2(\varphi)} \tag{5.5}$$

The frontal (ACS_F) and side (ACS_S) absorption cross section can be easily determined via FDTD numerical simulations and using (5.2b).

Before we derive the formula for the SAR$_{wb}$, an important property (or assumption) of the diffuse fields has to be recalled. It is assumed that the electromagnetic waves composing the diffuse fields cannot interfere with each other. Therefore, their energies or intensities can be summed regardless of mutual phase relations. This assumption is made for the acoustic case as well [18]. The applicability of the acoustic diffuse sounds properties to the electromagnetic diffuse fields is demonstrated in [17].

Under this hypothesis, the diffuse absorption cross section, which is our main concern here is expressed as

follows:

$$ACS_{wb,dmc} = \int_0^{2\pi} ACS(\varphi)d\varphi \tag{5.6}$$

Note that only the horizontal elevation is considered for simplicity purposes. The expression in (5.6) is a $\frac{\pi}{2}$-periodic function. Substituting (5.5) in (5.6), the $ACS_{wb,dmc}$ can be re-written as follows:

$$ACS_{wb,dmc} = 4 \int_0^{\frac{\pi}{2}} \sqrt{ACS_F^2 \cos^2(\varphi) + ACS_S^2 \sin^2(\varphi)}d\varphi$$
$$= 4ACS_F \int_0^{\frac{\pi}{2}} \sqrt{1 - m^2 \sin^2(\varphi)}d\varphi, \tag{5.7}$$

where the integral in (5.7) is the complete elliptic integral of second order with the parameter m defined as:

$$m = \sqrt{\frac{ACS_F^2 - ACS_S^2}{ACS_F^2}}, \quad 0<m<1$$

Equation (5.7) is further used to determine the η parameter via (5.3).

If one would model the total diffuse field with a single plane wave, a polarization matching factor of 0.5 would be assumed, which corresponds to a polarization angle of 45°. For instance, this assumption is made in [19]. Moreover, this has been experimentally confirmed through an analysis of the polarization angles of diffuse fields in a RC (Section 2.3.4 of Chapter 2). Both ACS_F and ACS_S are numerically determined with a plane wave incident to the front and to a side, respectively, with a polarization angle of 45°. This means that ACS_F and ACS_S are both obtained for η averaged over the polarization cases. Therefore, the resulting $ACS_{wb,dmc}$ value is obtained (with ACS_F and ACS_S) for an averaged η, and is independent of a particular polarization. Due to the symmetry of the ellipsoid, the same results would have been obtained if a polarization of $\pm 135^\circ$ or -45° had been assumed.

Finally, for the LOS component, the SAR_{wb} depends on the incident plane wave azimuth, polarization, considered frequency [4, 8]. By analyzing (5.2a) and (5.2b), it is clear that the resulting ACS_{los} will depend on the parameters mentioned above. The idea is to gather all these dependencies in a limited number of parameters, i.e., η, and k. Once these parameters are characterized for a given posture, polarization, direction, and frequency range, the ACS_{los} and $ACS_{wb,dmc}$ can thus be linked to the BSA.

5.4 Formula for human whole-body averaged SAR

5.4.1 Determination of the parameters for the ellipsoid model

This section is devoted to the determination - through FDTD numerical simulations - of the parameters k and η expressed in (5.1) and (5.3), respectively, for frequencies ranging from 1450 MHz to 5800 MHz. These frequencies span a frequency range from the Global System for Mobile Communications (GSM) 1800 band up to the Wireless Local Area Network (WLAN) frequencies. At each frequency, the ellipsoidal models are assigned with the appropriated dielectric properties listed in Table 5.2. The incident plane-wave power density is set to 1 W/m^2 in all the simulations.

Validation of the ACS as a function of the azimuthal angle

The ACS expression of (5.5) at any azimuth is validated here. All the plane waves are incident in the transverse plane. The azimuth angle is varied with a step of $15°$, and both vertical and horizontal polarizations are addressed. Table 5.3 compares the theoretical ACS ($\text{ACS}_{los,th}$) obtained from (5.5) with the simulated ACS ($\text{ACS}_{los,sim}$) obtained from (5.2b) for azimuthal angles ranging from 0 to $\pi/2$ (symmetry of the ellipsoid) for the ellipsoids of Fig. 5.1. The trend is the same for the other phantoms. The maximum

		φ (°)	0	15	30	45	60	75	90
Average man	Vert. pol.	$\text{ACS}_{los,sim}$ (cm^2)	1198	1160	1051	893	734	616	571
		$\text{ACS}_{los,th}$ (cm^2)	1198	1167	1076	938	777	633	571
		δACS (%)	0	0.6	2.3	5	5.8	2.7	0
	Hor. pol.	$\text{ACS}_{los,sim}$ (cm^2)	1417	1413	1392	1343	1276	1213	1182
		$\text{ACS}_{los,th}$ (cm^2)	1417	1403	1362	1305	1245	1200	1182
		δACS (%)	0	0.7	2.1	2.8	2.4	1	0
Average woman	Vert. pol.	$\text{ACS}_{los,sim}$ (cm^2)	1144	1104	991	828	663	542	497
		$\text{ACS}_{los,th}$ (cm^2)	1144	1112	1021	882	716	564	497
		δACS (%)	0	0.7	3	6.5	8	4	0
	Hor. pol.	$\text{ACS}_{los,sim}$ (cm^2)	1318	1313	1292	1244	1173	1103	1066
		$\text{ACS}_{los,th}$ (cm^2)	1318	1303	1260	1199	1134	1084	1066
		δACS (%)	0	0.8	2.5	3.6	3.3	1.7	0
10-year-old	Vert. pol.	$\text{ACS}_{los,sim}$ (cm^2)	720	700	640	557	474	413	390
		$\text{ACS}_{los,th}$ (cm^2)	720	703	653	579	494	420	390
		δACS (%)	0	0.4	2	4	4.2	1.7	0
	Hor. pol.	$\text{ACS}_{los,sim}$ (cm^2)	853	850	838	813	778	743	729
		$\text{ACS}_{los,th}$ (cm^2)	853	846	824	794	762	738	729
		δACS (%)	0	0.5	1.7	2.3	2	0.7	0
5-year-old	Vert. pol.	$\text{ACS}_{los,sim}$ (cm^2)	503	491	454	402	349	309	294
		$\text{ACS}_{los,th}$ (cm^2)	503	492	460	412	358	313	294
		δACS (%)	0	0.2	1.3	2.5	2.6	1.3	0
	Hor. pol.	$\text{ACS}_{los,sim}$ (cm^2)	595	593	584	568	547	526	516
		$\text{ACS}_{los,th}$ (cm^2)	595	590	577	557	537	522	516
		δACS (%)	0	0.5	1.2	1.9	1.8	0.7	0

Table 5.3: Simulated ($\text{ACS}_{los,sim}$) and calculated ($\text{ACS}_{los,th}$) absorption cross sections for the ellipsoid of Table 5.1. Both vertical and horizontal polarization at different azimuth angles are considered in the transverse plane

relative error (δACS) for all the ellipsoids is about 8%, and this is obtained for the average woman, whereas the minimum relative error approaches 2% for the 5-year-old child ellipsoid model. In general, the relative errors obtained between the predicted ACS with (5.2b) and the simulated values are small enough to be neglected. Therefore, (5.7) can be used to determine the $\text{ACS}_{wb,dmc}$ of the ellipsoids in order to further derive η.

Determination of η

Let us recall that η is the ratio of $\mathrm{ACS}_{wb,dmc}$ to the total projected body surface area (BSA_{pr}^{T}). The $\mathrm{ACS}_{wb,dmc}$ of an ellipsoid is determined with (5.7) and only two simulations (computation of ACS_{F} and ACS_{S}). The projected surface area of the tri-axial ellipsoid can be found by integrating (5.4) from 0 to 2π, which leads to a similar expression as (5.7). The $\mathrm{ACS}_{wb,dmc}$ is determined for all the investigated frequencies while the BSA_{pr}^{T} is frequency independent. For each frequency, four η values - one value per phantom - are obtained, which are then averaged over the phantoms to obtain one η value per frequency. It turns out that η is approximately phantom independent at a given frequency since the maximum relative standard deviation is about 6% and this occurs at 5800 MHz. The average values of η as a function of the frequency are shown in Fig. 5.3.
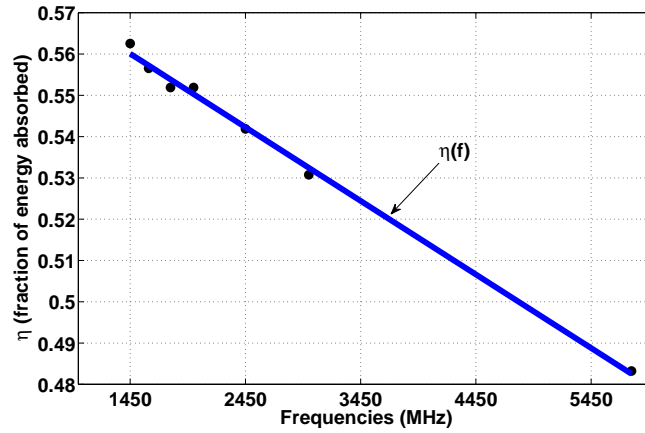
Figure 5.3: η as a function of frequency

A linear regression is applied to the data of Fig. 5.3, and η can be expressed as a function of the frequency:

$$\eta(f) = -1.7827 \times 10^{-5} \times f + 0.5859, \qquad R^2 = 0.9981 \tag{5.8}$$

where f is the frequency in MHz, and R^2 is the coefficient of goodness. Note that (5.8) is only valid for the investigated frequency band.

Determination of k

The next parameter to investigate is the ratio k between the ACS_{los} and $\mathrm{ACS}_{wb,dmc}$. This parameter is needed to determine the SAR_{wb} due to a LOS exposure at a certain azimuth. The ACS_{los} depends obviously on the incident wave polarization ψ and azimuth φ. Therefore, k is expressed as follows:

$$k(\varphi, \psi) = \frac{ACS_{los}(\varphi, \psi)}{ACS_{wb,dmc}} \tag{5.9}$$

91

k is investigated for the vertical and horizontal polarization using the four ellipsoids whose characteristics are shown in Table 5.1. The azimuthal angle is varied from 0 to 90° with a step of 15°. We limit the azimuth variation to one quadrant because of the ellipsoid's symmetry in the azimuthal domain. For a given frequency and azimuthal angle, k is averaged over the four phantoms. A frequency averaging is also done for each azimuthal angle. For all the investigated frequencies and azimuths, a maximum relative standard deviation of about 3% (φ=90°, frequency=2450 MHz) and 1.5% (φ=0°, frequency=1450 MHz) is obtained for the vertical and horizontal polarization, respectively. Therefore, k is considered as phantom independent. This is obvious as both the ACS_{los} and $\text{ACS}_{wb,dmc}$ are dependent on the frequency via the average fraction of absorbed energy.

Fig. 5.4 shows the mean value of k for the vertical and horizontal polarization, i.e., k_V and k_H, respectively.
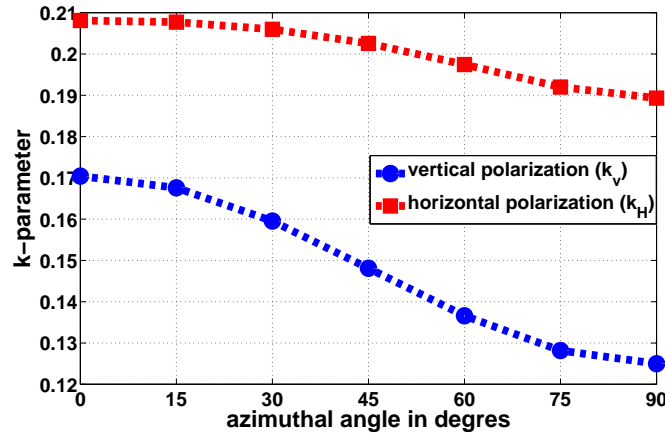
Figure 5.4: k (averaged over the phantoms and the frequencies). k_V (resp. k_H) is the ratio between the ACS from a vertically (horizontally) polarized LOS and the DMC

It is observed that k_H (k value for the horizontal polarization) is always - as a function of the azimuth - higher than k_V (k value for the vertical polarization). This is an expected result since the SAR_{wb} from a horizontally polarized plane wave is higher than the one from a vertically polarized plane wave in the GHz region [8]. Given the low relative standard deviations, k is thus considered as phantom and frequency independent. The value of k for any other polarization ψ at a given azimuth φ is determined from k_V and k_H:

$$k(\varphi, \psi) = k_V(\varphi) \times \cos^2(\psi) + k_H(\varphi) \times \sin^2(\psi) \tag{5.10}$$

5.4.2 Determination of the parameters for the realistic human models

The $\text{ACS}_{wb,dmc}$ is calculated with the knowledge of the phantom's total projected BSA (BSA_{pr}^T) and the η, (see 5.3). However, a human BSA is very complex, depending mainly on its height and mass. Several works [20–22] have investigated the human BSA and modeled it using both the human height and mass. All these models determine accurately the human's BSA, but they are unnecessary complex and in addition they

are inaccurate for obese people [23]. Actually, the BSA of a human can be determined with its mass as sole input and the resulting formula yields a better estimation of the BSA for both normal and obese people [23]. According to [23], a human's BSA is expressed as follws:

$$BSA = 0.1173 \times m^{0.6466}, \ \ \text{m} \geq 10 \, \text{kg} \tag{5.11}$$

where BSA is the human's body surface area in m^2 and m stands for the mass in kg. This formula was derived from patients weighting from 51.3 kg to 248.6 kg (their heights range from 152 cm to 182 cm). Child models were thus not included in their study. Moreover, (5.11) was derived based on a geometric method along with body size scaling principles. The surface area of a body segment (e.g., arm, hand, leg, thigh, etc.) is estimated by multiplying its circumference by its length and by a factor correcting for the shape. The formula (5.11) is very important for our study since this is the basis equation. Therefore, we investigated its correctness via numerical simulations and adapted it if necessary.

Numerical determination of the body surface area and total projected body surface area of heterogeneous phantoms

One can determine numerically the BSA (BSA$_{num}$) of a phantom in the simulation platform SEMCAD-X. This is achieved by discretizing the phantom with a certain uniform grid (i.e., *voxeling*), and by taking the sum of the surfaces of the voxels adjacent to the air. For this calculation, a grid step of 5 mm was chosen. The procedure to determine numerically the heterogeneous phantom BSA is explained in appendix A.1. Table 5.4 compares the BSA values of the heterogeneous phantoms determined with (5.11) and those determined numerically (BSA$_{num}$). The results of the numerical simulations in Table 5.4 show that (5.11) overestimates

Phantom	Thelonious	Billie	Ella	Duke
BSA$_{num}$ (m^2)	0.640	0.976	1.350	1.570
BSA (m^2)	0.798	1.180	1.622	1.878
BSA/BSA$_{num}$	1.24	1.21	1.20	1.20

Table 5.4: Ratio between the body surface area values, i.e., one determine numerically and the other determine with (5.11)

the BSA of all the human phantoms. The overestimation is constant for all the phantoms and is about 20%, indicating that (5.11) approximates well the human BSA. If we correct this formula for the 20% overestimation, this will also yield a better estimation of the absorption. The body surface area estimation is then as follows:

$$BSA = 0.097 \times m^{0.6466}, \ \ m \geq 10 \, \text{kg} \tag{5.12}$$

which agrees excellently with the numerical results. This formula determines accurately the BSA of any human based solely on its mass.

The BSA is used to calculate the ACS$_{wb,dmc}$ of heterogeneous humans via η. To calculate ACS$_{wb,dmc}$, the total projected BSA needs to be determined (i.e., BSA$_{pr}^{T}$, see (5.3)). Therefore, the BSA expressed in

(5.12) needs to be scaled with a coefficient to obtain the BSA_{pr}^{T}, assuming that both quantities have the same ratio for all the phantoms. Similarly to the BSA case, the BSA_{pr}^{T} of the heterogeneous phantoms is here determined using numerical simulations. The procedure is described in appendix A.2. Table 5.5 shows the numerical values of the BSA and the BSA_{pr}^{T} for the four heterogeneous phantoms, along with their respective ratio. The average ratio is about 2.20 with a standard deviation of only 2.70%. This ratio should be used

Phantom	Thelonious	Billie	Ella	Duke
BSA_{num} (m^2)	0.64	0.98	1.35	1.57
$\text{BSA}_{num,pr}^{T}$ (m^2)	1.45	2.17	2.90	3.35
$\text{BSA}_{num,pr}^{T}/\text{BSA}_{num}$	2.265	2.22	2.15	2.14

Table 5.5: Numerical body surface area and total projected body surface area with their respective ratio

to obtain the BSA_{pr}^{T} from the BSA calculated with (5.12).

A person is assumed to be exposed to both a LOS plane-wave and diffuse fields in a realistic indoor environment, according to the room electromagnetics theory [17, 19] and measurements presented in this thesis. The SAR_{wb} due to a LOS plane-wave illumination is obtained using (5.2b), (5.3), (5.9), (5.12), and by accounting for the ratio - between the BSA_{pr}^{T} and the BSA - determined in Table 5.5:

$$SAR_{wb,los}(\varphi,\psi) = 0.21 \times m^{-0.3534} \times \eta \times k(\varphi,\psi) \times I_{los} \qquad \text{m} \geq 10\,\text{kg} \qquad (5.13)$$

where I_{los} is the incident power density of the LOS component.

In indoor environments, the SAR_{wb} due to diffuse fields is stochastic since the propagation of the diffuse fields is stochastic [24]. For the average SAR_{wb} due to diffuse fields, we use the same equations as above:

$$SAR_{wb,dmc}^{avg} = 0.21 \times m^{-0.3534} \times \eta \times I_{dmc} \qquad \text{m} \geq 10\,\text{kg} \qquad (5.14)$$

Since k, η, and the power densities are known, the human absorption rate due to a LOS plane wave and/or the diffuse fields is easily calculated if the human's mass is known.

5.5 Validation of the SAR$_{wb}$ formula

The proposed formulas i.e., (5.13) and (5.14), are validated through numerical simulations at the frequency of 3 GHz. The formulas are applied to the 3D heterogeneous human models shown in Fig. 5.2 and are compared to the SAR_{wb} values obtained from FDTD numerical simulations. The SAR_{wb} due to the LOS component and diffuse fields are validated separately. The stochastic properties of the diffuse fields defined in Section 2.3.4 of Chapter 2 are applied here. The total incident power density is set to 1 W/m^2.

5.5.1 SAR$_{wb}$ values from LOS plane wave exposure

The $\text{SAR}_{wb}(\varphi,\psi)$ due to a LOS plane wave with azimuth φ and polarization ψ is expressed in (5.13). The theoretical $\text{SAR}_{wb,los}^{th}$ determined with (5.13) and the simulated $\text{SAR}_{wb,los}^{sim}$ from the numerical simulations

for the 26-year-old female (Ella) are shown in Fig. 5.5. In accordance with the literature [7, 8] and simulated values, the developed method shows that the SAR$_{wb,los}$ induced by a horizontally polarized plane wave is always - with respect to the azimuth - higher than the SAR$_{wb,los}$ induced by a vertically polarized plane wave (see Fig. 5.5(a)). We also notice that the SAR$_{wb,los}$ is more sensitive to the azimuth when the incident LOS plane wave is vertically polarized. This is explained by the ability of a horizontally polarized E-field to propagate better around the body [8], i.e., the incoming azimuth does not have as large an effect on the SAR as for vertical polarization. Analogue conclusions can be drawn for the other members of the virtual family.
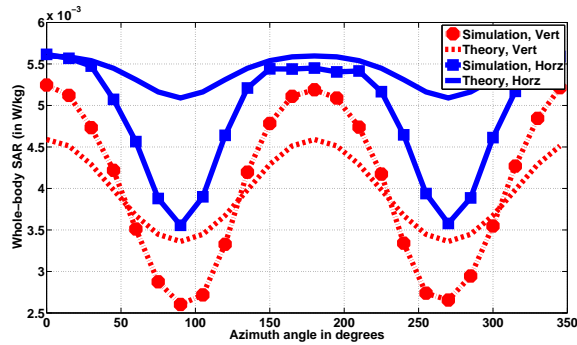
(a) SAR$_{wb}$ values
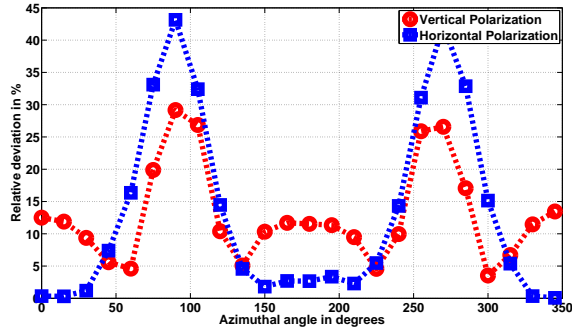
(b) Relative error of the SAR$_{wb}$ with respect to simulations

Figure 5.5: Theoretical versus simulated SAR$_{wb,los}$ and the relative error for phantom Ella

Table 5.6 summarizes the performance (i.e., accuracy) of the formula applied to the other members of the virtual family. The mean absolute relative error (δSAR$_{mean}$) varies from 28% to 12% (resp. 14% to 12%) for the vertical (resp. horizontal) polarization. The child models (Thelonious and Billie) exhibit in general the highest relative errors when the wave is incident to the front and/or the back ($\varphi \approx 0°$ and/or $180°$); whereas the lowest errors are obtained when the wave is incident to a side ($\varphi \approx 90°$ or $270°$). Regarding the adult models (Ella and Duke), it is interesting to see that the lowest errors occur for the worst case exposure,

Phantom	Thelonious		Billie		Ella		Duke	
Polarization	Vert.	Horiz.	Vert.	Horiz.	Vert.	Horiz.	Vert.	Horiz.
$\delta\mathrm{SAR}_{max}$ (%)	39.80	25.30	30.30	19.40	29.20	43.10	36.10	40.40
$\delta\mathrm{SAR}_{min}$ (%)	13.00	0.10	3.00	2.00	3.50	0	2.40	1.20
$\delta\mathrm{SAR}_{mean}$ (%)	28.70	14.30	19.40	12.30	12.90	13.00	14.00	14.60

Table 5.6: Relative error between the formula based $\mathrm{SAR}_{wb,los}$ and the simulation based $\mathrm{SAR}_{wb,los}$. $\delta\mathrm{SAR}$ is the relative error between the simulated and predicted values. The subscript *max*, *min* and *mean* designate the maximum, minimum, and average value, respectively

i.e., a horizontally polarized wave with frontal or dorsal incidence.

In general, the accuracy - in terms of relative error - of the proposed formula varies with the phantom's mass as well. It is important to notice that the numerical SAR_{wb} values may vary due to small changes in the modeling of parameters such as the model discretization, absorbing boundaries conditions, tissues properties, etc. A sensitivity study in [25] shows that the uncertainty on the simulated SAR_{wb} may reach $\pm21\%$. Keeping these uncertainties in mind, the proposed formula yields a good estimation of the SAR_{wb} due to a single plane wave. Moreover, the accuracy of the estimation improves as the human mass increases.

5.5.2 Averaged $\mathrm{SAR}_{wb,dmc}$ due to diffuse fields

As mentioned before, the whole-body SAR_{wb} due to diffuse fields is addressed in a statistical way. The stochastic approach of the diffuse fields has been widely accepted in the literature [24, 26–29]. A statistical multipath exposure tool is developed in [30] - which is based on FDTD simulations - to determine the average whole-body SAR_{wb} in realistic environments. We use this statistical multipath exposure tool as in chapter 2 to validate the $\mathrm{SAR}_{wb,dmc}^{avg}$ due to the diffuse fields and calculated with (5.14). The statistical multipath tool requires a minimum of 4000 samples to obtain statistically relevant values.

In our modeling, each sample is comprised of 432 plane waves (72 in the azimuthal plane and 6 in the elevation plane) representing the diffuse field. Let us now define the properties of the diffuse fields within a sample. For each sample, the total power density is divided by the number of plane waves such that each plane has the same amplitude (isotropic scattering). We have shown in Section 2.3.4 that the polarization angle ψ of the electromagnetic field in diffuse fields is normally distributed around $\psi_{mean} = \frac{\pi}{4}$. The standard deviation is so small that the polarization angles of the E-field in diffuse fields can be modeled with ψ_{mean}. Other approaches to model the polarization (e.g., uniform distribution) are used in literature but we follow this approach as motivated in Section 2.3.4.

The phase of each plane wave in a sample is randomly chosen with equal probability in [0 π[, i.e., according to an uniform distribution. Details on the diffuse fields modeling can be found in Section 2.3.4 of Chapter 2. Regarding the modeling in the space domain, adjacent plane waves are separated by $\Delta\varphi$=5° in the azimuthal plane and by $\Delta\theta$=30° in the elevation plane.

The output of the statistical tool is the cumulative distribution function (cdf) of the $\mathrm{SAR}_{wb,dmc}$. Fig. 5.6 shows the cdf of the $\mathrm{SAR}_{wb,dmc}$ for numerical simulations for the virtual family. Since we are mainly interested in the average value, we summarize those values in Table 5.7, along with the average values
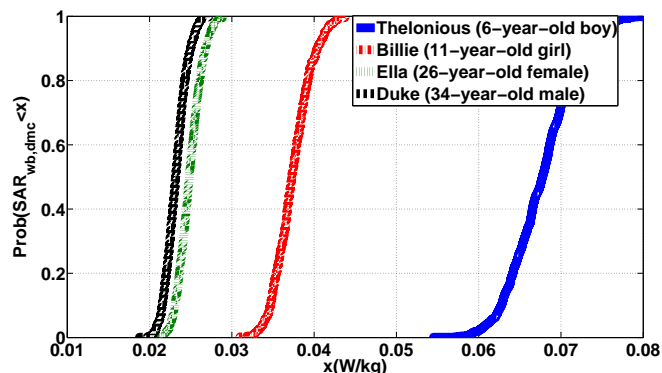
Figure 5.6: Cumulative distribution function of the SAR due to diffuse fields for the virtual family

obtained from the developed formula and the relative error δ_{SAR}.

Table 5.7 indicates that the SAR_{wb} induced by diffuse fields is much larger than the one induced by the LOS

	Thelonious	Billie	Ella	Duke
$\mathrm{SAR}^{formula}_{wb,dmc}$ (mW/kg)	41	33	27.60	25.70
$\mathrm{SAR}^{tool}_{wb,dmc}$ (mW/kg)	67.70	37.40	24.90	23.20
δ_{SAR} (%)	-39.40	-11.70	10.70	10.60

Table 5.7: Whole-body SAR_{wb} values from diffuse fields. Comparison of the proposed formula ($\mathrm{SAR}^{formula}_{wb,dmc}$) versus the statistical tool ($\mathrm{SAR}^{tool}_{wb,dmc}$)

component (e.g., see Fig. 5.5(a) for Ella). For the $\mathrm{SAR}_{wb,dmc}$, a maximum relative error of about -39.40% is obtained, and this occurs for Thelonious. A relative error of about -11.70%, 10.70%, and 10.60% is obtained for Billie, Ella, and Duke, respectively, indicating good agreement with the statistical tool. Note that the proposed formula underestimates the SAR_{wb} for the child models while it overestimates the SAR_{wb} for the adult models. However, a general satisfactory agreement is obtained, especially for the adults, indicating that the formula can be used to assess the average absorption due to diffuse fields in humans.

5.6 Conclusions

A simple expression to determine the human SAR_{wb} under realistic conditions in the GHz region is proposed. The propagation model is based on the room electromagnetics model, i.e., existence of diffuse scattered fields and a possible LOS component. For an incident plane wave, both vertical and horizontal polarization are considered and the method can easily be extended to other polarizations. The formula accounts for the exposure due to diffuse fields, which may be prominent in realistic indoor environments. The strength of the formula resides in its simplicity because only the human's mass and the incident power densities are

needed. The proposed formula to determine human's SAR_{wb} has been validated with FDTD numerical simulations at 3 GHz, and good agreement is obtained. The formula approximates human's SAR_{wb} caused by a LOS exposure with average relative errors varying from 28% to 12% (resp. 14% to 12%) for the vertical (resp. horizontal) polarization, depending on the human model. For the diffuse fields, relative errors of -39.40%, -11.70%, 10.70%, and 10.60% are obtained for the 6-year-old boy (Thelonious), 11-year-old girl (Billie), 26-year-old female (Ella), and 34-year-old male (Duke), respectively. It is observed that the accuracy of the proposed model improves when the human's mass increases.

<div align="right">

A

</div>

<div align="right">

Appendices

</div>

A.1 Numerical determination of the body surface area (BSA) of heterogeneous phantoms

The procedure to determine numerically the body surface area of the heterogeneous phantoms is presented here. Consider a certain phantom (Thelonious for instance) located in a rectangular parallelepiped limiting the simulation domain. The rectangular cuboid is discretized with a uniform grid size h. The discretization is performed with SEMCAD-X. After the discretization, each cube or voxel contains either a certain human tissue or the air surrounding the phantom indicated by an index. Fig. A.1 shows the cross section of the discretized rectangular cuboid for a certain height z_k, k={1, ..., k_{max}}, where k_{max} is the number of voxels along the z-axis. z_k is the discrete height defining a cross section plane. Since Fig. A.1 is in 2D, we use now the term pixel instead of voxel. In Fig. A.1, a white pixel designates the air surrounding the phantom while a green pixel indicates a certain human tissue. Part 1, Part 2, and Part 3 in Fig. A.1 are the discretized right arm, trunk, and left arm, respectively. This means that the considered cross section of Fig. A.1 is somewhere between Thelonious' hip and chest.

For a given height z_k, the BSA is the sum of the surfaces of the pixels adjacent to the air. Those pixels are indicated with a red cross in Fig. A.1. Therefore, the BSA is obtained by summing all the surfaces of the adjacent pixels to the air, and for all z_k.

$$
\begin{aligned}
BSA \quad &= \textstyle\sum_{z_k} N_p^a(z_k) \times h^2 & \text{(A.1)} \\
&= h^2 \times \textstyle\sum_{z_k} N_p^a & \text{(A.2)}
\end{aligned}
$$

<div align="center">

99

</div>
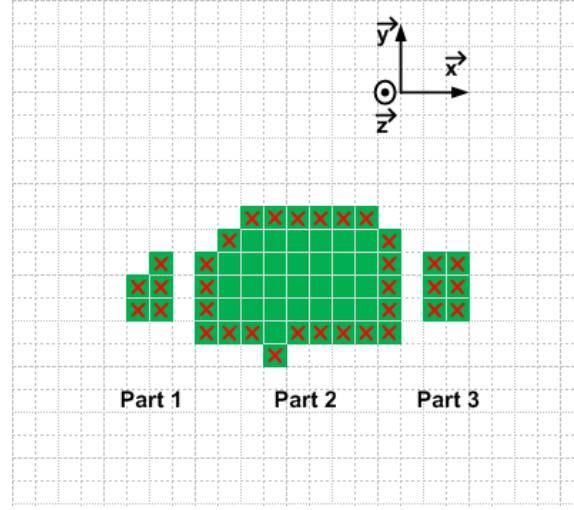
Figure A.1: Cross section of the rectangular cuboid at a certain height z_k. The height is chosen such that the cross plan meets the human body.

where h, $N_p^a(z_k)$ are the grid size and the number of pixels adjacent to the air in the cross plane z_k, respectively. Note that the grid size in Fig. A.1 is 25 mm. We set such coarse grid size for visualization purposes. However, the grid size in the implementation was set to 5 mm. Note that the numerical BSA slightly increases as the grid size decreases. For instance, a grid size of 2 mm results in an increase of the BSA of only 1 % for Thelonious, while the simulation time is 25 times higher. The simulation time was about 3 minutes for a grid size of 5 mm on a central processing unit (CPU) running at 3 GHz with a random access memory (RAM) of 4 GB while it was about 80 minutes for a grid size of 2 mm on the same machine.

A.2 Numerical determination of the total projected body surface area (BSA_{pr}^T) of heterogeneous phantoms

Recall that the BSA_{pr}^T is the sum of the projected human body surface from all the azimuthal angles, and is expressed as follows, see (5.3).

$$BSA_{pr}^T = \int_0^{2\pi} BSA_{pr}(\varphi)d\varphi, \tag{A.3}$$

where φ is the azimuthal angle, and $\text{BSA}_{pr}(\varphi)$ is the projected surface onto a plane along the azimuth φ. The discretized rectangular cuboid described in A.1 is used again to determine the BSA_{pr}^T, and let us consider the same height z_k of Fig. A.1. The human tissues are circumscribed in a rectangle ABCD in a (0,X,Y) coordinate system, as shown in Fig. A.2. Let us now define the coordinates of the points in Fig. A.2. $A_{0,\varphi}=A_0=A_\varphi=(0\ 0)'$; $B_0=(x_0\ 0)'$; $C_0=(x_0\ y_0)'$; $D_0=(0\ y_0)'$, where $'$ is the transpose notation. x_0 and y_0 are the maximum length of the phantom along the X and Y axis, respectively. In other words, x_0 and y_0 are

Figure A.2: Human tissues circumscribed in a rectangle and its rotation.

the length and width of the phantom in the cross plane z_k. One can obtain their values since the grid size h is known and the number of voxels (precisely pixels since the figure is in 2D) at each line can be easily determined. In Fig. A.2, $x_0 = N_p^X \times h$, and $y_0 = N_p^Y \times h$ where N_p^X and N_p^Y are the maximum number of pixels along the X axis and the Y axis, respectively. N_p^X (resp. N_p^Y) = 13 (resp. =7) in Fig. A.2. The goal is first to determine the length l_φ (see Fig. A.2) of the projected rectangle $A_\varphi B_\varphi C_\varphi D_\varphi$ onto the X axis. The projected surface at azimuth φ and cross plane z_k is defined by l_φ and the grid size h.

At the azimuth angle φ, the phantom is rotated with respect to φ. The coordinates of the rotation (along φ) of a certain point M $\in$ {A, B, C, D} are as follows: $M_\varphi = R(\varphi).M_0$, where $R(\varphi)$ is the rotation matrix defined as:

$$R(\varphi) = \begin{pmatrix} \cos(\varphi) & -\sin(\varphi) \\ \sin(\varphi) & \cos(\varphi) \end{pmatrix}. \tag{A.4}$$

Let M(φ) be defined as $M(\varphi) = (x_{M(\varphi)} \; y_{M(\varphi)})'$. The length l_φ at a certain discrete height z_k is given by:

$$l_\varphi^{z_k} = max(x_{A(\varphi)}, x_{B(\varphi)}, x_{C(\varphi)}, x_{D(\varphi)}) - min(x_{A(\varphi)}, x_{B(\varphi)}, x_{C(\varphi)}, x_{D(\varphi)}) \tag{A.5}$$

where max(.) and min(.) are the maximum and minimum value of the set between the brackets, respectively. Once l_φ can be determined for a certain z_k, the BSA$_{pr}^T$ is given as:

$$BSA_{pr}^T = \sum_{z_k} \sum_{\varphi} l_\varphi^{z_k} \times h \tag{A.6}$$

$$= h \times \sum_{z_k} \sum_{\varphi} l_\varphi^{z_k} \tag{A.7}$$

101

References

[1] R. S. Thoma A. Richter. "Parametric Modeling and Estimation of Distributed Diffuse Scattering Components of Radio Channels". In *COST273 TD(03)198, accesible via http://www.lx.it.pt/cost273/*, 2003.

[2] A. Richter. *"Estimation of Radio Channel Parameters: Models and Algorithms"*. PhD thesis, Faculty of electrical Engineering and Information Technology at the Technical University. Ilmenau, Germany., 2005.

[3] J. Poutanen, J. Salmi, K. Haneda, V. M. Kolmonen, and P. Vainikainen. "Angular and Shadowing Characteristics of Dense Multipath Components in Indoor Radio Channels". *IEEE Trans. Antennas Propag.*, 59: pages 245–253, 2011.

[4] ICNIRP. "Guidelines for limiting exposure to time-varying electric, magnetic, and electromagnetic fields (up to 300 GHz)". *Health Physics*, 74 (4): pages 494–522, 1998.

[5] E. Conil, A. Hadjem, F. Lacroux, M. F. Wong and J. Wiart. "Variability analysis of SAR from 20 MHz to 2.4 GHz for different adult and child models using finite-difference time-domain". *Phys. Med. Biol.*, 53: pages 1511–1525, 2008.

[6] G. Vermeeren, W. Joseph and L. Martens. "Whole-body SAR in spheroidal adult and child phantoms in a realistic exposure environment". *IEE Electronics Letters (44)13:*, (44) 13: pages 790–791, 2008.

[7] A. Hirata, N. Ito and O. Fujiwara. "Influence of electromagnetic polarization on the whole-body averaged SAR in children for plane-wave exposures". *Phys. Med. Biol.*, 54 (2009):N59–N65, 2009.

[8] T. Uusitupa, I. Laakso, S. Ilvonen and K. Nikoskinen. "SAR variation study from 300 to 5000 MHz for 15 voxels models including different postures". *Phys. Med. Biol.*, 55: pages 1157–1176, 2010.

[9] E. Conil, A. Hadjem, A. Gati, M. F. Wong and J. Wiart. "Influence of Plane-Wave Incidence Angle on Whole Body and Local Exposure at 2100 MHz". *IEEE Trans. Electromagn. Compat.*, 53, No. 1: pages 48–52, 2011.

[10] A. Hirata, O. Fujiwara, T. Nagaoka, S. Watanabe. "Estimation of Whole-Body Average SAR in Human Models Due to Plane-Wave Exposure at Resonance Frequency". *IEEE Trans. Electromagn. Compat.*, 52: pages 41–48, 2010.

[11] A. Hirata, S. Kodera, J. Wang, and O. Fujiwara. "Dominant Factors Influencing Whole-Body Average SAR Due to Far-Field Exposure in Whole-body Resonance Frequency and GHz Regions". *Bioelectromagnetics*, 28: pages 484–487, 2007.

[12] C. H. Durney, H. Massoudi, and M. F. Iskander. "Radiofrequency Radiation Dosimetry Handbook". *Brooks Air Force Base-USAFSAM-TR-85-73*, 1986.

[13] *IEEE Recommended Practice for Determining the Peak Spatial-Average Specific Absorption Rate (SAR) in the Human Head from Wireless Communications Devices: Measurement Techniques*, 2003.

[14] Foundation for Research on Information Technologies in Society (IT'IS). http://www.itis.ethz.ch/itis-for-health/virtual-population/human-models/ (accessed on October 21, 2014), 2014. http://www.itis.ethz.ch/itis-for-health/virtual-population/human-models/ (accessed on October 21, 2014).

[15] A. Taflove, S. Hagness. *"Computational electrodynamics: The finite-difference time-domain method"*. Norwood, MA, 3rd edition, 2005.

[16] F. W. Smith D. E. Merewether, R. Fisher. "On Implementing a Numeric Huygen's Source Scheme in a Finite Difference Program to Illustrate Scattering Bodies". *IEEE Trans. Nucl. Sci.*, 27 (6): pages 1829–1833, 1980.

[17] J. B. Andersen, J. Ø. Nielsen, G. F. Pedersen, G. Bauch, and M. Herdin. "Room Electromagnetics". *IEEE Antennas Propagat. Mag.*, 49, (2): pages 27–33, 2007.

[18] H. Kuttruff. *"Room Acoustics"*. Spon Press, London, 2000.

[19] J. B. Andersen, K. L. Chee, M. Jacob, G. F. Pedersen, T. Kürner. "Reverberation and Absorption in an Aircraft Cabin with the Impact of Passengers". *IEEE Trans. Antennas and Propag.*, 60 (5): pages 2472–2480, 2012.

[20] D. Du Bois and E. F. Du Bois. "A formula to estimate the approximate surface area if height and weight be known". *Arch Intern Medicine.*, 17: pages 863–871., 1916.

[21] S. Fujimoto, T. Watanabe, A. Sakamoto, K. Yukawa, K. Morimoto. "Studies on the physical surface area of Japanese. 18. Calculation formulae in three stages over all ages". *Nippon Eiseigaku Zasshi*, 5: pages 443–450., 1968.

[22] E. A. Gehan and S. L George. "Estimation of human body surface area from height and weight". *Cancer chemother Rep*, 54: pages 225–235, 1970.

[23] E. H. Livingston and S. Lee. "Body surface area prediction in normal-weight and obese patients". *American Journal of Physiology - Endocrinology and Metabolism*, 281: pages E586–E591, 2001.

[24] D. Ullmo, and H. U. Baranger. "Wireless Propagation in Buildings: A Statistical Scattering Approach". *IEEE Trans. Veh. Technol.*, 48 (3): pages 947–55, 1999.

[25] J. F. Bakker, M. M. Paulides, A. Christ, N. Kuster, and G. C. van Rhoon. "Assessment of induced SAR in children exposed to electromagnetic plane waves between 10 MHz and 5.6 GHz". *Phys. Med. Biol.*, 55: pages 3115–3130, 2010. Erratum in Phys. Med. Biol. 56(9) page 2883, 2011.

[26] A. A. M. Saleh and R. Valenzuela. "A Statistical Model for Indoor Multipath Propagation". *IEEE J. Select. Areas Commun. JSAC*, pages pages 128–137, 1987.

[27] J. B. Andersen, T. S. Rappaport, and S. Yoshida. "Propagation Measurements and Models for WiWireless Communications Channels". *IEEE Trans. Antennas Mag.*, pages pages 42–49, 1995.

[28] D. Chizhik, and J. Ling. "Propagation Over Clutter: Physical Stochastic Model". *IEEE Trans. Antennas Propag.*, 56 (4): pages 1071–1077, 2008.

[29] E.Tanghe, W. Joseph, M. Lienard, A. Nasr, P. Stefanut, L. Martens, and P. Degauque. "Statistical Analysis of Multipath Clustering in an Indoor Office Environment". *EURASIP Journal on Wireless Communications and Networking*, 2011:16 pages, 2011.

[30] G. Vermeeren, W. Joseph, C. Olivier, and L. Martens. "Statistical multipath exposure of a human in a realistic electromagnetic environment". *Health Physics*, 94, no. 4: pages 345–354, 2008.

6

Circuit model for diffuse fields and electromagnetic absorption prediction in rooms

6.1   Introduction

Several methods have been used to model the diffusion model in realistic indoor environments. The diffusion phenomena in a building floor has been investigated in e.g., [1, 2]. Reference [1] has shown that the diffusion model is governed by a differential equation of the first order, the solution of which is comprised of exponential terms. Later, [2] developed a statistically based diffusion model via the stochastic properties of the diffusion phenomena in indoor environments. Although these models predict excellently the diffusion behavior in indoor environments, they require the value of several parameters that may be difficult to obtain in practice. This is because the propagation phenomena are very complex in a realistic indoor environment. Therefore, realistic assumptions are necessary to model the diffusion phenomena in indoor environments and to determine in a simpler and efficient manner the human exposure due to the EMWs in such places.

As discussed in Chapter 3, the diffuse fields propagation in a single room is governed by the reverberation time, which describes completely the diffusion behavior inside the room and represents the decay rate of the energy in diffuse fields [3]. It is recalled that the reverberation time is only dependent on the room dimensions and the absorption properties of the surfaces (walls, ceiling, floor, etc.). Although some specular components may exist in an indoor environment, the room electromagnetics theory [3] focuses on the diffusion effect, assuming only one specular component, typically the LOS component - when it exists - in the channel response; the remainder is assumed to be part of the diffuse multipath components. The assumption of the room electromagnetics theory about the existence of only one specular component in the channel response is likely to occur in realistic environments since it has been shown - through measurements - that the

diffuse power density may be prominent in the total power involved in realistic indoor environments [4, 5], Section 4.5.2.

This chapter aims to introduce a new electrical circuit model based on the room electromagnetics theory developed in [3, 6] and briefly presented in Chapter 1. By applying (fast) circuit solvers, a complex electromagnetics problem can be calculated in this way. Such circuit models may be used by many not capable to or willing to get involved with the full wave simulations. The novelty of this circuit model relies *i)* in the use of the room dimensions to determine the exposure of a person located inside and *ii)* the translation of the room electromagnetics theory into a circuit model enabling fast assessment of indoor exposure and human absorption rate. Absorptions due to diffuse fields in both the narrow and ultra-wide band systems are investigated. Moreover, the method discards the need of modeling the roughness of the surfaces. The room electromagnetics [3] basic equations are described in Section 1.3 of Chapter 1.

This chapter is organized as follows: the model and the main concepts based on the room electromagnetics theory are highlighted in Section 6.2. The elements of the circuit model are also determined. In Section 6.3, the SAR_{wb} is obtained using the exposure calculated from the circuit model. An application of the theory in a realistic office environment is given in Section 6.4. Furthermore, the theory is implemented in a circuit simulating software. Finally, conclusions are drawn in Section 6.5.

6.2 Circuit model for diffuse fields

6.2.1 Concept

The principle of the circuit model is shown in Fig. 6.1, where a room and transmitting antenna Tx characteristics plus a person's location are the input parameters.
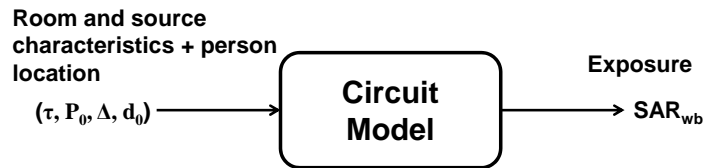
Figure 6.1: Principle of the circuit model. τ is the reverberation time of the considered room, P_0 is the transmitted power, Δ is the duration of the transmitted pulse, and d_0 is the separation between the human and the Tx

The exposure in terms of the power density - hence the SAR_{wb} - is given as the output. The Tx characteristics (P_0, Δ) and the person's separation from the Tx (d_0) are supposed to be known. Given the room dimensions, a simple method to determine the exposure without the need of carrying out any exposure measurements or simulations is presented. The theory applies to adjacent rooms' scenarios as well, and an application of the circuit model for a realistic office will be discussed. The strength of the method lies in its simplicity because it does not require any simulation of the entire room in an electromagnetic software

tool, which would be very time and memory consuming when the room dimensions increase. Depending on the bandwidth of the considered system, there are two scenarios to distinguish in the evolution of the diffuse fields' energy in indoor environments (see Fig. 6.2):

1. the active duration of the transmitted signal, i.e., Δ, is much smaller than the room reverberation time, which corresponds to the Ultra-Wide Band (UWB) systems cases ($\Delta << \tau$);

2. the active duration of the transmitted signal is larger than the reverberation time ($\Delta >> \tau$), which corresponds to the WLAN systems cases;

In general, the reverberation time of an indoor environment is of the order of a few tens of nanoseconds e.g., $\approx$ 30-50 ns (Chapter 3) and the pulse duration Δ of UWB systems is only a few nanoseconds (even picoseconds). Typical value of Δ is $\approx$ 209 μs for a WLAN system [7]. The active duration Δ is the time period during which the transmitted pulse is different from zero (pulse duration), i.e., P(t)=P$_0$. The energy evolution of the two systems is different and is shown in Fig. 6.2.
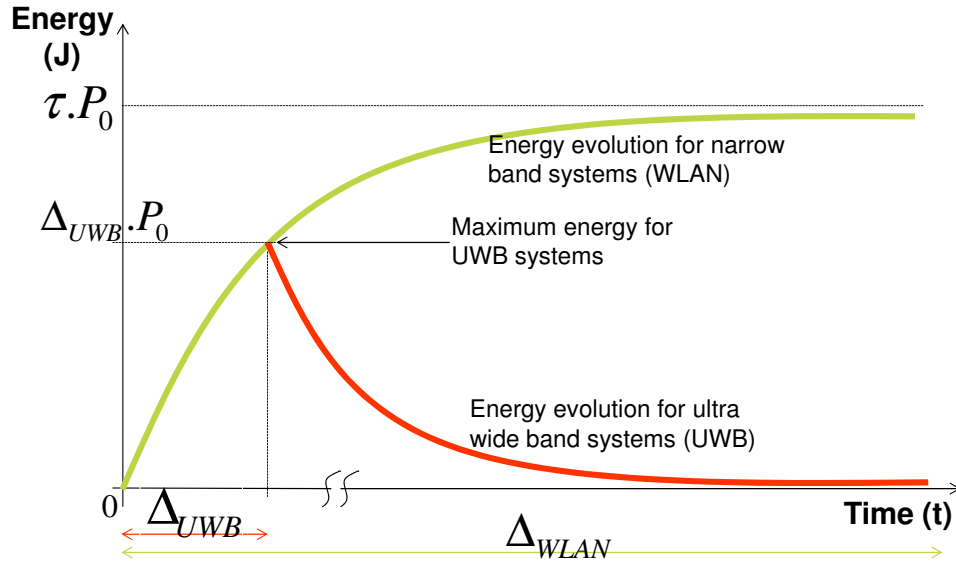
Figure 6.2: Energy evolution for ultra-wide-band (UWB) and narrow-band (WLAN) systems in room electromagnetics

From 0 to Δ_{UWB} (as long as the source is on), the energy of the UWB systems evolves up to a maximum value, i.e., ΔP_0. As soon as the source is off (t> Δ_{UBW}), the energy decreases exponentially from its peak value towards zero with the reverberation time being the damping factor.

6.2.2 Model for incident power density for UWB systems

The present circuit model theory is developed in analogy with [6], where the diffuse power density has been investigated. It is assumed that the pulse duration is much lower than the reverberation time [6].

Therefore, the theory developed in this section is only valid for the UWB systems.

The energy for a small pulse duration Δ (UWB systems) in a room is obtained from (1.11):

$$W_d(t) = \frac{P_0 \tau}{V} \left(e^{\frac{\Delta}{\tau}} - 1 \right) e^{-\frac{t}{\tau}} \tag{6.1}$$

The resulting total power density from t_0 in a diffuse field is as follows:

$$I_d(t_0) = \frac{P_0}{\pi \eta A} e^{-\frac{t_0}{\tau}} \tag{6.2}$$

where P_0 is the transmitted power.

For the WLAN systems where Δ is much more larger, the energy grows from zero toward a steady state, whose value is τP_0.

Model for the incident power density in the same room

Let us consider the RC circuit of Fig. 6.3. The equation governing the voltage is as follows:

$$E(t) = U(t) + RC \frac{dU(t)}{dt} \tag{6.3}$$

where $E(t)$, $U(t)$, R, and C are the source voltage, voltage over the capacity, resistor, and the capacity, respectively. This differential equation describes the charge (resp. discharge) of the capacitance when the source is on (resp. off). The solution of (6.3) is given by (6.4):
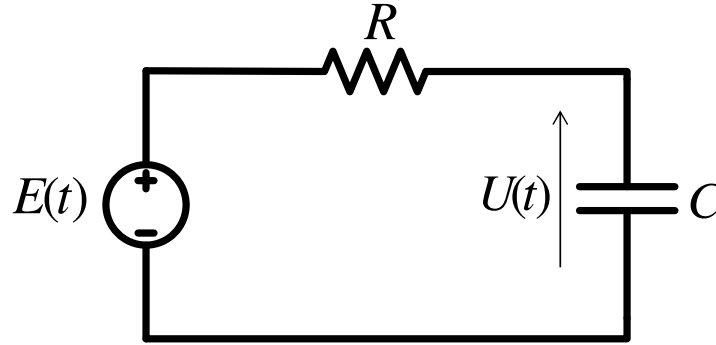
Figure 6.3: Circuit model equivalent to room electromagnetics theory

$$U(t) = \frac{1}{RC} \int_0^\infty E(t - t') e^{-\frac{t'}{RC}} dt' \tag{6.4}$$

As the pulse signal is transmitted in the considered room during a period of time Δ, the circuit model is fed with E(t) during the same duration Δ and is defined as follows:

$$E(t) = \begin{cases} E & \text{if} \quad 0 \leq t \leq \Delta \\ 0 & \text{otherwise} \end{cases}$$

The general solution of (6.4) is as follows:

$$U(t) = E\left(e^{\frac{\Delta}{RC}} - 1\right)e^{-\frac{t-\Delta}{RC}}, \qquad t \geq 0$$

$$= U_0 e^{-\frac{t-\Delta}{RC}}, \qquad t \geq 0 \tag{6.5}$$

$U(t)$ looks like the classical expression of the voltage's charge for $0<t\leq \Delta$ (resp. discharge for t$\geq \Delta$) in a capacitance C with the final (resp. initial) voltage being U_0, which is expressed as follows:

$$U_0 = E\left(e^{\frac{\Delta}{RC}} - 1\right). \tag{6.6}$$

Actually, U_0 is the voltage in the capacitance just after turning the source E(t) off. Considering only the decay of the voltage, i,e, the source is turned off, (6.5) turns into:

$$U(t) = E\left(e^{\frac{\Delta}{RC}} - 1\right)e^{-\frac{t}{RC}}, \qquad t \geq \Delta$$

$$= U_0 e^{-\frac{t}{RC}}, \qquad t \geq \Delta \tag{6.7}$$

Assume that the total energy in the room can be stored in the capacitance C. The energy density (in Watt.s/m^3) in the room can be expressed as a function of the room volume and the capacitance's energy as follows:

$$W_d(t) = \frac{1}{2}CU^2(t) \times \frac{1}{V}, \qquad t \geq \Delta$$

$$= \frac{C}{2V}U_0^2 e^{-\frac{2t}{RC}}, \qquad t \geq \Delta \tag{6.8}$$

By comparing the energy density in the capacitance, i.e., (6.8), and in the room electromagnetics theory, i.e., (6.1), and assuming the same decay rate the following relations are derived:

$$\frac{RC}{2} = \tau \tag{6.9}$$

$$R = \frac{U_0^2}{P_0(e^{\frac{\Delta}{\tau}} - 1)}, \qquad \left(\Omega\right)$$

By choosing arbitrarily a value of U_0 and knowing P_0, Δ and τ, the value of R can be easily computed. Once the resistor R is calculated, (6.9) is used to determine the value of the capacitance:

$$C = 2\tau \frac{P_0\left(e^{\frac{\Delta}{\tau}} - 1\right)}{U_0^2}, \qquad \left(F\right) \tag{6.10}$$

The total power density $I_D(d_0)$ at a location d_0 in the room is now calculated. Assuming a Lambertian scattering of the electromagnetic waves (EMW) on the surfaces, i.e., the EMWs are scattered in all the directions independently of their arrival angle, as in [8, 9], the scattering process ends up in a complete diffuse field. The power density is direction-independent in complete diffuse fields, thus the power density I(t) in the capacitance is obtained from (1.10) as follows:

$$I(t) = \frac{c_0}{4\pi} \times \frac{1}{2V}CU^2(t)$$

$$= \frac{c_0}{8\pi V}CU_0^2 e^{-\frac{2t}{RC}} \tag{6.11}$$

The total power density I_D from t_0 on is the total energy density from t_0 divided by the time duration:

$$I_D(t_0) = \frac{1}{\Delta} \int_{t_0}^{\infty} I(t)dt \tag{6.12}$$

where t_0 is the arrival delay of the first diffuse component. Taking (6.9) and (6.11) into account, a solution of (6.12) is as follows:

$$I_D(t_0) = \frac{\tau c_0 C}{8\pi \Delta V} U_0^2 e^{-\frac{t_0}{\tau}} \tag{6.13}$$

The total power density can be rewritten as:

$$I_D(t_0) = \frac{\tau c_0 C}{8\pi \Delta V} U^2(t_0) \tag{6.14}$$

$$= \frac{\tau^2 c_0 P_0}{4\pi \Delta V} \left(e^{\frac{\Delta}{\tau}} - 1 \right) e^{-\frac{t_0}{\tau}} \tag{6.15}$$

Note that in (6.14), the power density is expressed as a function of the voltage over the capacitance. Moreover, (6.15) proves that the total power density I_D in the circuit model is independent of the voltage U_0, hence of E(t). Indeed, the power density depends on the room characteristics (V and τ) and of the source characteristics (P_0 and Δ).

The diffuse field's power density has been earlier addressed in [6] where it was assumed that the time period Δ is much smaller compared to the reverberation time τ. Since the same assumption is made here, let us now derive the power density expression in the circuit model when $\frac{\Delta}{\tau} \longrightarrow 0$ (i.e., $\Delta \ll \tau$) for comparison purpose:

$$\lim_{\frac{\Delta}{\tau} \to 0} I_D(t_0) = \lim_{\frac{\Delta}{\tau} \to 0} \frac{\tau^2 c_0 P_0}{4\pi \Delta V} (e^{\frac{\Delta}{\tau}} - 1) e^{-\frac{t_0}{\tau}} \tag{6.16}$$

$$= \frac{\tau c_0 P_0}{4\pi V} e^{-\frac{t_0}{\tau}}$$

$$= \frac{P_0}{\pi \eta A} e^{-\frac{t_0}{\tau}} \tag{6.17}$$

which is the same expression as in (6.2). In (6.16), we assume that $e^{\frac{\Delta}{\tau}} \approx \left(1 + \frac{\Delta}{\tau}\right)$ since $\Delta \ll \tau$. Equation (6.17) indicates that the power density derived from the circuit model is the same as the one determined in the theory of the room electromagnetics. This is logical because of (6.9) and (6.10).

The distance from a Tx can be more easily measured than the arrival delay of an EMW; thus it is more convenient to express the power density as a function of the distance. For this purpose, let us assume that the first diffuse field component has the same arrival delay as the LOS component. This hypothesis is enforced by the fact that the room electromagnetics theory assumes that the diffuse fields (see Fig. 1.5 of Chapter 1) arrive just after the LOS component. Given a certain separation d_0 from the Tx, the total power density in the circuit model is:

$$I_D(d_0) = \frac{\tau^2 c_0 P_0}{4\pi \Delta V} \left(e^{\frac{\Delta}{\tau}} - 1 \right) e^{-\frac{d_0}{c_0 \tau}}$$

$$= \frac{\tau c_0 P_0}{4\pi V} e^{-\frac{d_0}{c_0 \tau}} \tag{6.18}$$

Theory for adjacent rooms

The room electromagnetics theory extended to the adjacent room scenarios is addressed in Chapter 3. The main principles are recalled below. Let us consider a receiver (or person) located in a room R_{rx} and a transmitter located in an adjacent room R_{tx}, as illustrated in Fig. 6.4. P(t)=P$_0$ is the transmitted power in the room R_{tx}, and α^2 is the transmission factor of the wall separating both rooms.
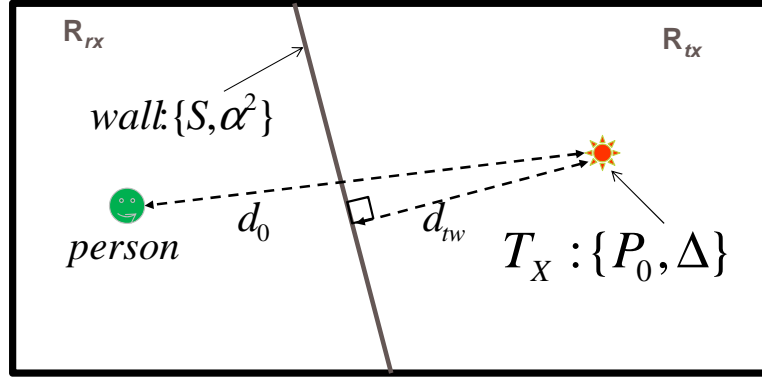
Figure 6.4: Adjacent room scenario schematic

Complete diffuse fields are assumed in both rooms so that the power density will be direction independent, i.e., $I(\theta,\varphi)=I$, where θ is the elevation angle and φ is the azimuth angle. The room R_{rx} is then fed by two sources:

1. P$_r$(t): which is the received LOS (or first component) power from the room R_{tx}. In fact, P$_r$ is the transmitted LOS power P(t), which is the incident power scaled with the wall transmission factor and corrected with the loss due to the free-space propagation from the Tx to the wall separating both rooms.

2. P$_{exch}$: the power induced by diffuse energy exchanged from the room R_{tx} to the room R_{rx} through the surface S of the wall separating the rooms.

The received powers in the rooms R_{rx} are balanced as follows:

$$P_r + P_{exch} = V_{rx}\frac{dW_{rx}}{dt} + \frac{c_0 A'_{rx}}{4}W_{rx} \tag{6.19}$$

where V_{rx}, W_{rx}, and A'_{rx} are respectively the volume, energy density, and the effective absorbing area of the room R_{rx}. The exchanged power from the room R_{tx} to the room R_{rx} is related to the energy density in the room R_{rx}:

$$P_{exch} = \frac{c_0 S}{4}W_{rx} \tag{6.20}$$

The solution of (6.19) is given by:

$$W_{rx}(t) = \frac{1}{V_{rx}}\int_0^\infty P_r(t-t')e^{-\frac{t'}{\tau_a}}\,dt' \tag{6.21}$$

where τ_a is the reverberation time in the room R_{rx} when Tx is located in the room R_{tx}, and P_r is defined as:

$$P_r(t) = \begin{cases} P_r & \text{if} \quad 0 \leq t \leq \Delta \\ 0 & \text{otherwise} \end{cases}$$

Assume that the shortest distance from Tx to the wall separating both rooms is d_{tw}, and that a LOS plane wave impinges on the wall with surface S. Therefore, the first received power component in the room R_{rx} is as follows:

$$P_r = \alpha^2 \frac{P_0}{4\pi d_{tw}^2} S \tag{6.22}$$

The energy density in the room R_{rx} is then (a solution of (6.21)):

$$\begin{aligned} W_{rx}(t) &= \frac{P_r \tau_a}{V_{rx}} \left(e^{\frac{\Delta}{\tau_a}} - 1 \right) e^{-\frac{t}{\tau_a}} \\ &= \frac{\alpha^2 P_0 S \Delta}{4\pi d_{tw}^2 V_{rx}} e^{-\frac{t}{\tau_a}} \end{aligned} \tag{6.23}$$

The reverberation time τ (when the transceivers are in the same room) and τ_a are linked via the following formula (see Section 3.2.4):

$$\begin{aligned} \tau_a &= \frac{\tau}{1 - \frac{S}{A'_{rx}}} \\ &= \frac{\tau}{1 - \frac{c_0 \tau S}{4 V_{rx}}} \end{aligned} \tag{6.24}$$

In analogy to the developed theory for the same-room case, the circuit model for adjacent rooms is shown in Fig. 6.5. R_a is the resistance and C_a is the capacitance. Once again, by comparing the energy density in the
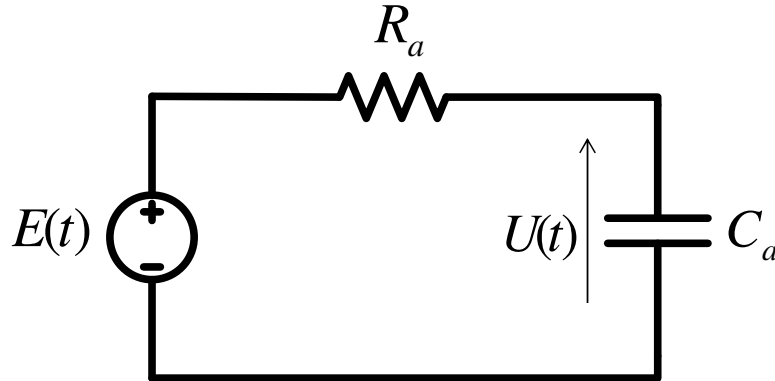
Figure 6.5: Circuit model equivalent to room electromagnetics theory for adjacent rooms

circuit model, i.e., (6.8), and the energy density from the adjacent rooms theory, i.e., (6.23), we derive the

following relations:

$$\frac{R_a C_a}{2} = \tau_a \tag{6.25}$$

$$R_a = \frac{4\pi d_{tw}^2 \tau_a}{\alpha^2 S} \times \frac{U_0^2}{\Delta P_0} \tag{6.26}$$

Since R_a is computed from (6.26), the capacitance C_a is determined from (6.25) with the knowledge of τ_a. Similarly to the same-room case, the power density expression for adjacent rooms is:

$$
\begin{aligned}
I_{D,a}(t_0) &= \frac{\tau_a c_0 C_a}{8\pi \Delta V_{rx}} U^2(t_0) \\
&= \frac{\tau_a c_0 P_r}{4\pi V_{rx}} e^{-\frac{t_0}{\tau_a}} \\
I_{D,a}(d_0) &= \frac{\tau_a c_0}{4\pi V_{rx}} \frac{\alpha^2 P_0 S}{4\pi d_{tw}^2} e^{-\frac{d_0}{c_0 \tau_a}}
\end{aligned}
\tag{6.27}
$$

Including the LOS component in the model (UWB)

The goal of the circuit model is primarily to model the power density of the diffuse fields. However, in order to use the circuit model to address the human exposure within the room electromagnetics context, it should include the power density of the first arriving component as well (this is LOS component for the same-room scenario), since the SAR_{wb} is induced by both sources. Note that the human absorption is quantified in terms of the SAR in the RF region [10]. Given an incident plane wave, its power density at a certain distance d_0 is

$$I_L = \frac{\alpha^2 P_0}{4\pi d_0^2} \tag{6.28}$$

where I_L, α^2, and d_0 are the power density of the first arriving component, the transmission factor of the wall (if any), and the separation from the Tx, respectively. For the same room scenario, $\alpha^2 = 1$ since there is no transmission through a wall. In the adjacent-room case, an assumption is made that the first-arriving component travels along the line connecting the Tx and Rx (distance equal to d_0, see Fig. 6.4.)

Consider that the first arriving component (LOS for the same-room scenario) power density illuminates a person, which results in a certain absorption cross section, i.e., ACS_{los}. The power P_{los}^{abs} absorbed by that person is as follows:

$$
\begin{aligned}
P_{los}^{abs} &= I_L \times ACS_{los} \\
&= \frac{\alpha^2 P_0}{4\pi d_0^2} \times ACS_{los}
\end{aligned}
\tag{6.29}
$$

The voltage of the circuit model has not yet been set to a particular value. Therefore, the maximum voltage U_0 in the capacitance can be defined as follows:

$$
\begin{aligned}
U_0^2 &= Z_0 \times P_{los}^{abs} \\
U_0 &= \sqrt{Z_0 \times \frac{\alpha^2 P_0}{4\pi d_0^2} \times ACS_{los}}
\end{aligned}
\tag{6.30}
$$

113

where Z_0 is the free-space impedance (i.e., $Z_0 = 120\pi\ \Omega$). Since U_0 is now known, the circuit model's input voltage E(t) is determined with (6.6). Finally, the LOS component power density in the circuit model is given by

$$I_L = \frac{U_0^2}{Z_0 \times ACS_{los}} \tag{6.31}$$

which is only dependent of the capacitance maximum voltage and the human body surface illuminated by the LOS component. The circuit model derived here determines the exposure, i.e., the power densities, (and afterwards the SAR_{wb}) for only one person at a given location. If different persons stand at different distances from the Tx, different circuit models are then needed. So, in general, the SAR_{wb} in different humans in a room will be predicted by a set of independent circuit models (see Section 6.4).

The authors of [11] have shown that the highest absorption rate occurs for plane waves incident to the front of an exposed human or phantom. The ACS_{los} depends on the incident LOS component's direction and its polarization, as evidenced in Chapter 5. The ACS_{los} is supposed to be a known parameter here, which already takes the direction and polarization of the incident plane wave into account.

6.2.3 Model for incident power density for WLAN narrow-band systems ($\Delta >> \tau$)

Nowadays, the WLAN IEEE 802.11 standard systems are widely deployed in residential/office environments. For these systems, the active duration of the transmitted signal Δ is of the order of a few hundreds of microseconds [7], whereas the reverberation time is about a few tens of nanoseconds. Therefore, the $\Delta << \tau$ assumption does not hold anymore and this case needs to be addressed otherwise. From the room electromagnetics point of view, the energy density evolution is still governed by (1.11) and (6.21) for the same room and the adjacent rooms, respectively. The active duration of the transmitted pulse is several thousands times the reverberation time value. Therefore, the energy density can thus evolve to a steady state as we previously mentioned in Section 6.2.1. The energy density for the same room can be found by integration of (1.11) from 0 to t.

$$W_d(t) = \frac{\tau P_0}{V}\left(1 - e^{-\frac{t}{\tau}}\right) \tag{6.32}$$

Similarly to the UWB case, the power density for the narrow-band systems is calculated now with $\Delta >> \tau$ assumption in mind. Given the energy density in (6.32) and assuming complete diffuse fields, the power density is as follows:

$$\begin{aligned} I(t) &= \frac{c_0}{4\pi}W_d(t) \\ &= \frac{P_0\tau c_0}{4\pi V}\left(1 - e^{-\frac{t}{\tau}}\right) \end{aligned} \tag{6.33}$$

The signal is transmitted during Δ, the total power density from t_0 on is then as follows:

$$\begin{aligned} I_D(t_0) &= \frac{1}{\Delta}\int_{t_0}^{\Delta} I(t)dt\ , \qquad t_0 < \Delta \\ &= \frac{P_0\tau c_0}{4\pi V}\left(1 - \frac{t_0}{\Delta} + \frac{\tau}{\Delta}e^{-\frac{\Delta}{\tau}} - \frac{\tau}{\Delta}e^{-\frac{t_0}{\tau}}\right) \end{aligned} \tag{6.34}$$

Because of the narrow band assumption, i.e., $\Delta \gg \tau$, the two last terms of (6.34) tend towards 0, so they are negligible in the equation. Considering a residential or an office environment with a maximum length of 300 m leads to a maximum arrival delay t$_0$ of the LOS component of about 1000 ns. Considering that Δ is of order of a few hundred of microseconds, the term $\frac{t_0}{\Delta}$ can thereby be neglected as well, leading to the final expression of the power density:

$$
\begin{aligned}
I_D(t_0) &= \frac{c_0}{4\pi V}\tau P_0 \\
&= \frac{P_0}{\pi \eta A}
\end{aligned}
\tag{6.35}
$$

Unlike the UWB case, the diffuse power density in a room in steady state for the narrow-band system (WLAN) is independent of the distance d$_0$ from the Tx; it only depends on the room and the Tx characteristics. The power density exhibits no exponential decay, thus it is not modeled with a circuit model. Likewise, the power density for the adjacent rooms scenario is found by integrating (6.21). Following the same procedure, the total power density for the adjacent rooms is as follows:

$$
\begin{aligned}
I_{D,a}(t_0) &= \frac{c_0}{4\pi V_{Rx}}\tau_a P_r \\
&= \frac{c_0 \tau_a}{4\pi V_{Rx}} \times \frac{\alpha^2 P_0 S}{4\pi d_{TW}^2}
\end{aligned}
\tag{6.36}
$$

6.3 Determination of the SAR$_{wb}$ from the exposure

6.3.1 Expression for ultra-wideband systems

The power densities for both sources (diffuse fields and LOS component) are known via the circuit model. The whole-body specific absorption rate in a person is then easily derived:

$$
\begin{aligned}
SAR_{wb} &= SAR_{dmc} + SAR_{los} \\
&= \frac{1}{m}(I_D \times ACS + I_L \times ACS_{los}) \\
&= \frac{1}{m}\left(\frac{\tau c_0 C}{8\pi \Delta V}U^2(\frac{d_0}{c_0})ACS + \frac{U_0^2}{Z_0} \right)
\end{aligned}
\tag{6.37}
$$

where SAR_{wb} and m are the total whole-body specific absorption rate and the mass of the exposed person, respectively. For the adjacent rooms case, τ and C have to be replaced by τ_a and C$_a$, respectively.

6.3.2 Expression for narrow-band systems

The SAR$_{wb}$ is derived in a similar way as for the UWB case:

$$
\begin{aligned}
SAR_{wb} &= SAR_{dmc} + SAR_{los} \\
&= \frac{1}{m}(I_D \times ACS + I_L \times ACS_{los})
\end{aligned}
\tag{6.38}
$$

The SAR_{wb} in the same and adjacent rooms are then given as follows:

$$SAR_{wb} \begin{cases} = \frac{1}{m} \left(\frac{c_0 \tau P_0}{4\pi V} ACS + \frac{P_0}{4\pi d_0^2} ACS_{los} \right) \text{ for the same room} \\ = \frac{1}{m} \left(\frac{c_0 \tau_a}{4\pi V} \frac{\alpha^2 P_0 S}{4\pi d_{tw}^2} ACS + \frac{\alpha^2 P_0}{4\pi d_0^2} ACS_{los} \right) \text{ for the adjacent rooms} \end{cases}$$

where d_{tw} and d_0 are the shortest distance between the Tx and the adjacent room, and the distance separating the Tx to the exposed person, respectively. As previously mentioned, the prediction of the SAR_{wb} due to WLAN systems is performed without the circuit model.

6.4 Application

In the following section, we show how the circuit model can be used to determine in practice the SAR_{wb} of humans in realistic indoor environments.

6.4.1 Determination of the reverberation time as a function of the room dimensions

Depending on the trade off between the accuracy and the simplicity, the reverberation time value can be determined using the radiosity method [16], or by carrying out measurements [3, 6, 17], respectively. The methodology proposed here to determine the reverberation times aims to avoid the need of performing measurements or computations, which would be both difficult and time consuming. The reverberation time value is rather determined in a simpler but practical way. To this end, the effective roughness of the surfaces and the Lambertian diffusion model are used as in [8, 9]. The effective roughness includes not only the roughness of the surfaces, but the inside of the surfaces as well. It is recalled that the reverberation time expression of the room *i* as follows:

$$\tau_i = \frac{4V_i}{c_0 \eta A_i} \tag{6.39}$$

where τ_i, V_i, η, and A_i are the reverberation time value, the room volume, the average fraction of energy absorbed by the room surfaces, and the total area of the surfaces taking part in the diffusion process, respectively.

The main challenge resides now in the determination of the fraction of energy absorbed by the surfaces (the walls, the floor and the ceiling). To make this easy, let us suppose the following assumptions:

1. η is supposed to be uniform for all the absorbing areas (walls, ceiling, floor). The fraction of energy η determined here can be interpreted in an average sense. In the diffuse scattering literature [18], (1-η) is assimilated to the diffuse scattering coefficient, which is the ratio of an incident wave (in terms of energy) being scattered after interaction upon a rough surface;

2. the surfaces of the walls, the ceiling, and the floor are assumed to be Lambertian and perfectly diffuse. The Lambertian assumption states that the pattern of the scattered rays is independent of the incident EMW's direction [18].

The Lambertian's law approximates well the reflectance of some surfaces such as the flat paints [18]. This makes the Lambertian's law quite suitable for indoor environments. According to this law, the bidirectional

reflectance of a perfectly diffuse surface is [18]:

$$r_L(\theta_i) = \frac{1}{\pi}\cos(\theta_i),\tag{6.40}$$

where r_L, and θ_i are the bidirectional reflectance, and the angle between the incident plane wave and the normal of the surface, respectively. The scattering process can be seen in Fig. 6.6.
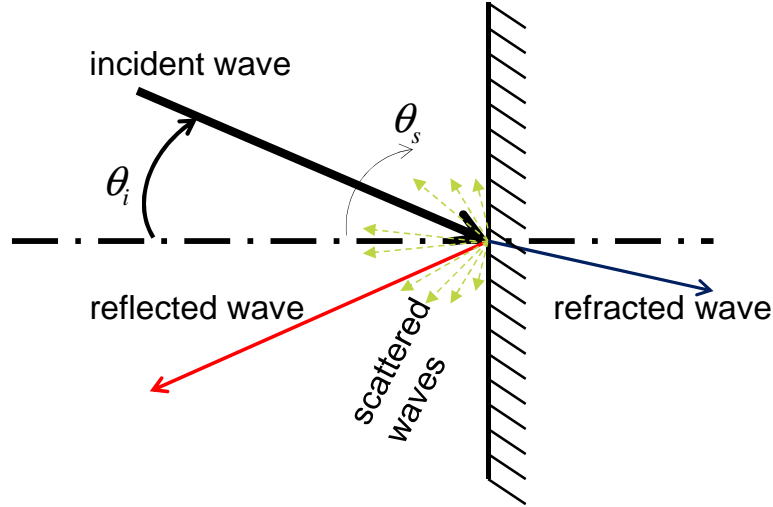
Figure 6.6: Illustration of the interaction between a plane wave and a rough surface

The reflectance is defined in [18] as the fraction of the incident wave's intensity scattered diffusely into many directions by a geometrically complex medium (see Fig. 6.6). The term *bi-directional* refers to the orientation of the source (the incident plane wave) and the detector (a scattered wave). Actually, we are interested in the directional-hemispherical reflectance since the source is a LOS signal and the diffuse waves emerge in the whole upper half-sphere of the surface (electromagnetic rays emerge in all directions in a diffuse scenario). The directional-hemispherical reflectance is called scattering coefficient elsewhere in the literature [18]. The actual expression of the directional-hemispherical reflectance is complex because it involves the properties of the particles forming the considered surface and the inside. The actual expression is very difficult - if not impossible - to obtain in practice because of the lack of information of these particles. Therefore, the directional-hemispherical reflectance ($0 \leq \rho \leq 1$) is determined here by integrating the bi-directional reflectance (6.40) over the half space as follows:

$$\begin{aligned}\rho &= \frac{1}{2\pi}\int_{\varphi=0}^{2\pi}\int_{\theta_s=0}^{\frac{\pi}{2}} r_L(\theta_i)\sin(\theta_s)d\theta_s d\varphi \\ &= r_L(\theta_i)\end{aligned}\tag{6.41}$$

where ρ is the directional-hemispherical reflectance (i.e., reflection coefficient for diffuse scattering), θ_s is the angle between the normal to the surface and a given scattered ray, and φ is the azimuthal angle. The

incident source is a LOS plane wave perpendicular to the walls, i.e., θ_i=0. Therefore, the calculation of (6.41) yields to $\rho = \frac{1}{\pi} \approx 0.32$. Note that the formula is independent of the frequency. The scattering coefficient is likely to be independent of the frequency up to a certain limit. This is confirmed by experimental measurements in indoor environments where the average absorption coefficient of building walls is nearly constant from 2 to 6 GHz [19].

Note that the authors of [20] have used a directive scattering pattern instead of a Lambertian model, and they have found that a scattering coefficient of 0.4 is the best value for indoor environments at 3.6 GHz, resulting in a relative error of 20%. Moreover, [8] used a Lambertian model to determine the scattering coefficient at 900 MHz and have found a value of 0.316, which is very similar to the value that we determined here since a relative error of less than 1% is obtained. A lambertian scattering value of 0.4 was found for building walls at the frequency of 1296 MHz in [9]. Regarding these values, the scattering coefficient determined here agrees with the values obtained in the literature although the frequencies are different. The fraction of the diffuse energy absorbed by a surface is thus:

$$\eta = 1 - \rho$$
$$= 0.68$$

However, (6.39) is only valid for small values of η [16, 21, 22]. When dealing with higher η, it is corrected by the following [22]:

$$\eta_c = -\log(1-\eta) * (1 + \frac{\gamma^2}{2} \log(1-\eta)) \tag{6.42}$$

where η_c is the corrected η, and γ^2 is a parameter taking into account the relative dimensions of the considered room. Actually, this parameter is the relative variance of the path length distributions in a room and the corresponding values can be found in [22]. When η is corrected with (6.42), the Sabine's law i.e., (6.39) becomes the Eyring's law.

6.4.2 Configuration

The configuration of Fig. 6.7 is considered. This is the floor plan of our office environment in Ghent, also shown in Fig. 3.3 of Chapter 3. In the following sections, the SAR_{wb} in the persons indicated in Fig. 6.7 as P_{11}, P_{12}, P_{21}, and P_{31} is investigated using the circuit model. The notation P_{ij} designates the person j in the room i. A Tx is located in the room 1 (R_1) which contains the persons P_{11} and P_{12}. The persons P_{21} and P_{31} are located in the adjacent rooms, i.e., room 2 (R_2) and room 3 (R_3), respectively. The surface of the walls separating R_1-R_2 and R_1-R_3 are S_{12}=28.30 m^2 and S_{13}=18 m^2, respectively. Because the smooth glasses do not diffuse the electromagnetic waves, they have not been accounted for in the calculation of the absorbing area. The Tx is located at d_{TW2}=4.70 m and d_{TW3}=5.65 m from the wall S_{21} and S_{31}, respectively. Using the room dimensions and equations (6.42) and (6.39), a reverberation time value of about 32.0 ns, 31.30 ns, and 20.10 ns are obtained for the rooms R_1, R_2, and R_3, respectively. The characteristics of the rooms and the reverberation time values are summarized in Table 6.1. The relative dimensions are
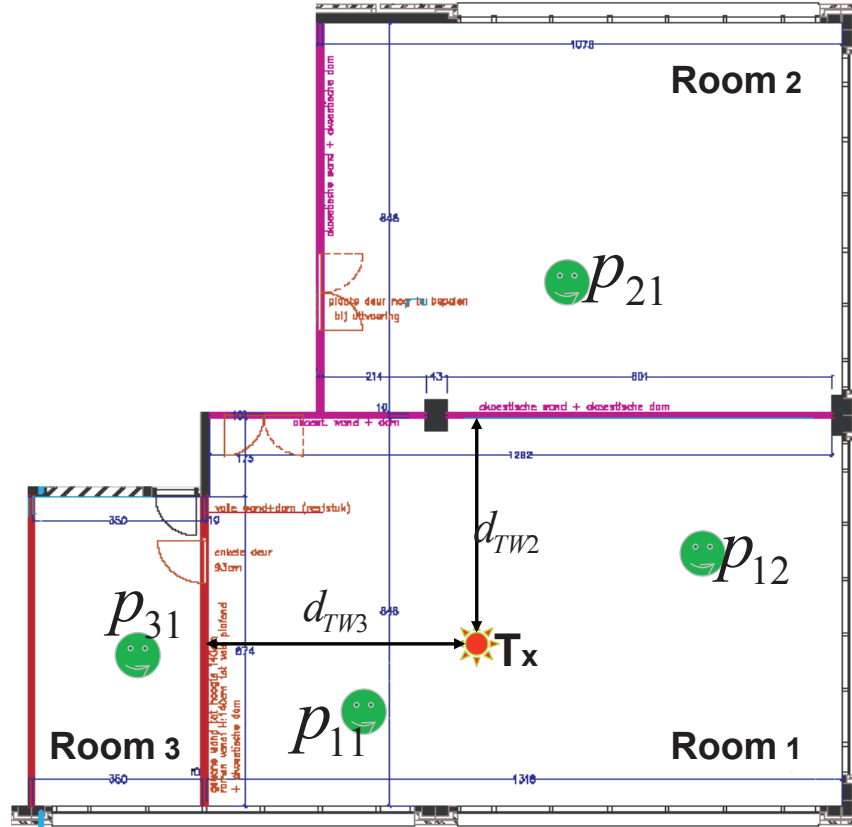
Figure 6.7: Ground plan of the investigated rooms with people locations

defined as (1:width/height:length/height), where the result of each ratio is rounded to the nearest integer of the following set of integers, i.e., 1, 2, 5, and 10 defined in [22].

6.4.3 Determination of the circuit model elements for UWB systems

Consider an UWB system operating at 2.50 GHz within a bandwidth of 1 GHz. The effective isotropically radiated power (EIRP) level limitations for the UWB systems are issued by the U.S frequency regulator, i.e., the Federal Communications Commission (FCC). For the indoor communications, a power spectral density of about -51.30 dBm/MHz sets the transmission level for communications between 2 and 3 GHz [23]. A 1 GHz bandwidth corresponds then to an EIRP of 7.40 mW and an active pulse duration Δ of 1 ns. For each exposed person, the elements of the circuit model to determine are the resistance R, the capacitance C, and the maximum voltage U_0 in the capacitance. The input voltage of the circuit model is expressed as a function of the person's ACS, i.e., (6.30). We obtained a typical value of 0.35 m^2 at 2.30 GHz based on measurements on real humans (see Section 3.4 of Chapter 3). This is chosen as the ACS$_{wb,dmc}$ value (ACS in diffuse fields), which in turn, leads to an ACS$_{los}$ of 0.175 m^2 for a frontal LOS plane wave illumination. The

119

Room	relative dimensions	γ^2	η_c	Volume (m^3)	Area (m^2)	τ (ns)
R1	1:2:5	0.403	0.4455	300	280	32.06
R2	1:2:5	0.403	0.4455	245	234	31.33
R3	1:1:2	0.356	0.4513	63.10	92.60	20.13

Table 6.1: Characteristics of the three investigated rooms

penetration loss of the wall (7 dB) is accounted for in the adjacent room elements computation. Table 6.2 lists the resulting equivalent circuit elements for the configuration shown in Fig. 6.7.

Person	distance (m)	U_0 (mV)	resistance R (Ω)	capacitance C (nF)	τ or τ_a (ns)
p_{11} (R1)	3	66	18.60	3.45	32.10
p_{12} (R1)	6	33	4.60	13.80	32.10
p_{21} (R2)	10	18	22.80	3.80	43.00
p_{31} (R3)	8	22	63.50	1.10	35.40

Table 6.2: The circuit model elements

Whole-body SAR from theoretical formula

Equations (6.18) and (6.27) can be used to compute the diffuse power density in the room R_1 and its adjacent rooms (R_2 and R_3), respectively. The LOS power density is determined with (6.28). Assuming that the person's mass is about 70 kg, the theoretical SAR$_{wb}$ values in the exposed persons are determined and the results are shown in Table 6.3. As expected, the higher SAR$_{wb}$ occurs in the person p_{11} because of its vicinity to the Tx. The lowest SAR$_{wb}$ is induced in the person p_{21} since he is the furthest from the Tx. It

Person	distance (m)	I_D (mW/m^2)	I_L (mW/m^2)	SAR$_{wb}$ (μW/kg)
p_{11} (R1)	3	$1.40\ 10^{-2}$	$6.60\ 10^{-2}$	0.235
p_{12} (R1)	6	$1.03\ 10^{-2}$	$1.65\ 10^{-2}$	$9.27\ 10^{-2}$
p_{21} (R2)	10	$1.18\ 10^{-3}$	$4.91\ 10^{-3}$	$1.82\ 10^{-2}$
p_{31} (R3)	8	$1.70\ 10^{-3}$	$7.34\ 10^{-3}$	$2.685\ 10^{-2}$

Table 6.3: Theoretical whole-body SAR for the scenario of Fig. 6.7

turns out that the contribution of the diffuse power density I_D for all the investigated scenarios cannot be neglected compared to the LOS power density I_L, as we also have found in Chapter 4.

Whole-body SAR from the circuit model simulation

The Advanced Design System (ADS) [24] is used to simulate the circuit model. The circuit model of Fig. 6.3 is used to emulate the exposure of the configuration shown in Fig. 6.7. Because the R and C-values are now known, (6.6) is used to compute the actual value of the voltage E feeding the source for each circuit

model. As mentioned in Section 6.2.2, the source is turned off after 1 ns since this corresponds to the pulse duration. The circuit model for one person, e.g., p_{11} is displayed in Fig. 6.8.

$$R_{11} = 18.58\,\Omega$$

$$E_{11} = 4.20V$$
$$\Delta = 1ns$$

$$C_{11} = 3.45\,nF \quad U_{11}(t)$$
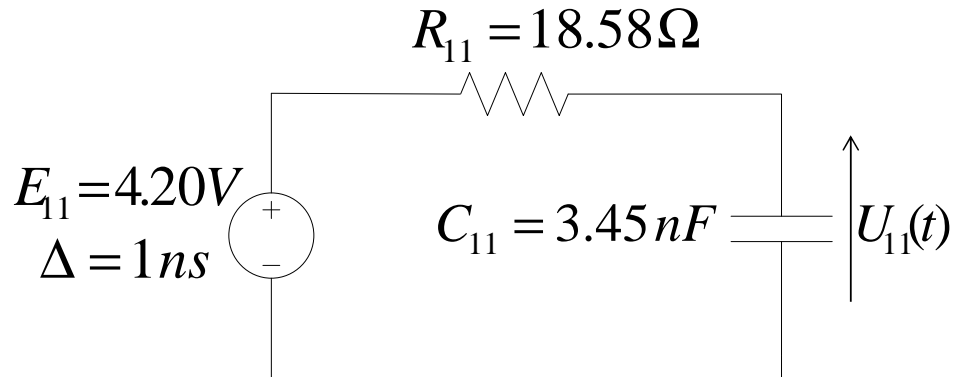
Figure 6.8: Circuit model of person p_{11}. The source has been turned off after 1 ns. A transient simulation was used to obtain the voltage decay over 600 ns with a step of 0.1 ns

The voltage in a capacitance is time dependent and frequency independent; thus a transient simulation is used in each case. The schematic is the same for any other person illustrated in Fig. 6.7. However, the value of the parameters R, C, and E is replaced with the appropriate ones, whose values can be found in Tables 6.2 and 6.4. The result of the simulation of Fig. 6.8 is the voltage's discharge in the capacitance, as shown in Fig. 6.9. The separation Tx-person in meter is given on the X-axis and the capacity voltage in Volt

Figure 6.9: Capacity voltage for person p_{11}

on the Y-axis. It can be verified that the value of U_0 of p_{11} in Table 6.2 corresponds to the maximum value

in the voltage plot of Fig. 6.9. A marker on the plot shows the person's (i.e., p_{11}) location and the voltage over the capacitance at this distance. Knowing the capacity voltage at a certain delay (hence at a certain distance), (6.37) enables the determination of the SAR_{wb} absorbed by a person in the room. The simulated results in terms of the $SAR_{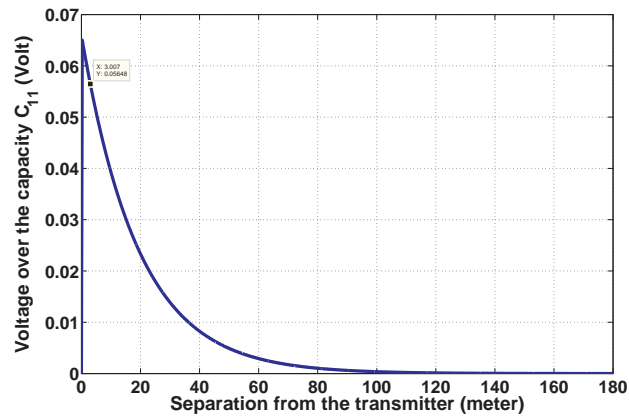wb}$ values are shown in Table 6.4. These results agree excellently with those of Table 6.3. Recall the mass and the ACS_{wb} of each person are 70 kg and 0.35 m^2, respectively. The relative error ΔSAR is defined as the difference between the theoretical and the simulated values in percentage of the theoretical value. These errors are also shown in Table 6.4. The most relevant remark here is the fact that the diffuse fields contribution has been accounted for - through a circuit model - to assess the human SAR_{wb}. It is worthy to mention that the simulation part does not aim to validate the theory; rather, it shows a method

Person	distance d_0 (m)	E (V)	SAR_{wb}^{sim} (μW/kg)	ΔSAR (%)
p_{11} (R1)	3	4.20	0.234	0.42
p_{12} (R1)	6	2.10	$9.20 \ 10^{-2}$	0.75
p_{21} (R2)	10	1.54	$1.80 \ 10^{-2}$	1.1
p_{31} (R3)	8	1.54	$2.67 \ 10^{-2}$	0.56

Table 6.4: Whole-body SAR from simulation for the scenario of Fig. 6.7

to implement the theory of room electromagnetics in real scenarios. The present circuit model theory *i)* is based on the room electromagnetics theory, which has already been validated through measurements [3] and *ii)* the room electromagnetics based SAR_{wb} assessment has also been addressed and validated through measurements and numerical simulations in Chapter 4. The presented circuit model theory is based on these previous validations.

6.4.4   Application to IEEE 802.11 systems

Consider an IEEE 802.11g system operating in the 2.40 GHz band in the same indoor environment shown in Fig. 6.7. The characteristics of the system are retrieved from [7] and are as follows: an EIRP of 100 mW, and an active duration of the transmitted pulse Δ of 209 μs. The exposure of the persons for such system are listed in Table 6.5. Equations (6.35), (6.36), and (6.28) have been used to compute I_D, $I_{D,a}$, and

Person	distance (m)	τ or τ_a (ns)	I_D or $I_{D,a}$ (mW/m^2)	I_L (mW/m^2)	SAR_{wb} (μW/kg)
p_{11} (R1)	3	32.06	0.255	0.884	3.50
p_{12} (R1)	6	32.06	0.255	0.221	1.80
p_{21} (R2)	10	43.00	0.034	0.0637	0.33
p_{31} (R3)	8	35.36	0.048	0.0995	0.49

Table 6.5: Exposure to IEEE 802.11g system

I_L, respectively. We noticed that the SAR_{wb} for the WLAN system (Table 6.5) is higher than the SAR_{wb} for the UWB system (Table 6.3). One may think that this is due to the higher transmitted power in the WLAN system case. This is correct if we make an absolute comparison of the SAR_{wb} values. However, let us

make a relative comparison of the different powers involved in the absorption. The ratio of the LOS power densities for both systems $\frac{I_{L,UWB}}{I_{L,WLAN}}$ and the ratio of the diffuse power densities for both systems $\frac{I_{D,UWB}}{I_{D,WLAN}}$ for the different persons are now computed using the values of Tables 6.3 and 6.5 and are listed in Table 6.6. On the one hand, the LOS component power densities ratio between the UWB and WLAN systems yields

Person	distance (m)	$\frac{I_{D,UWB}}{I_{D,WLAN}}$	$\frac{I_{L,UWB}}{I_{L,WLAN}}$
p11 (R1)	3	0.0549	0.0747
p12 (R1)	6	0.0404	0.0747
p21 (R2)	10	0.0347	0.0770
p31 (R3)	8	0.0354	0.0740

Table 6.6: UWB and WLAN systems power densities ratio for both LOS component and DMC

a nearly constant value of about 0.07 for all the investigated scenarios, which is also the ratio between the transmitted powers of the UWB (i.e., 7.40 mW) and the WLAN (i.e., 100 mW) systems. Therefore, the induced SAR_{LOS} due to the LOS component is the same for both systems assuming the same transmitted power.

On the other hand, the diffuse power densities ratios between UWB and WLAN systems vary for all the investigated scenarios, and the ratios are lower than the transmitted powers ratio of 0.074. This shows that for the same transmitted power, the exposure to the diffuse fields in an UWB system will be lower than the exposure to the diffuse fields in a WLAN system. Moreover, (6.17) and (6.35) confirm that the diffuse fields' exposure for UWB systems is *always* lower than the diffuse fields exposure for the WLAN exposure (for the same transmitted power), regardless of the separation from the transmitter. This can also be intuitively understood by the fact that the diffuse energy density never reaches a steady state for the UWB systems - due to the small duration of the pulse - unlike the WLAN systems, where the diffuse fields' energy evolves to the steady state.

For the SAR_{wb} at the considered frequency, the basic restrictions is 0.08 W/kg for the general public exposure and 0.4 W/kg for the occupational exposure [10]. All the values obtained in this chapter are below these basic restriction values. However, the comparison with the basic restrictions values is not the purpose of this work; rather, it aims to determine via an electrical circuit model the actual absorption levels in realistic indoor environments.

6.5 Conclusion

An electrical circuit model for the human exposure and average whole-body specific absorption rate prediction in indoor environments is proposed in this chapter. Basically, the method translates the room electromagnetics theory into an electrical circuit, which may be embedded into circuit components simulators. The method accounts for the diffuse fields and for the line-of-sight component as well, and hence, allows the forecast of the SAR_{wb} in realistic complex environments. Moreover, we show in this chapter a simple method to determine the reverberation time in a realistic environment without the need of carrying

out any measurements or simulations. The theory applies to both the same room and adjacent rooms scenario and an application of the circuit model to our working office is presented. The strength of the method lies in its simplicity since its does not require any simulation of the entire room. The theory is applied to an ultra-wideband system and to a wireless local area network system. It turns out that the lowest absorption rate is obtained for the UWB system and this is due to the diffuse fields, whose energy density evolution cannot reach a steady state, unlike for the WLAN systems.

References

[1] Majid A. Nemati and Robert A. Scholtz. A Diffusion Model For UWB Indoor Propagation. In *Military Communications Conference.*, 2004.

[2] M. A. Nemati and R. A. Scholtz. A Parametric Analytical Diffusion Model for Indoor Ultra-Wideband Received signal. In *Conference on Signals, Systems and Computers.*, 2005.

[3] J. B. Andersen, J. Ø. Nielsen, G. F. Pedersen, G. Bauch, and M. Herdin. "Room Electromagnetics". *IEEE Antennas Propagat. Mag.*, 49, (2): pages 27–33, 2007.

[4] N. Czink, A. Richter, E. Bonek, J. P. Nuutinen, J. Ylitalo. "Including Diffuse Multipath Parameters in MIMO Channel Models". In *IEEE 66th Vehicular Technology Conference (VTC)- Fall.*, 2007.

[5] J. Poutanen, J. Salmi, K. Haneda, V. M. Kolmonen, and P. Vainikainen. "Angular and Shadowing Characteristics of Dense Multipath Components in Indoor Radio Channels". *IEEE Trans. Antennas Propag.*, 59: pages 245–253, 2011.

[6] J. B. Andersen, K. L. Chee, M. Jacob, G. F. Pedersen, T. Kürner. "Reverberation and Absorption in an Aircraft Cabin with the Impact of Passengers". *IEEE Trans. Antennas and Propag.*, 60 (5): pages 2472–2480, 2012.

[7] L. Verloock, W. Joseph, G. Vermeeren, and L. Martens. "Procedure for Assessment of General Public Exposure from WLAN in Offices and in Wireless Sensor Metwork Testbed". *Health Physics*, 98 (4): pages 628–638, 2010.

[8] V. Degli-Esposti. "A Diffuse Scattering Model for Urban Propagation Prediction". *IEEE Trans. Antennas and Propag.*, 49 (7): pages 1111–1113, 2001.

[9] V. Degli-Esposti, F. Fuschini, E. M. Vitucci, and G. Falciasecca. "Measurement and Modeling of Scattering From Buildings". *IEEE Trans. Antennas Propag.*, 55 (1): pages 143–153, 2007.

[10] ICNIRP. "Guidelines for limiting exposure to time-varying electric, magnetic, and electromagnetic fields (up to 300 GHz)". *Health Physics*, 74 (4): pages 494–522, 1998.

[11] S. Kühn, W. Jennings, A. Christ and N. Kuster. "Assessment of induced radio-frequency electromagnetic fields in various anatomical human body models". *Phys. Med. Biol.*, 54 (2009): pages 875–890, 2009.

[12] T. Kientega. A new approach to assess the specific absorption rate induced by multiple plane waves at 2.1 GHz. In *EuCAP 2011 - Convened Papers*, 2011.

[13] E. Conil, A. Hadjem, A. Gati, M. F. Wong and J. Wiart. "Influence of Plane-Wave Incidence Angle on Whole Body and Local Exposure at 2100 MHz". *IEEE Trans. Electromagn. Compat.*, 53, No. 1: pages 48–52, 2011.

[14] A. Hirata, N. Ito and O. Fujiwara. "Influence of electromagnetic polarization on the whole-body averaged SAR in children for plane-wave exposures". *Phys. Med. Biol.*, 54 (2009):N59–N65, 2009.

[15] T. Uusitupa, I. Laakso, S. Ilvonen and K. Nikoskinen. "SAR variation study from 300 to 5000 MHz for 15 voxels models including different postures". *Phys. Med. Biol.*, 55: pages 1157–1176, 2010.

[16] O. Franek, J. B. Andersen and G. F. Pedersen. "Diffuse Scattering Model of Indoor Wideband Propagation". *IEEE Trans. Antennas Propag.*, 59, No. 8: pages 3006–3012, 2011.

[17] A. Bamba, W. Joseph, J. B. Andersen, E. Tanghe, G. Vermeeren, D. Plets, J. O. Nielsen, and L. Martens. "Experimental Assessment of Specific Absorption Rate Using Room Electromagnetics". *IEEE Trans. Electromagn. Compat.*, 54 (4): pages 747–757, 2012.

[18] Bruce Hapke. "Theory of Reflectance and Emittance Spectroscopy". *Cambridge University Press*, 1993.

[19] A. Bamba, M. T. Martinez-Ingles, D. P. Gaillot, E. Tanghe, B. Hanssens, J. M. Molina-Garcia-Pardo, M. Lienard, L. Martens, and W. Joseph. "Experimental Investigation of Electromagnetic Reverberation Characteristics as a function of UWB Frequencies". *IEEE Antennas Wireless Propag. Lett. (accepted for submission)*, 2014. DOI: 10.1109/LAWP.2014.2382873.

[20] F. Mani, F. Quitin, and C. Oestges. "Accuracy of depolarization and delay spread predictions using advanced ray-based modeling in indoor scenarios". *EURASIP Journal on Wireless Communications and Networking. Available online: http://jwcn.eurasipjournals.com/content/2011/1/11*, no. 11:11 pages, 2011.

[21] C. F. Eyring. "Reverberation time in DEAD Rooms". *J. Acoustic. Soc.*, 1: pages 217–241, 1930.

[22] H. Kuttruff. *"Room Acoustics"*. Spon Press, London, 2000.

[23] Andreas F. Molisch. "Ultrawideband Propagation Channels-Theory, Measurement, and Modeling". *IEEE Trans. Veh. Technol.*, 54 (5): pages 1528–1545, 2005.

[24] Agilent Technologies. Advanced design system, ads. http://www.home.agilent.com.

7
Conclusions and future research

This chapter summarizes the main achievements and conclusions obtained during this thesis. Furthermore, some opportunities for future research are mentioned.

7.1 Conclusions

The radio propagation community has considered for several decades the measurement data of wireless radio channel as a superposition of a possible Line-Of-Sight (LOS) contribution (present in LOS conditions) and discrete specular paths stemming from specular reflections. While modeling of the wireless channel is satisfactory for the propagation in outdoor or urban environments, recent channel investigations in realistic indoor environments show that modeling of wireless channels with finite number of discrete paths does not describe faithfully all the propagation mechanisms occurring in the environment. Such modeling of the wireless channel neglects the contribution of diffuse scattered fields, which stem from scattering at rough surfaces and/or diffraction at edges. The diffuse scattered field is the part of the measurement data that can not be characterized with discrete paths. Furthermore, the diffuse scattered fields may contribute significantly in the total power involved in indoor environments.

Knowing accurately the power densities incident on humans is important for calculating the absorption of the fields in human bodies in order to determine if there exist potential harmful health effects. Dosimetry studies have numerically investigated the human's whole-body averaged Specific Absorption Rate (SAR_{wb}) in the RF range. The numerical investigations of the SAR_{wb} were based on deterministic (or discrete) representation of the incident field(s), neglecting thereby the contribution of the diffuse fields in the absorption. The main contribution of the dissertation is the investigation of human absorption due to diffuse fields, which has never been addressed in the literature. This has been tackled in the following manner.

In Chapter 1, we provided an overview of some radio channel models. These channel models traditionally do not account for the diffuse fields propagation. Consequently, we described the diffuse multipath components and briefly present an estimator of the channel's parameters (i.e., RiMAX) to retrieve the diffuse multipath components in measurement data. A simple channel model (i.e., *room electromagnetics*) that models adequately the propagation of the diffuse scattered fields was introduced and its properties and characteristics were also briefly presented.

Chapter 2 was devoted to the characterization of the absorption cross section due to diffuse fields by measurements of the reverberation time values in a reverberation chamber. We presented in this chapter a methodology to determine the reverberation time and the absorption cross section due to diffuse fields. Reverberation chambers are extreme references to emulate the propagation of electromagnetic waves in realistic indoor environments where diffuse fields are prominent. We showed the difference between the absorption cross section in diffuse fields and the absorption cross section due to discrete plane wave(s). Moreover, measurements in a reverberation chamber and simulations enabled us to determine some properties of the diffuse fields, such as the polarization and phase. Finally, we determined the absorption cross section of a human adopting several postures in diffuse fields in the reverberation chamber.

In Chapter 3, we investigated the properties of the reverberation time in realistic indoor environments. This chapter can be considered as an application of Chapter 2. The benchmarking of the reverberation time consisted of measurements with different antennas, measurement systems (virtual channel sounder and real channel sounder), and environments (Aalborg and Ghent). We extended the room electromagnetics theory from a single room to adjacent rooms scenario. The analysis of the room electromagnetics theory allowed the derivation of the absorption cross section in diffuse fields. Finally, the experimental methodology developed in Chapter 2 was used to determine the diffuse absorption cross section of humans in a realistic office.

In Chapter 4, we addressed the SAR_{wb} of humans under realistic propagation conditions, i.e., presence of diffuse fields and a possible LOS component. Depending on the receiver's location, the investigation of the power density showed that the diffuse fields may be prominent in indoor environments as it may reaches 95% of the total power density. Several scenarios (depending on the contribution of the diffuse fields in the total power) were considered, and it was observed that the diffuse fields contribute significantly to the absorption rate at larger distances from the transmitting antenna. Moreover, the experiment procedure to determine the SAR_{wb} under realistic conditions was validated via numerical simulation of a cylindrical phantom.

Chapter 5 proposed a simple formula to determine the total specific absorption rate under both LOS and diffuse fields' illumination. The method is based on an ellipsoid analysis and simulations and is valid in the GHz region. The formula has been applied to four heterogeneous phantoms and validated using numerical simulations. The developed formula can be used to assess the absorption rate of humans under diffuse and/or LOS illumination. The formula is especially accurate for adults.

Finally, Chapter 6 proposed a circuit model to determine the power density in diffuse fields, and hence the related absorption rate of a human. Basically, the model translates the room electromagnetics into a R-C electrical circuit where the decaying diffuse energy present in a room is modeled with the energy inside a capacitance C. This circuit model can also be embedded into a circuit simulator. The theory applies to both UWB and WLAN systems. We also show in this chapter that the absorption rate of humans due to diffuse fields is larger in WLAN systems than in UWB systems. This is due to the fact that the diffuse energy

reaches the steady state for WLAN systems, which is not the case for UWB systems.

7.2 Future research opportunities

The first research opportunity deals with the (frequency) limits of the room electromagnetics theory. The room electromagnetics theory is valid because the propagation of the electromagnetic waves is dominated by diffuse scattering. Diffuse scattering phenomena are usually favored in environments where the surfaces are considered as rough. However, the roughness of the surfaces depends on the considered wavelength [1, 2]. At higher frequencies (e.g., mmWaves range), the surfaces are more likely to be rough because the Rayleigh criteria [3] would be fulfilled. Therefore, one may think that the scattering could be prominent under these conditions. It is correct that multiple diffuse scatterings will occur at the surfaces in the mmW range. However, if a receiving antenna is not located close to these surfaces, the scattered waves will not always reach the receiving antenna due to the high free-space propagation loss at higher frequencies. Therefore, the uniformity of the fields within the room (which is a key condition for the room electromagnetics theory) may be questioned. This issue is more apparent when we compare experimental power delay profiles obtained at two frequencies, e.g., 3.5 GHz and 60 GHz (see Fig. 7.1).
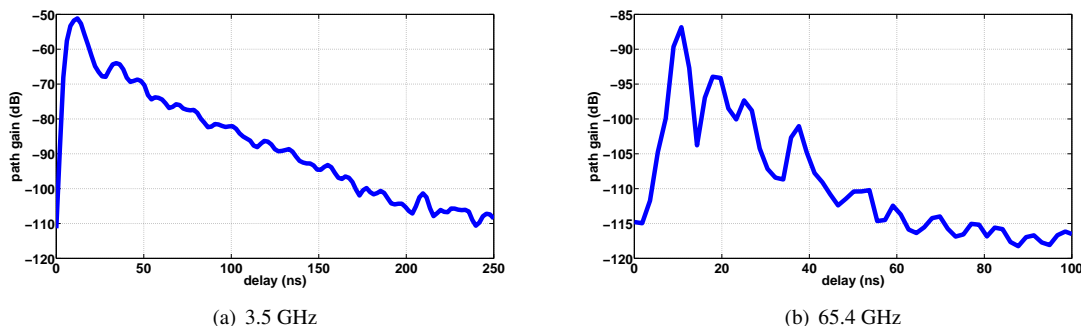

(a) 3.5 GHz   (b) 65.4 GHz

Figure 7.1: Experimental power delay profile at 3.5 and 65.4 GHz in an indoor environment

We observe at least two differences in the PDPs of Fig. 7.1. First, the tail of the PDP of Fig. 7.1(a) can be clearly approximated by a line, from which the reverberation time is derived. In Fig. 7.1(b), we see that it would be inaccurate to approximate the PDP's tail with a line. Second, we see from Fig. 7.1(a) and Fig. 7.1(b) that the received electromagnetic power (or energy) drops faster into the noise region in the latter (shorter maximum arrival delay) than in the first figure. Following these observations, it would be interesting to investigate the room electromagnetics validity in the mmW range. This could be performed via MIMO channel measurements and then be verified for instance if the tails of the PDPs obtained at different locations in an indoor environment *i)* could be approximated by linear tails and *ii)* have the same slope. Note that the dimensions of the considered environment might have an influence, especially at higher frequencies, and

have to be taken into account for a rigorous analysis.

The room electromagnetics has been derived from the room acoustics theory [4]. The room acoustics theory addresses the diffusion of sound fields in coupled rooms as well. We have extended the room electromagnetics theory to the adjacent rooms' scenario in Chapter 3. However, the extension of the room electromagnetics theory to non-adjacent coupled rooms would add valuable contribution to this work. I recommend other researchers to investigate this issue.

Another interesting subject to investigate is the properties of the diffuse fields in realistic environments. We have considered uniform distribution and normal distribution for the phase and polarization of the diffuse fields, respectively, in indoor environments. This was based on measurements in a reverberation chamber and assumptions taken from the room acoustics theory. However, it is essential to carry out MIMO channel measurements in order to carefully address the properties of the polarization and phase of the diffuse scattered fields in realistic indoor environments. This could also be helpful for researchers who are interested in simulating the diffuse fields using numerical tools. Precise information on the diffuse fields polarization and phase can be included in advanced ray tracing tools to enhance their performance as the current versions do not include the polarization of the diffuse scattered waves due to limited knowledge on this, e.g., [5].

The reverberation time of an indoor environment can be theoretically determined (Section 1.3.1 of Chapter 1) or via empirical methods, e.g., [6]. One can use the value of the reverberation time to generate the PDP at a given location in an indoor environment, e.g., based on the one-slope method. However, this approach does not consider the small-scale variations of the received signal caused by motions of people, objects around the receiver, etc. Small-scale variations in room to room scenarios have been recently investigated [7]. These two approaches may be merged to predict the PDP in indoor environments. Furthermore, extensive MIMO channel measurements in single and couple room(s) should be carried out for validation purposes.

References

[1] O. Landron, M. J. Feuerstein, and T. S. Rappaport. "In Situ Microwave Reflection Coefficient Measurements for Smooth and Rough Exterior Wall Surfaces". In *43rd IEEE Vehicular Technology Conference, Secaucus, NJ, USA*, 1993.

[2] F. Delfino, P. Girdinio, L. Minervini, M. Nervi. "Electromagnetic plane wave scattering from building surfaces". *COMPEL - The international journal for computation and mathematics in electrical and electronic engineering*, 25 (4): pages 1007–1018, 2006.

[3] P. Beckmann and A. Spizzichino. *"The Scattering of Electromagnetic Waves from Rough Surfaces"*. Norwood, MA, 1987.

[4] H. Kuttruff. *"Room Acoustics"*. Spon Press, London, 2000.

[5] F. Mani, F. Quitin, and C. Oestges. "Accuracy of depolarization and delay spread predictions using advanced ray-based modeling in indoor scenarios". *EURASIP Journal on Wireless Communications and Networking. Available online: http://jwcn.eurasipjournals.com/content/2011/1/11*, no. 11:11 pages, 2011.

[6] A. Bamba, M. T. Martinez-Ingles, D. P. Gaillot, E. Tanghe, B. Hanssens, J. M. Molina-Garcia-Pardo, M. Lienard, L. Martens, and W. Joseph. "Experimental Investigation of Electromagnetic Reverberation Characteristics as a function of UWB Frequencies". *IEEE Antennas Wireless Propag. Lett. (accepted for submission)*, 2014. DOI: 10.1109/LAWP.2014.2382873.

[7] E. Vinogradov, W. Joseph, and C. Oestges. "Modeling and Simulation of Fast Fading Channels in Indoor Peer-to-Peer Scenarios.". In *Proceedings 8th European Conference on Antennas and Propagation, 2014, p. 529-530*, pages pages 529–530, Den Haag, The Netherlands, 07-11 April 2014.

[8] ICNIRP. "Guidelines for limiting exposure to time-varying electric, magnetic, and electromagnetic fields (up to 300 GHz)". *Health Physics*, 74 (4): pages 494–522, 1998.